NASA Contractor Report 172381

ANALYTICAL MODEL OF THE STRUCTUREBORNE INTERIOR NOISE INDUCED BY A PROPELLER WAKE

M. C. Junger, J. M. Garrelick, R. Martinez, and J. E. Cole, III

Cambridge Acoustical Associates, Inc.
54 Rindge Ave. Ext.
Cambridge, MA 02140

Contract NAS1-17570

May 1984

National Aeronautics and
Space Administration

Langley Research Center
Hampton, Virginia 23665

PROJECT OVERVIEW

Advanced prop-fan propulsion systems which are being considered for passenger aircraft have noise characteristics quite different from turbo-jet systems they may replace. Rather than being primarily broadband much of the acoustic energy of propellers is concentrated in tonals at the harmonics of the blade passing frequency (BPF). Since the fundamental BPF is in the range of several hundred hertz, the tonal spectrum of the propeller induced noise is of concern from the viewpoint of passenger acceptance and comfort.

The objective of this study is to examine analytically the structureborne contribution to the interior noise that is induced by the propeller wake acting on the wing. Analytical models have been developed to describe each aspect of this path including the excitation loads, the wing and fuselage structures, and the interior acoustic space. Because this is a feasibility study, the emphasis has been placed on examining a variety of parameters, and as a result different models have been developed to examine specific parameters. The excitation loading on the wing by the propeller wake is modeled by a distribution of rotating potential vortices whose strength is related to the thrust per blade. The response of the wing to this loading is examined using beam models. A model of a beam structurally connected to a cylindrical shell with an internal acoustic fluid has been developed to examine the coupling of energy from the wing to the interior space. The model of the acoustic space allows for arbitrary end conditions (e.g., rigid or vibrating end caps). Calculations are presented using these models to compare with a laboratory test configuration as well as for parameters of a prop-fan aircraft.

Several of the major findings of this study are summarized as follows:

1. The unsteady-lift reaction of the wing to the propeller-wake field is a significant mechanism for transfer of vortex energy to structural vibration.
2. In the absence of significant scattering from major structural discontinuities, the propagation loss of structureborne noise along the wing at the BPF is negligible and cabin noise levels are comparable to the source pressure levels for a cylindrical fuselage.
3. Stringers that are small and in effect structurally integral with the skin have minimal impact on propagation along the wing. However, cut-off phenomena associated with a parallel array of discrete stringers could be created and exploited to enhance propagation loss.
4. The interior acoustic levels on average are not appreciably altered by the presence of structural damping in the fuselage skin.

N84-32119#

TABLE OF CONTENTS

SUMMARY, CONCLUSIONS, AND RECOMMENDATIONS

Advanced prop-fan propulsion systems which are being considered for passenger aircraft have noise characteristics quite different from turbo-jet systems they may replace. Rather than being primarily broadband much of the acoustic energy of propellers is concentrated in tonals at the harmonics of the blade passing frequency (BPF). Since the fundamental BPF is in the range of several hundred hertz, the tonal spectrum of the propeller induced noise is of concern from the viewpoint of passenger acceptance and comfort.

Propeller noise can propagate to the interior of the fuselage by paths that can be categorized as being primarily either airborne or structureborne. The airborne path is expected to be the dominant path, and it is estimated that the required insertion loss for this path provided by the fuselage must be approximately 55 dB at a BPF of 200 Hz. Measurements using conventional aircraft suggest that the contribution to the interior noise of the structureborne path is not far below that of the airborne path. Consequently control of the structureborne path is likely to be important in achieving acceptable interior noise levels.

The objective of this study is to examine analytically the structureborne contribution to the interior noise that is induced by the propeller wake acting on the wing. Analytical models have been developed to describe each aspect of this path including the excitation loads, the wing and fuselage structures, and the interior acoustic space. Because this is a feasibility study, the emphasis has been placed on examining a variety of parameters, and as a result different models have been developed to examine specific parameters. The excitation loading on the wing by the propeller wake is modeled by a distribution of rotating potential vortices whose strength is related to the thrust per blade. The response of the wing to this loading is examined using beam models. A model of a beam connected elastically to a cylindrical shell with an internal acoustic fluid has been developed to examine the coupling of energy from the wing to the interior space. The model of the acoustic space allows for arbitrary end conditions (e.g., rigid or vibrating end caps). Calculations are presented using these models to compare with a laboratory test configuration as well as for parameters of a prop-fan aircraft.

The principal conclusions resulting from the analytical modeling and numerical calculations are the following:

1. The unsteady-lift reaction of the wing to the propeller-wake field is a significant mechanism for transfer of vortex energy to structural vibration. For a fixed value of design thrust, and for points on the wing where wake loading is maximum, harmonics of the wake-induced pressure vary inversely with both the square of the propeller radius and the reduced frequency of the tonal. Predicted and experimentally obtained source levels are in reasonable agreement.

2. In the absence of significant scattering from discrete stiffeners, e.g., ribs, or from other major structural discontinuities, the propagation loss of structureborne noise along the wing at the BPF is negligible and cabin noise levels are comparable to the source pressure levels for a cylindrical fuselage.

3. For a rib to enhance significantly the propagation loss along a wing it must constrain both the translational and rotational motion of the skin. The criteria for achieving this objective appear to be realizable with minimum weight penalty. In practice rib effectiveness will be limited by rib elasticity which reduces its scattering strength and allows more efficient propagation across and coupling into it, both effects leading to an increase in cabin noise, the latter via the rib-spar-fuselage path.

4. Sound radiation (airborne) associated with structureborne noise scattering from structural discontinuities along the wing is negligible compared with the direct acoustic path.

5. Stringers that are small and in effect structurally integral with the skin have minimal impact on propagation along the wing. However, cut-off phenomena associated with a parallel array of discrete stringers could be created and exploited to enhance propagation loss. The criterion for effectiveness is given as $k_f L < \pi$, where k_f is the wavenumber of flexural waves in the skin and L the interstringer spacing. Also, the (spanwise) length of the stringer array need only measure a flexural wavelength in the skin and therefore entails minimum weight penalty.

6. Spar vibration levels directly excited by the unsteady lift are less than those in the skin near the midchord. Also, in the absence of stiffeners, either ribs or stringers, coupling of structureborne noise from the skin into the spars is minor. The extent of coupling from the skin to spars in the

presence of ribs has not been determined, and in view of the previous conclusions this skin-rib-spar-fuselage path may be the dominant one for typical wing configurations.

7. The interior acoustic levels on average are not appreciably altered by the presence of structural damping in the shell.

8. It is feasible to develop an analytical model of the structureborne path of the shaker driven laboratory model. However the noise predictions of a model that includes finite shell dynamics with frames, beam-shell interactions and structural damping, but ignores fluid loading, acoustic absorption and shell stringers do not compare favorably with laboratory measurements.

9. The feasibility of developing an equivalent model of the structureborne path along an actual wing-fuselage structure is questionable in view of the implied computer costs and/or running times. (For example the surface area of an aluminum fuselage of 3.05 m (10 ft.) diameter, 12.2 m (40 ft.) length and 2.5×10^{-3} m (0.1 in.) skin thickness measures roughly 10^3 flexural wavelengths at a frequency of 200 Hz. Using only a one-quarter wavelength mesh size and 3 degrees of freedom per node a finite element analysis of the fuselage skin alone would entail 10^4 unknowns exclusive of the modelling of the wing or the interior acoustic space.)

10. Asymptotic or "canonical" analytical models of specific structural elements and features characteristic of actual wing-fuselage structures, e.g., stiffened skins, can be used to identify propagation phenomena that are potentially useful for diagnostic and noise control purposes. However, here it is particularly important to use such models in conjunction with a measurement program, either full scale or model, for confirmation.

Recommendations for further work fall into two categories, these being analytical modelling and experimental measurements. Further development of the analytical models examined in this report is suggested in the following areas:

1. In modelling the propeller wake, include the effects of, (a) a viscous vortex core, (b) three-dimensional unsteady aerodynamics, and (c) the dynamics of vortex paths in the presence of solid surfaces.

2. In modelling the wing, develop and implement models that trace the skin-rib-spar-fuselage path accounting for both rib elasticity and the spar-fuselage frame interaction.

3. In modelling the fuselage structure include the effects of, (a) internal stiffeners, and (b) either acoustic absorption along the boundaries (see 4 below) or the loading of the internal fluid on the structure.

4. In modelling the interior acoustic space implement the theory in terms of the eigenfunctions appropriate to large boundary absorption (e.g., Bessel functions of the appropriate complex eigenvalues).

Recommendations for experimental studies directed toward characterizing the structureborne noise path are as follows:

5. Using the existing laboratory model as a diagnostic tool for analytical concepts and models, examine the dependence of the interior pressure levels on a number of parameters including spatial location, structural damping, acoustic absorption, and discrete structural stiffeners.

6. Develop new laboratory models of both wing and fuselage structures based on the scaling laws implied by existing analytical models. These analytical models may also be used to assess scaling law conflicts, tradeoffs and compromises.

7. The extent to which cut-off phenomena predicted for a stringer-skin geometry enhances the propagation loss along existing wings should be determined experimentally. Also the feasibility of further exploiting this mechanism for noise control purposes should be studied by means of a combined analytical-laboratory measurement program.

8. Using a full scale aircraft and with excitation by shaker or by propulsion system when possible, (a) measure the structural transfer functions along the wing skin and spars; and (b) measure the transfer functions of structural response to interior pressure. Structural intensity measurements may be useful to examining the power flow along specific components of the wing.

I. INTRODUCTION

Advanced prop-fan propulsion systems promise to provide fuel efficient flight at high subsonic speeds. The propellers in these systems having multiple skewed blades represent a noise source with characteristics quite different from the dominant noise sources of current turbo-fan engines. In particular, rather than being primarily broadband, much of the acoustic energy of prop-fan propulsion systems is concentrated in tonals at harmonics of the blade-passing frequency. Since the fundamental blade passing frequency (i.e., propeller rpm times number of blades) is in the range of several hundred Hertz, the tonal spectrum of the propeller is of concern from the viewpoint of passenger acceptance and comfort.

The paths by which propeller noise propagates to the interior of the fuselage can be categorized as being primarily either airborne or structureborne. We define the airborne path as the path of propeller induced excitation that acts directly through the air on the fuselage. This includes propeller radiated noise and the aerodynamic near field of a rotating propeller located in close proximity to the fuselage. The airborne path is expected to be the dominant path by which acoustic energy excites the aircraft interior. The airborne insertion loss required by a fuselage to reduce the propeller tonal at the blade passing frequency to an 80 dB(A) (re: 20 μPa) interior level is approximately 55 dB (i.e., assuming 135 dB(A) free field level at 200 Hz). A variety of means to achieve a large sidewall transmission loss have been examined in the literature. Additionally, analytical models have been developed to predict the interior noise level in response to acoustic excitation of the fuselage. A recent review of many of these models is presented in Ref. 1.

In general the parameters governing the transmission of airborne acoustic energy to the aircraft interior are more clearly defined than those that control the transmission of structureborne energy which is the subject of this report. We define the structureborne path as that path by which propeller induced energy propagates to the fuselage via other structures, notably the wing. Although useful for the purpose of discussion, the distinction between airborne and structureborne paths is not rigorous since structureborne energy can radiate and become airborne energy and vice versa. The sources of structural excitation at propeller related tonals include the interaction of the lifting surfaces with the propeller wake and engine vibration. The unsteady wake of the propeller acts on the skin of the wing and of any rear control surfaces in its path. This vibration excitation can propagate along the skin and the primary wing structure to excite the fuselage. Engine vibration is transmitted through the engine mounts directly to the primary wing structure. Both of these excitations can transmit energy to the fuselage which in turn radiates noise to the aircraft interior.

Structureborne noise has been cited by several investigators as a potentially important consideration for achieving acceptable interior noise levels in propeller driven aircraft.[2-4] While the structureborne path, which in fact may be multiple paths, is not expected to be the dominant means by which acoustic energy reaches the aircraft interior, its contribution may not be far below that of the airborne path, especially in view of the large noise reduction required for the advanced tuboprop aircraft. For example, measurements of interior noise made on a conventional twin engine turboprop aircraft (deHaviland Twin Otter) with both wing and fuselage wrapped to reduce excitation by the propeller wake suggest that the structureborne noise is no more than 10 dB below that of the aircraft path.[5] For a single engine aircraft with a reciprocating engine, measurements reported in Ref. 6 indicate that both airborne and structureborne contributions to the interior noise are comparable in level. In a more recent study, the importance of structureborne noise in a single engine aircraft has been further documented.[7] Analytical modeling of the structureborne noise path is currently needed to support and further evaluate the results of these empirical studies. Although the fuselage and interior acoustic space have been modeled to examine parameters important to the airborne path,[1] the excitations used in these models have typically been a single acoustic wavenumber pressure field.

The objective of the present study is to develop an analytical model (albeit simplified) of the structureborne path including excitation loads, wing and fuselage structures, and interior acoustic space. The excitation loading on the wing by the propeller wake is modeled by a distribution of rotating potential vortices whose strength is related to the thrust per blade. Beam and plate models are used to represent the response of the wing to this loading. A model of a beam elastically built into a cylindrical shell with an internal acoustic fluid has been developed to examine the coupling of energy from the wing to the interior space. The model of the acoustic space allows for arbitrary end conditions (e.g., rigid end caps). Calculations are presented using these models to compare with a laboratory test configuration as well as for parameters of a turboprop aircraft.

II. THEORETICAL PREDICTIONS OF WING LOADING INDUCED BY A PROPELLER WAKE

A. Introduction

The near wake of a propeller in uniform flow consists of a complex system of trailing vortex sheets, each originating at a blade trailing edge. Due to self-induced velocities, these sheets quickly become unstable and roll up into a system of mainly concentrated tip vortices in a helical arrangement.[8] Neglecting for the moment the effect of self- and mutually-induced velocities after the roll up process is complete, the trajectory of each vortex filament or vortex segment may be assumed as determined solely by freestream convection (in the propeller far wake, downstream of the wing and therefore not of concern here, this assumption is not valid and vortex structure and positions become chaotic).

In the near wake, therefore, as a propeller tip approaches the horizontal plane say from above, its rolled-up tip vortex is convected over the wing, and an instant later, under the wing. Thus the vortex appears to "cut through" and, as a result, causes locally time- and spanwise-varying angles of attack and accompanying lift. The unsteady lift so generated becomes the source for noise borne by the wing structure into the cabin.

Here we develop a model for the wing loads induced by the propeller wake, and compare predicted levels to those measured by Miller et al.[3] for a 0.61 m (2 ft) diameter propeller in subsonic flow. Finally, estimates are made of vortex-induced wing pressures for an actual aircraft presently considered by NASA a possible candidate for the new prop-fan technology. When compared to typical estimates of incident airborne noise, the results of this last calculation bear out the need for study of the structural path as a potentially significant competing mechanism.

B. Propeller Wake Model and Wing Aerodynamics

Figure II-1 shows the near-wake model. A system of N straight, infinite potential vortices in rotary motion causes a downwash w on the wing plane given by

$$w(t,y) = -\frac{\Gamma}{2\pi R} \sum_{k=1}^{N} \frac{y-\cos[\Omega t + \frac{2\pi(k-1)}{N}]}{1+y^2-2y\cos[\Omega t+ \frac{2\pi(k-1)}{N}]} \qquad \text{(II-1)}$$

where t is time and y, the spanwise distance measured from the propeller hub point, has been normalized by the blade radius R; Ω and N denote propeller rotational speed and blade number, respectively. Γ stands for the strength of each vortex and may be determined from the propeller design thrust value via a lifting-line analysis performed later in the chapter.

We define the normalized downwash $\tilde{w}(t,y)$ by

$$\tilde{w} = - \frac{w}{\Gamma/2\pi R} \tag{II-2}$$

and show typical signatures in Fig. II-2, where values of Ω, and N have been chosen to match those in Miller's experiment. The y = 1.01 position corresponds to the measurement position in Ref. 3. The figure confirms that as y = 1 is approached the predicted downwash becomes more and more impulsive and that the period of the relatively complicated $\tilde{w}$ sum is $2\pi/\Omega N$, with an associated fundamental (in Hertz) equal to the blade-passage frequency $N\Omega/2\pi$. Based on this we write the vortex-induced wing lift coefficient $C_L(t,y)$ in terms of harmonics $C_{Lm}(y)$;

$$C_L(t,y) = \mathrm{Re}\left\{\sum_{m=0}^{\infty} C_{Lm}(y)e^{imN\Omega t}\right\} \tag{II-3}$$

The aerodynamic model for the wing assumes the latter to be infinite in span (no three-dimensional root or tip effects) and as a flat plate in cross section. The flow is assumed aerodynamically two dimensional with each wing reacting locally to the input downwash field (classical strip theory). Also, for applications of interest it will be found later that the airfoil reduced frequency based on the fundamental $\Omega Nb/U$, where b is wing semichord, is not small relative to unity, and so the model to calculate C_{Lm} in terms of downwash harmonics $\tilde{w}_m$ should contain high-frequency unsteady effects and should not be given merely by

$$\frac{2\pi w_m/U}{\sqrt{1-M^2}}$$

i.e., the quasi-steady assumption where U and M stand for flight speed and flight Mach number, respectively. Moreover, since flight speeds will be in the high subsonic range, compressibility effects other than that given by the $(1-M^2)^{-\frac{1}{2}}$ Prandtl-Glauert factor should also be included.

For an airfoil in subsonic flow passing through a nonuniform field given in terms of gusts, Amiet[9] has derived such an unsteadiness-compressibility correction to the quasi-steady lift coefficient (kept in curly brackets in Eq. II-4 below). Applying it in its relatively simple high-frequency limit (his Eq. 20), one then has

$$C_{Lm}(y) = \left\{ \frac{2\pi}{\sqrt{1-M^2}} \quad \frac{w_m(y)}{U} \right\} \cdot \frac{-i\sqrt{1-M^2}}{\pi\sqrt{M}\,\frac{\Omega Nmb}{U}} \tag{II-4}$$

C. Harmonic Analysis of the Propeller Wake

The analysis to obtain the wake harmonics $\tilde{w}_m$ from $\tilde{w}$ as defined by Eqs. II-1 thru II-2, begins with an identity involving two arbitrary complex numbers $\tau = e^{i\beta}$, $z = re^{i\alpha}$ (e.g., Ref. 10).

$$\frac{\tau}{\tau-z} + \frac{z^*}{\tau^*-z^*} = \frac{1-r^2}{1+r^2-2r\cos(\alpha-\beta)} \tag{II-5}$$

where * denotes conjugate.

For $r < 1$ we may now express the left hand side of Eq. II-5 as

$$1 + 2 \sum_{m=1}^{\infty} r^m \cos m(\alpha-\beta)$$

Since r, the magnitude of z, is by definition positive, this relationship is immediately applicable to the range $0 < y < 1$. Thus letting $y=r$, $\Omega t = \alpha$, $-\beta = \frac{2\pi(k-1)}{N}$, and performing some algebra one finds that

$$\frac{y-\cos\left[\Omega t + \frac{2\pi(k-1)}{N}\right]}{1+y^2-2y\cos\left[\Omega t + \frac{2\pi(k-1)}{N}\right]} = -\sum_{m=1}^{\infty} y^{m-1} \cos m\left[\Omega t + \frac{2\pi(k-1)}{N}\right] \tag{II-6}$$

By a similar calculation for $r > 1$ the left hand side of Eq. II-5 takes the form

$$-\left\{ 1 + 2 \sum_{m=1}^{\infty} \frac{\cos m(\alpha-\beta)}{r^m} \right\}$$

and for $1 < y < \infty$ we find that

$$\frac{y-\cos\left[\Omega t + \frac{2\pi(k-1)}{N}\right]}{1+y^2-2y\cos\left[\Omega t + \frac{2\pi(k-1)}{N}\right]} = \sum_{m=0}^{\infty} \frac{\cos m\left[\Omega t + \frac{2\pi(k-1)}{N}\right]}{y^{m+1}} \qquad \text{(II-7)}$$

If the cosines on the right sides of Eqs. II-5 and II-7 are now expanded out, and the sum $\sum_k$ is interchanged with $\sum_m$, the following two factors appear

$$\sum_{k=1}^{N} \cos\left[\frac{2\pi m(k-1)}{N}\right] \quad , \qquad \sum_{k=1}^{N} \sin\left[\frac{2\pi m(k-1)}{N}\right] \quad ;$$

the first of which is zero unless m is a multiple of N, and then it equals N. The second sum is identically zero. These conclusions may be used to find, for example, that the right side of Eq. II-6 becomes

$$-N \sum_{m=1}^{\infty} y^{Nm-1} \cos mN\Omega t$$

The simple manipulations used to obtain the series expression of $\tilde{w}$ for $0 < y < \infty$ may be adapted to the negative ranges $-1 < y < 0$, $-\infty < y < -1$. One writes

$$\frac{1-r^2}{1+r^2-2r\cos(\alpha-\beta)} = \frac{1-r^2}{1+r^2-2(-r)\cos(\alpha-\beta+\pi)}$$

and then replaces y by $-y > 0$ and $\frac{2\pi(k-1)}{N}$ by $\frac{2\pi(k-1)}{N} + \pi$ in the previous results.

The final series representations are now given for $\tilde{w} = \tilde{w}(t, -\infty < y < \infty)$:

$$\tilde{w} = N\sum_{m=0}^{\infty} \cos mN\Omega t \begin{cases} \dfrac{1}{y^{Nm+1}} & 1 < y < \infty \\[2ex] \dfrac{(-1)^{Nm+1}}{(-y)^{Nm+1}} & -\infty < y < -1 \end{cases} \qquad \text{(II-8a)}$$

$$\tilde{w} = N\sum_{m=1}^{\infty} \cos nmN\Omega t \begin{cases} -y^{Nm-1} & 0 < y < 1 \\[2ex] (-1)^{Nm}(-y)^{Nm-1} & -1 < y < 0 \end{cases} \qquad \text{(II-8b)}$$

so that $\tilde{w}_m = N/y^{Nm+1}$ for $1 < y < \infty$, etc. Several points of interest should be noted. First, a steady field exists for $|y| > 1 (m=0)$ which is algebraically invariant with respect to the number of blades N. Since the m=0 harmonic is odd in y (proportional to $\pm 1/|y|$), this steady component represents a net moment about the propeller axis. The authors wonder if it has ever been a factor in wing design for steady flight.

Secondly, increasing N causes a more rapid spatial decay of each $m \geq 1$ harmonic from the N value at y=1. For very large N the vortex spacing becomes infinitesimal and physically a steady limit should be approached. Mathematically, in fact, only the m=0 steady term for $|y| > 1$ remains. In this limit the solution is consistent with the fundamental theorem of electrostatics which states that the internal field of a surrounding conductor is zero and that the field outside may be interpreted as due to a single equivalent centrally located charge.[11]

Third and lastly, the initial expression in Eq. II-1 yields an infinite value of downwash w at $y = \pm 1$ at times when vortices pass through the wing plane (the denominator becomes $(y-1)(y+1)$). As $y \to \pm 1$ therefore, the time history of induced downwash becomes highly impulsive (recall Fig. II-2) and is given by a series with tonals of constant level N (transform of a delta function).

D. Calculation of Vortex Strength

Figure II-3a (from Ref. 8) shows a blade airfoil section in rotary motion. As always, lift is defined as the force normal to the relative free-stream $\sqrt{U^2+(\Omega r)^2}$. We model the radial blade load distribution as indicated in Fig. II-3b, i.e., triangular in shape. At the tip, where the radial load drops abruptly from its maximum value L_{tip} to zero, a vortex of strength Γ_v equal to the blade tip bound vorticity Γ_b must be "trailed away" according to Kelvin's circulation theorem. To obtain the strength of the bound vortex in terms of tip lift L_{tip}, we apply the two-dimensional lifting-line relation

$$\rho\sqrt{U^2+(\Omega R)^2}\ \Gamma_b = L_{tip} \ . \tag{II-9}$$

As previously discussed, upon passage through the wing the free vortex induces on the wing surface a time- and spanwise-varying angle of attack $\alpha(t,y) \simeq w/U$ from which the vortex induced unsteady airload L_v may be calculated. With C_{Lm} defined in Eq. II-4 the high-frequency compressible model yields the following relationship for the m^{th} harmonic of vortex-induced wing pressure

$$L_{vm}(y) = \frac{\rho}{2} U^2 C_{Lm}(y) \qquad \text{(II-10)}$$

Substituting for Γ_b from Eq. II-9 into Eq. II-1, and then using Eq. II-1 with Eq. II-4 into Eq. II-10, we obtain

$$L_{vm}(y) = \frac{\tilde{w}_m}{\sqrt{1+\left(\frac{\Omega R}{U}\right)^2}} \frac{L_{tip}}{2R} \frac{(-i)}{\pi\sqrt{M}\,\frac{\Omega N m b}{U}} \qquad \text{(II-11)}$$

Lastly, the tip lift L_{tip} must be related to the blade thrust T_b. Neglecting drag forces, the differential thrust dT and lift dL are related through[8]

$$dT = dL\cos\beta = dL \frac{\Omega r}{\sqrt{U^2+(\Omega r)^2}}$$

so that the total blade thrust T_b is given by

$$T_b = \int_0^R dr\, \frac{dL}{dr} \cos\beta$$

Substituting $dL/dr = L_{tip}\cdot(r/R)$ for the assumed triangular loading, and evaluating the resulting integral, one finally obtains that

$$\frac{L_{tip}}{2R} = \frac{T_b/R^2}{\sqrt{1+\left(\frac{U}{\Omega R}\right)^2} - \left(\frac{U}{\Omega R}\right)^2 \sinh^{-1}\left(\frac{\Omega R}{U}\right)} \qquad \text{(II-12)}$$

Putting the above into Eq. II-11 and defining the total propeller thrust T as $T_b N$, the desired harmonic $L_{vm}(y)$ of the vortex-induced, lifting pressure distribution is found:

$$L_{vm}(y) = \frac{T}{NR^2} \frac{\tilde{w}_m(y)}{\sqrt{1+\left(\frac{\Omega R}{U}\right)^2}} \frac{1}{\left\{\sqrt{1+\left(\frac{U}{\Omega R}\right)^2} - \left(\frac{U}{\Omega R}\right)^2 \sinh^{-1}\left(\frac{\Omega R}{U}\right)\right\}} \qquad \text{(II-13)}$$

$$\frac{i}{\pi\sqrt{M}\,\frac{\Omega m N b}{U}}$$

For a fixed value of design thrust T, L_{vm}(y=1)(the maximum for each harmonic) varies as the inverse of the square of the radius R, and as the inverse of $\Omega Nmb/U$, the "tonal reduced frequency". No other N dependence exists since the N factor in $\tilde{w}_m$ (Eq. II-8) cancels that other appearing in the $T/(NR^2)$ group of Eq. II-13.

As indicated in the final result, L_{vm} depends also on Mach number M and on advance ratio $\Omega R/U$. However, the possibility of propeller-wake airload control through these parameters appears limited due to restrictions of actual practice on high subsonic cruise speeds U (and so M), and on blade tip speed ΩR. For well-known aeroacoustic reasons the latter is preferably kept also in the high subsonic range.

E. Application of Wake Model to Two Cases of Interest

We may now apply Eq. II-13 to predict levels of the lifting pressure distribution on the wing due to the propeller wake and compare them to those measured by Miller,[3] whose laboratory model is shown in Figure II-4a. Also, a prediction is made using actual aircraft parameters.

In Ref. 3 the vane stands vertically and is aligned with a propeller radius, i.e., it intersects the propeller axis if continued upwards in the sketch. Thus, the radial position given by r/R = 1.01 in the experiment corresponds to the spanwise position given by y = 1.01 in our theoretical model.

The parameters for the laboratory propeller are the following:

Power Coefficient: $C_p = 1.84$
Advance Radio: $J = 3.06$ ($\Omega R/U = .97$)
Number of Blades: $N = 8$
Blade Radius $R = 0.30$ m (1 ft.)
Freestream Mach Number: $M = .6$
Propeller Efficiency: $\eta_{eff} = .8$ (private communication)
Vane Semichord: $b = 0.15$ m (.5 ft.) (assumed)

From these, values are calculated for thrust coefficient and total propeller thrust of 2.1 N (.48 lb) and 963 N (215 lb), respectively. For the first (m=1) harmonic at the spanwise position y = 1.01 (so that $\tilde{w}_m \cong N$)

Eq. II-13 yields 20 $\log_{10}$ (L_{v_m}/P_{ref}) = 154 dB (Pref = 20 μPa) vs. the experimental value of about 143 dB. The rate of decay for the tonals may also be computed from Eq. II-13 and compared to measurement. Taking $m=8$, the level of the eighth harmonic will be down by 23 dB ($20 \log_{10}(1.01^{-65}/8)$) from that of the first harmonic.

Both of these results are shown in Fig. II-4b superimposed on measured values for comparison. Fairly good agreement is indicated, though predictions appear somewhat higher than measurement at the lower part of the spectrum. We put off momentarily discussion of possible reasons for discrepancy and briefly present a similar calculation for an actual aircraft.

Revell, et al.[12] have listed operating parameters for a typical business-size propeller drive aircraft. These are:

Tip speed = 243m/s (800 ft/sec)
Cruise speed = .8M
Propeller diameter = 2.2 m (7.2 ft)
Number of blades = 8
Cruising altitude = 9210 m (30,000 ft)

Using a value of 302 m/s (995 ft/sec) for the sound speed at 9210 m (30,000 ft), one calculates a flight speed of 242 m/s (796 ft/sec), and so $\Omega R/U \approx 1$. A value of $b = 0.91$ m (3 ft) is assumed for the semichord at the engine spanwise position. From Eq. II-13 then, at the spanwise wing points of maximum vortex loading one finds that for the first harmonic ($f = 283$ Hz),

$$20 \log_{10}[L_{v_{m=1}}(y=\pm 1)/P_{ref}=20\mu\text{Pa}] = 137 \text{ dB} \quad ,$$

a number comparable in magnitude to those measured and predicted for the airborne path (Ref. 1, Fig. 5).

F. Summary of Results

When comparing the theoretical results predicted here to experimental results, the fundamental question should be asked whether a significant portion of the measured pressure can be attributed to the unsteady-aerodynamic lift mechanism of the present model. The propeller wake effects measured in Ref. 3

were apparently interpreted there as locally high values of stagnation pressures induced by free vorticity. The original purpose of the vane was probably to provide a physical mount for sensing instruments, not to act as an aerodynamic mechanism through which additional vortex energy could be channeled into the structure.

The mechanism in our theoretical model is an aerodynamic "reaction" mechanism. Pressures predicted on the wing plane are due to the aerodynamic presence of the wing; they would vanish if the actual lifting surface were removed because they are the impermeable wing's lifting reaction to an incident unsteady flow. This resulting force driving the vane or wing is balanced by an equal and opposite net fluid force (Newton's first law) which in the immediate vicinity of the wing appears smeared over in the form of an acoustic near field. Since the theoretical model uses a flat-plate airfoil, those predicted pressures are antisymmetric with respect to the flight plane, so that on the two sides of the vane they are equal in magnitude but opposite in sign.

The fairly good agreement between theory and experiment suggests that the lift effect is significant, and that it can therefore serve as an efficient coupler of propeller wake energy to structureborne vibration. It should be pointed out, however, that as estimated here these levels probably represent conservative estimates for the mechanism. The model does not account for finite vortex core size, nor does it account for mutual three-dimensional effects of wing sections in the vortex-induced spanwise-varying downwash field. Both of these may be expected to lower levels somewhat due to their smoothing action.

Another possibly important neglected effect is that on vortex position and motion by an "image" system inside the wing. The model here allowed the propeller wake to cut freely through the wing plane, when in fact potential theory would call for a more complicated trajectory due to interaction with the solid surface.

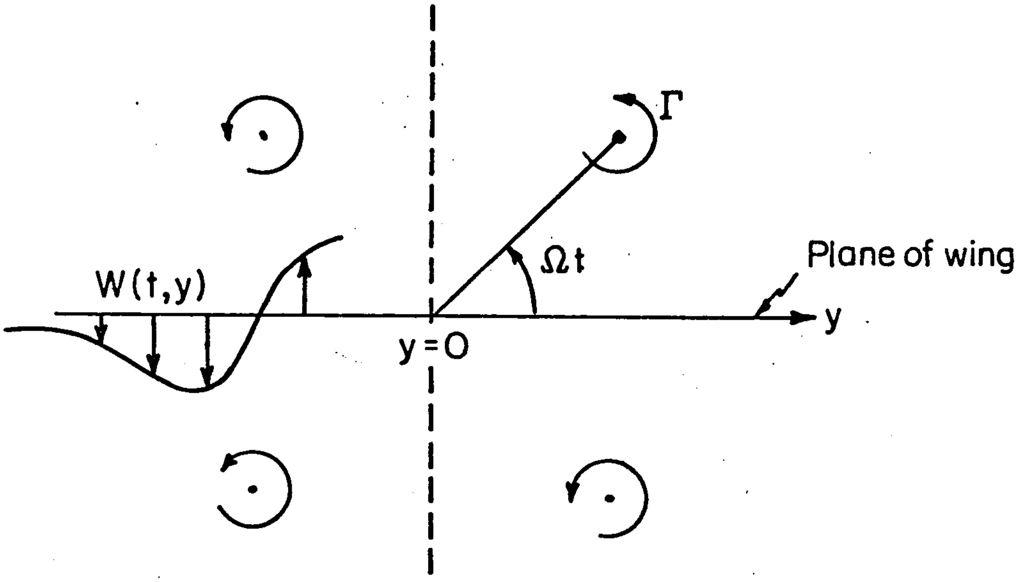

Fig. II.1 - Wake model for a four-bladed propeller, indicating horizontal plane of wing and vortex-induced downwash.

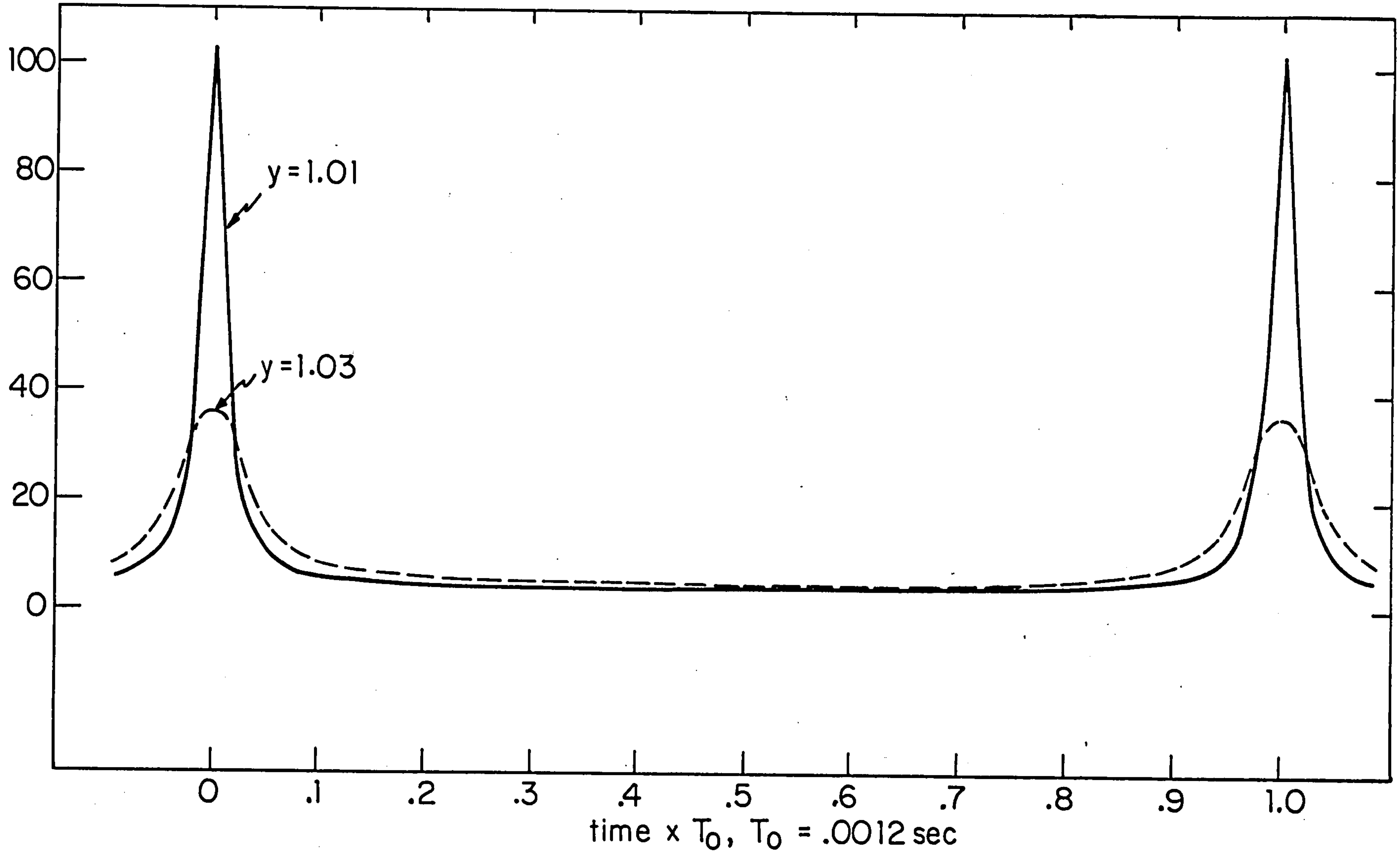

Fig. II.2 - Time history of $\bar{w}$, the normalized downwash function of Eqs. II-1 and II-2; N = 8, Ω = 640 rad/sec.

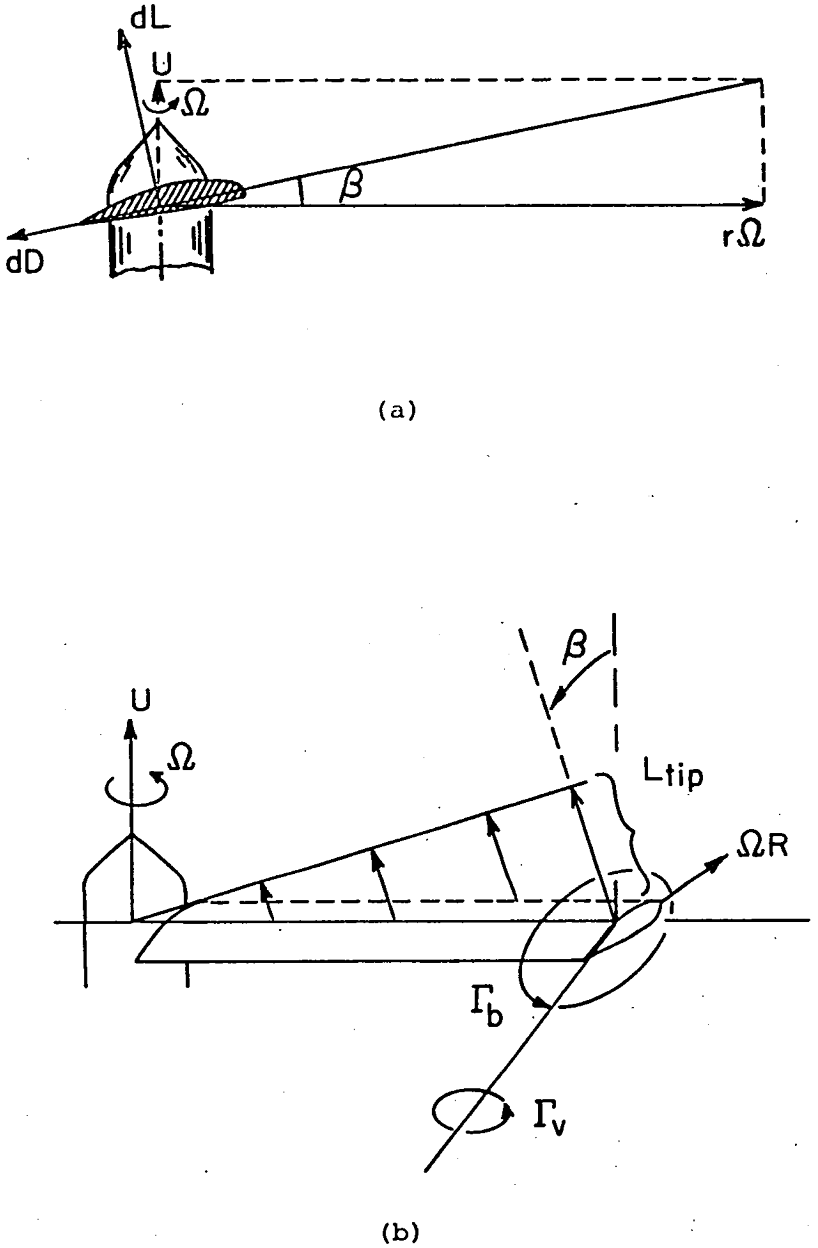

Fig. II.3 - (a) Blade forces acting at a typical blade motion a distance r from the hub.

(b) Linear distribution of lift and blade-tip vortex model.

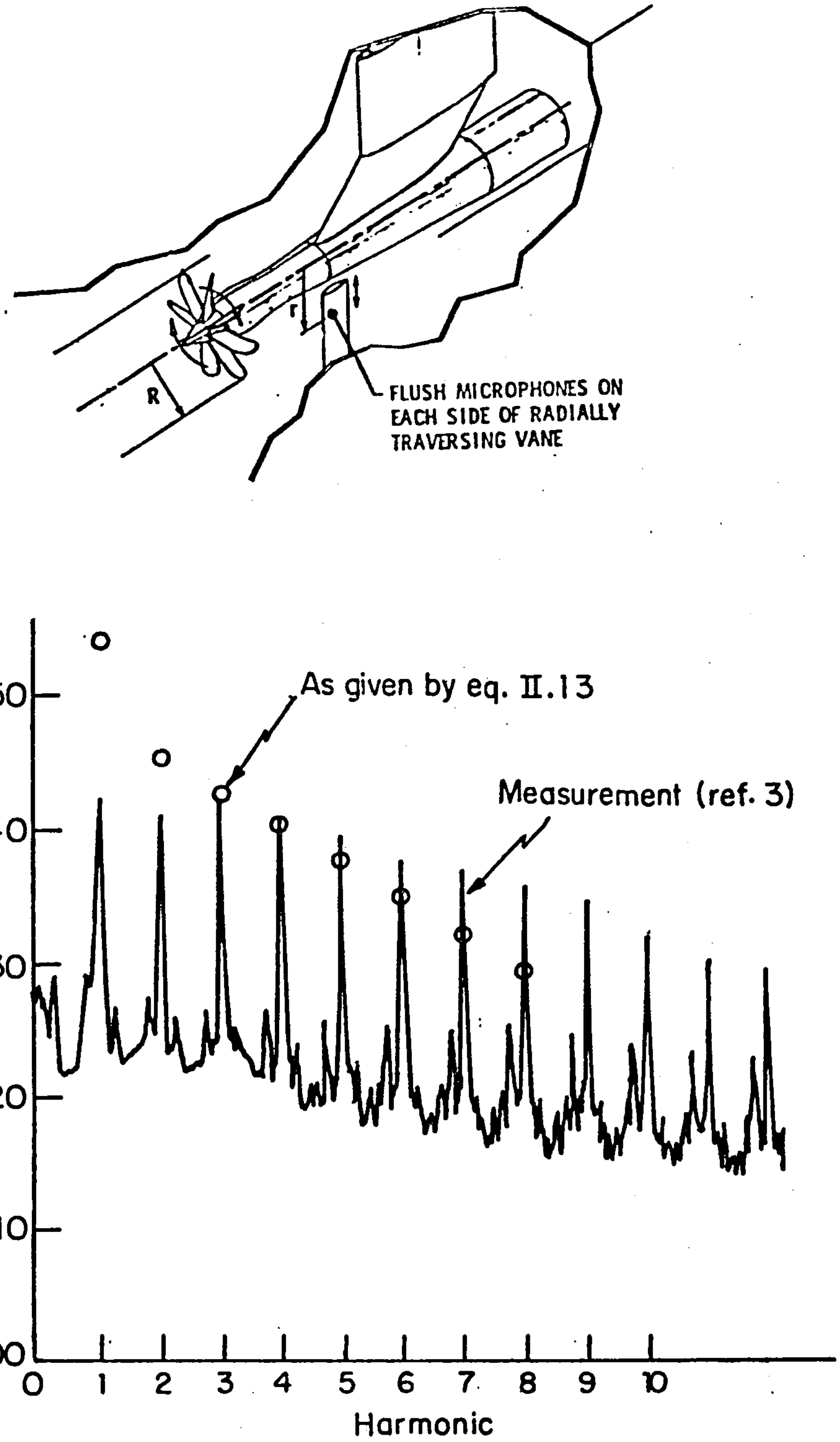

Fig. II.4 - (a) Laboratory model in Ref. 3.

(b) Comparison of theoretically predicted pressure harmonics (o) for y = 1.01 to experimental measurements (solid line); for N = 8, Ω = 640 rad/sec, r/R = 1.01.

III. STRUCTUREBORNE NOISE MODELS

A. Structureborne Noise Propagation Along a Wing Structure

1. Introduction

In the following sections the characteristics of structureborne noise propagation along a wing-like structure are analyzed. Basic concepts and functional analyses rather than extensive numerical modelling are emphasized.

First the relevant characteristics of the vibration source, as modelled in Chapter II, are summarized. Propagation along the (bare) skin is then analyzed followed by a discussion of the air/fuel space between skins. Scattering and radiation from ribs is examined as is the potentially beneficial impact of discrete stringers. Finally spar dynamics are considered followed by a summary of results.

2. Source Characteristics

As described previously the assumed source of structureborne noise on the wing is the unsteady lift associated with blade tip vortices. This driving force, as modelled, has the following general characteristics:

a. At a given spanwise position (y) measured from the propeller hub (y=0) the unsteady pressures on the top and bottom skins of the wing are equal in magnitude and opposite in phase.

b. The unsteady pressure (lift) is antisymmetric about y=0.

c. For y > 0, the unsteady lift at the m^{th} harmonic of the blade passage frequency N varies as $(y/R)^{\alpha}$ where R is the propeller blade radius. The quantity α is given by

$$\begin{aligned} \alpha &= (mN-1) \qquad 0 \leq y/R \leq 1 \\ &= -(mN+1) \qquad y/R \geq 1 \end{aligned} \qquad \text{(III-1)}$$

To account for the above three factors, we assume a normal pressure acting on the wing in the form

$$P(y;\omega) = P_o(\omega)\, f(y/R) \qquad \text{(III-2)}$$

where $P_o(\omega) = NL_{vm}(1)$ as defined in Eq. II-13,

$$f(y/R) \begin{cases} = -\mathrm{sgn}(y/R)\, |y/R|^{(mN-1)} & |y/R| \leq 1 \\ = \mathrm{sgn}(y/R)\, |y/R|^{-(mN+1)} & |y/R| \geq 1 \end{cases} \qquad \text{(III-3)}$$

and

$$\mathrm{sgn}(y/R) = \begin{cases} 1 & |y/R| > 1 \\ -1 & |y/R| < 1 \end{cases} \quad \text{(III-4)}$$

The maximum lift $P_o(\omega)$ is given in Chapter II where it was shown that for parameters typical of small aircraft $P_o(\omega) \approx 137$ dB re 20 μPa.

3. The Wing as a Flexural Waveguide

Wing structures consist of top and bottom skins with spanwise stringers, structurally connected to each other by means of a chordwise array of ribs and two (front and rear) spanwise spars (Fig. III-1). The unsteady lift acts mainly over the surface area of the skins and the resulting vibrations are transmitted to the fuselage along the parallel skin-stringer and spar structures.

We first consider the flexural response of the skins to the unsteady lift ignoring chordwise variations in both source and structure, that is we treat the wing as a one-dimensional (infinite) waveguide. The acceleration of the wing, $a(y;\omega)$, in response to a distributed harmonic pressure field, $p(y_s;\omega)$, is given by (Ref. 13, Chapt. 6)

$$a(y;\omega) = (-i\omega^2/4EIk_f^3) \int_{-\infty}^{\infty} p(y_s;\omega)\{\exp[ik_f|y-y_s|]+i\exp[-k_f|y-y_s|]\}dy_s \quad \text{(III-5)}$$

where ω is circular frequency and the relevant material and geometric properties of the wing are expressed in the parameters E (Young's modulus), I (cross-sectional moment of inertia) and k_f (flexural wavenumber), with

$$k_f = (\mu\omega^2/EI)^{\frac{1}{4}}(1+i\eta/4) \quad \text{(III-6)}$$

where μ is the wing mass density per unit length and η a structural loss factor to account for energy dissipation. (In Eq. III-5 stringers may be modelled only to the extent that they modify, on average, the parameters I, m and η.)

Non-dimensionalizing Eq. III-5 to the inertial response of the wing under the peak pressure,

$$A(\bar{y};\omega) = \mu a(\bar{y};\omega)/P_o(\omega) = (-i/4)\int_{-\infty}^{\infty} f(\bar{y}_s/\beta)\{\exp[i|\bar{y}-\bar{y}_s|]+i\exp[-|\bar{y}-\bar{y}_s|]\}d\bar{y}_s \qquad \text{(III-7)}$$

where $\bar{y} = k_f y$ and $\beta = k_f R$. Thus, as modelled, at a given harmonic of the blade passage frequency the normalized acceleration is a function of the distances from the propeller hub to the locations of the wing tip and the observer measured in terms of flexural wavelengths.

To this point we have not related the parameters of the mathematical model to specific wing properties. However, it is useful to keep in mind the range of parameters of interest. Material properties are assumed to be those of rolled aluminum and we take $E = 6.9\text{x}10^{10}$ Pa ($10\text{x}10^6$ psi) and $\rho = 2.7\text{x}10^3$ kg/m^3 ($2.53\text{x}10^{-4}$ lb.sec^2/in^4). Of concern is the fundamental propeller blade passage frequency, which as before, and corresponding to N=8, is taken to be 283 Hz, and its harmonics, $f_m = \omega/2\pi = 283$ m for integer m, R = 1.1 m (3.6 ft.) is a typical propeller blade radius. For a skin of (effective) thickness h(in) Eq. III-6 yields a flexural wavelength

$$\lambda_f(\text{in}) = 2\pi/k_f(\text{in}^{-1}) \doteq 2\pi 10^2[h(\text{in})/f(\text{Hz})]^{\frac{1}{2}} \approx 37[h(\text{in})/N]^{\frac{1}{2}} \qquad \text{(III-8)}$$

(Note: $\lambda_f(\text{in}) = .025\ \lambda_f(\text{m})$)

For example taking 48 Pa (1 psf) for the weight density of the skin, $h = 1.7\text{x}10^{-3}$ m (0.07 in.) and $\lambda_f \approx .25$ m (10 in.) at the assumed fundamental blade rate frequency of 283 Hz.

For illustrative purposes Eq. III-7 has been evaluated for the above sample parameters. The results are plotted in Fig. III-2 as a function of the non-dimensionalized spanwise distance $\bar{y}$. In these calculations η was taken to be $5\text{x}10^{-2}$ which is moderate. Also shown in Fig. III-2 is a plot of Eq. III-3 showing the spatial decay of the source pressure magnitude from its peak at $\bar{y} - k_f R \sim 27$.

Although not evident in Fig. III-2, as $\bar{y} \Rightarrow 0$, $A(\bar{y};\omega)$ goes to zero in accord with the assumed asymmetry of the source about $\bar{y}=0$. For values of $\bar{y} < k_f R$, wave propagation associated with the nonuniformity of the pressure field produces an interference pattern in the response curve. The on-average level is roughly 10 dB down from that which would obtain from a locally reacting inertial response to the maximum lift pressure (0 dB). For $k_f R < \bar{y} < 10^2$ the acceleration levels begin to decay exponentially due to structural damping. Finally if the graph was extended well beyond $\bar{y} = 10^2$, the curves for $A(\bar{y};\omega)$ and $f(\bar{y}/\beta)$ would eventually converge indicating that the local acceleration is dominated by the inertial response of the waveguide to the magnitude of the local pressure.

In the following sections some of the cross-sectional details of the wing are considered, namely the entrapped air or fuel between skins, rib scattering and radiation, stringers, and spars.

4. Entrapped Air/Fuel Between Skins

Air inertia relative to that of the wing structure can be dismissed a priori. In addition its compressibility may be dismissed primarily under the assumption of identical top and bottom skins since as discussed earlier the unsteady lifts on the skins are out of phase, that is there is no net compressive force on the wing cross-section as a whole. For example, modelling the skin-air layer-skin cross-section as an acoustic waveguide terminated by the inertia of the skins and assuming equal and out of phase pressures on the skins, (Fig. 3a) either skin acceleration is given by

$$\frac{\mu a(\bar{y};\omega)}{p_o(\omega)} = [2 - i\tan\gamma]/[2 - i\tan\gamma(1+i\sigma)] \qquad \text{(III-9)}$$

with $\gamma = \omega d/c$, $\sigma = \rho c/\omega\mu$ and where d represents the depth of the air cavity and ρc the density and sound speed of the entrapped fluid. For parameters of interest $\sigma << 1$ and the compressibility of the air layer may be dismissed for all frequencies.

On the other hand consider the situation that exists for those wing sections containing fuel. In this instance $\sigma > 1$ and $\gamma < 1$ for the frequencies of interest* and thus the fuel is effectively incompressible. The inertia of the fuel is large relative to that of the plating** causing a reduced (locally reacting) response of the skin covering these fuel tanks but also scattering of

---

* Assuming $(\rho c)_{fuel} = .75\ (\rho c)$ water and d = 0.15 m (6 in.), $\sigma \sim 3\text{x}10^4/f(\text{Hz})$ and $\gamma \sim 8\text{x}10^{-4} f(\text{Hz})$.

** For the assumed parameters $(\rho d)_{fuel}/(\rho h)_{skin} \sim 4d(\text{in}) >> 1$.

incoming vibrations propagating along the skin from the fuel tank boundaries. This latter phenomenon is discussed in detail in the following section in connection with ribs.

5. Rib Scattering and Radiation

Ribs present structural discontinuities to the skin-stringer structure, modifying its impedance and wave propagation properties but also causing sound radiation. To examine the effect of ribs on wave propagation we first model a single rib as a locally reacting structure with drive-point impedance Z_r (Fig. III-3b). We locate the rib at a nondimensionalized distance $\bar{y}_r$ from the propeller hub. The wing acceleration becomes

$$\frac{\mu a(\bar{y};\omega)}{P_o(\omega)} = \int_{-\infty}^{\infty} f(\bar{y}_s)g(\bar{y},\bar{y}_s)d\bar{y}_s+\bar{F}_r(\omega)g(\bar{y},\bar{y}_r) \qquad \text{(III-10)}$$

where

$$g(\bar{y},\bar{y}_s) = (-i/4)\exp[i|\bar{y}-\bar{y}_s|]+i\exp[-|\bar{y}-\bar{y}_s|] \qquad \text{(III-11)}$$

and $\bar{F}_r$ is the nondimensionalized rib reaction

$$\bar{F}_r(\omega) = F_r(\omega)k_f/P_o(\omega) \ . \qquad \text{(III-12)}$$

By imposing the constraint condition that

$$a(\bar{y}_r;\omega) = (i\omega/Z_r)F_r(\omega) \ , \qquad \text{(III-13)}$$

or

$$\frac{\mu a(\bar{y}_r;\omega)}{P_o(\omega)} = \bar{F}_r(\omega)/\bar{Z}_r \ , \qquad \text{(III-14)}$$

we may solve for the rib reaction

$$\bar{F}_r(\omega) = \frac{-\int \bar{f}(\bar{y}_s)g(\bar{y}_r,\bar{y}_s)d\bar{y}_s}{\bar{Z}_r^{-1}+g(\bar{y}_r,\bar{y}_r)} \qquad \text{(III-15)}$$

where

$$\bar{Z}_r^{-1} = -i\omega\mu/k_f Z_r \ . \qquad \text{(III-16)}$$

The wing acceleration in the presence of the rib may now be computed by substitution of Eq. III-15 into Eq. III-10. The result is shown in

Fig. III.4 for an infinite translational impedance rib ($\bar{Z}_r = \infty$) located one propeller radius from the wing tip ($\bar{y}_r = 2\beta \sim 54$). It is observed (compare Figs. III-2 and III-4) that although a null is indeed created at the rib location, beyond a quarter flexural wavelength away the effect is minor. It follows that the presence of an array of such ribs would be ineffective in reducing the vibrations reaching the fuselage unless the rib array spacing was less than a quarter flexural wavelength ($\lambda_f/4 \sim 0.062$ m (2.5 in.), for the illustrative example being considered).

Now let us increase the complexity of our rib model by allowing it to constrain the rotation as well as the translation of the wing. In this case the rib, by virtue of its rotational impedance Z_r^*, creates a concentrated couple (M_r) in addition to a transverse force (F_r). The acceleration field is now expressed by

$$\frac{\mu a(y;\omega)}{P_o(\omega)} = \int f(\bar{y}_s)\, g(\bar{y},\bar{y}_s)\, d\bar{y}_s + \bar{F}_r(\omega)\, g(\bar{y},\bar{y}_r) + i\bar{M}_r(\omega)\, \partial g(\bar{y},\bar{y}_r)/\partial y \qquad \text{(III-17)}$$

where

$$\bar{M}_r(\omega) = M_r(\omega)\, k_f^2/P_o(\omega) \quad .$$

By imposing the additional constraint that

$$\partial a(\bar{y}_r;\omega)/\partial\bar{y} = (i\omega/Z_r^*)\, M_r(\omega) \quad ,$$

or

$$\frac{\mu\partial a(\bar{y}_r;\omega)/\partial\bar{y}}{P_o(\omega)} = -\bar{M}_r(\omega)/\bar{Z}_r^* \quad , \qquad \text{(III-18)}$$

we obtain

$$\bar{M}_r(\omega) = \frac{\int f(\bar{y}_s)\, \partial g(\bar{y}_r,\bar{y}_s)/\partial\bar{y}\,[\mathrm{sgn}(\bar{y}_r-\bar{y}_s)]\, d\bar{y}_s}{\bar{Z}_r^{*-1} - i\partial^2 g(\bar{y}_r,\bar{y}_r)/\partial\bar{y}^2} \qquad \text{(III-19)}$$

with

$$(\bar{Z}_r^*)^{-1} = -i\omega\mu/k_f^3 Z_r^* \quad . \qquad \text{(III-20)}$$

By setting both $\bar{Z}_r^*$ and $\bar{Z}_r$ equal to infinity we create an effectively clamped boundary at $\bar{y} = \bar{y}_r$ thus blocking completely wave propagation across the rib. Accordingly the computed acceleration levels for $\bar{y} > \bar{y}_r$ (~27.) are caused solely by that portion of the pressure field extending beyond the rib. And it follows that for this case the excess propagation loss across the rib is primarily a function of (y/R), the distance of the rib from the hub measured in terms of the propeller blade radius, and should be approximated by $20 \log|y_r/R|^{-(mN+1)}$. For the parameters being considered, m=1, N=8 and $y_r/R = 2$, this expression yields -54 dB. Exact numerical results are shown in Fig. III-5.

Figs. III-4 and III-5 were computed assuming a rib with effectively infinite translational and rotational impedances relative to those of the skin. Nevertheless, given the large skin compliance, this is readily achieved. The criteria for accomplishing this end may be deduced from the denominator of Eqs. III-15 and III-19 and are given by

$$|Z_r|/2\sqrt{2}\ \omega\mu/k_f = \gamma > 1 \qquad \text{(III-21a)}$$

and

$$|Z_r^*|/2\sqrt{2}\ \omega\mu/k_f^3 = \gamma > 1$$

For example, assuming an inertial rib Eqs. III-21 are satisfied ($\gamma = 3$) for the example being considered by a rib with a cross-sectional area of 6.2×10^{-4} m^2 (1 $in.^2$) and rotational inertia of 9.8×10^{-7} m^4 (2.5 $in.^4$).

Having considered the influence of single ribs the question arises as to the effect of a ribbing array. For example it is well documented[14] that a periodically spaced array of ribs produces "pass" and "stop" frequency bands within which flexural waves in the plating either propagate freely, that is unattenuated in the absence of dissipation or, suffer an evanescent decay. However, given the thin and, in turn, low impedance wing skin, it has been shown that the criterion for achieving a very large impedance mismatch at each rib location for both translation and rotation is easily realizable (Eq. III-21). Also, for the problem at hand and as is the case for a single rib, the effectiveness of an array will be bounded by the direct excitation, it being distributed over the surface of the plating. Thus for the assumed parameters of interest, array effects (stop bands) are not considered to be a viable means for enhancing propagation loss along a wing beyond that implied by the multiple application of the above single rib analysis. Nor are array effects (pass bands) thought to be of concern in terms of short circuiting single rib effectiveness.

At this point it is informative to examine the dependence of the above predictions on N, the number of propeller blades. For this purpose the previous example was recalculated but for N=4 rather than 8. The frequency was held constant at 283 Hz. Results are shown in Fig. III-6 for the unribbed and fully constrained (in both translation and rotation) cases. Also shown in Fig. III-6 as a dotted line is the spatial variation in the source pressure magnitude which is now observed to decay more slowly. However for the unribbed case, the normalized acceleration levels themselves are relatively insensitive to the change in N, especially the decay in level beyond $\bar{y} = \beta$. This may be explained as follows. For large values of mN the effective source area is concentrated around $\bar{y} \approx \pm 1$, the locations of the wing tips. However, for the assumed parameters, the spatial decay in the source is still slow enough so that its effective correlation length exceeds the characteristic (flexural) wavelength in the skin. To obtain a measure of the net source strength we integrate the pressure over one quarter flexural wavelength from the (closest) wing tip. Using Eq. III-3 we obtain an effective moment acting on the waveguide of

$$M(\omega) = P(\omega)R^2 \int_{(1-\lambda_f/4R)}^{(1+\lambda_f/4R)} (\bar{y}_s - 1) f(\bar{y}_s/\beta) d\bar{y}_s \approx P(\omega)(\lambda_f/4)^2 \ , \quad \lambda_f/4R << 1 \tag{III-22}$$

which is invariant to N. The (far field) waveguide response to this line moment is given by

$$|A(\bar{y};\omega)| \approx (\pi/4)^2 \exp[-(\bar{y}-\beta)\eta/4] \ . \tag{III-23}$$

Eq. 23 has been plotted in Fig. III-6 where it is shown to compare favorably with the far field portion of the response curve computed using Eq. III-7.

While N has only a minor effect on the computed acceleration levels for the homogeneous structure, this is not the case in the presence of a strong structural discontinuity. For example, for the effectively rigid rib considered earlier, the transmission loss across it is roughly 50 dB when N=8 (Fig. III-5) but less than 30 dB for N=4 (Fig. III-6). This difference in rib effectiveness is directly attributable to the slower decay in the unsteady lift for N=4 and in turn a higher excitation level at and just beyond the rib location.

Although the subject of this work is the propagation of structureborne noise along the wing it is important to keep track of the acoustic radiation associated with these vibrations as this radiation impinging on the fuselage is also a potential source of cabin noise. This combined structureborne-airborne noise path can short circuit potential structureborne noise control measures.

To estimate this effect in connection with rib scattering we assume that the structureborne path has been blocked at some distance $\bar{y}_r$ from the propeller hub. That is, at spanwise distances $\bar{y} > \bar{y}_r$, the wing acceleration is zero. The pressure radiated along the wing surface may be approximated by (Ref. 13, p. 94),

$$p_r(y;\omega) = (\rho W/2\pi) \int_{-\infty}^{y_b} \{\exp[ik(y-y_s)]/(y-y_s)\}a(y_s;\omega)\,dy_s \qquad \text{(III-24)}$$

provided that $\alpha = \rho c/\omega m << 1$ and $(y-y_r) >> W$, where W is the average wing chord. In Eq. III-24 $k = \omega/c$ is the acoustic wavenumber. Rather than evaluate Eq. III-24 exactly for the acceleration fields computed earlier let us consider a simpler case.

The far field grazing radiation from a rigid piston centered about x=y=0, of rectangular dimensions $2L_x$, $2L_y$, and vibrating in an infinite baffle with acceleration amplitude a_o is (Ref. 13, p. 94)

$$|p_r(y-y_r;\omega)| = [\rho/2\pi(y-y_r)]4a_oL_x\sin(kL_y)/k \quad . \qquad \text{(III-25)}$$

We let $2L_x = W$ the wing chord. Also, since for the example under consideration we are below the critical frequency, that is $k_f >> k$, we allow $2L_y = \lambda_f/4$ or one quarter of a flexural wavelength, it being assumed that radiation from the remaining portion of the vibrating wing is minimized because of phase cancellation. This yields

$$|p_r(y;\omega)| \sim \rho Wa_o/4k_f y \qquad y >> y_r \quad . \qquad \text{(III-26)}$$

Normalizing this radiated pressure to the maximum source pressure

$$|p_r(y;\omega)/P_o(\omega)| \sim \rho Wa_o/4k_f yP_o(\omega)$$

$$= (4\sqrt{12}\ k/k_f)^{-1}(\rho/\rho_w)(c_w/c)(W/y)(\mu a_o/P_o(\omega)) \quad . \qquad \text{(III-27)}$$

For example, using the physical parameters of our example and a frequency of 283 Hz (m=1)

$$\left|P_r(y;\omega)(P_o/\omega)\right| \sim 4\times 10^{-3}(W/y)(\mu a_o/P_o(\omega)) \qquad \text{(III-28)}$$

Taking $\mu a_o/P_o(\omega)$ to be roughly unity (see Fig. III-5 with $\bar{y} \sim \bar{y}_r$) we see that, ignoring spherical spreading in the form of (W/y) the radiated pressure is down a considerable 48 dB from the maximum source pressure. Given the Chapter I estimate of $P_o(\omega)$ = 137 dB re 20 μPa for a typical maximum source pressure, it is concluded that this radiated field is negligible compared with the direct airborne path.

6. Discrete Stringers

To this point stringers have been modelled as being integral with the wing skins and thus accounted for only to the extent that they modify skin parameters yielding an effective stiffness or density. However, depending upon geometric details this approach may not be adequate. For example if the stringer impedance is large relative to that of the skin and if the stringer spacing is comparable to or exceeds the wavelength of freely propagating flexural waves in the skin then the stringer must be modelled in a discrete fashion. It is shown below that this situation provides a mechanism for potentially enhancing the propagation loss of structureborne noise along the wing over the bare skin, or integral skin-stringer case.

Consider the structure shown in Fig. III-7. The skin which is still taken to be of infinite spanwise extent is now taken to be not just a lifting line as before, but rather a lifting surface of finite chord, simply supported along its sides. These simple supports represent the stringers. Assuming an excitation pressure of the form $F(x,y) = R(x)\delta(y)$, the plating acceleration, which is now a function of x and y, must satisfy the partial differential equation

$$a_{yyyy}+2a_{yyxx}+a_{xxxx}-k_f^2a = -\omega^2[12(1-\nu^2)/Eh^3]f(x)\delta(y) \qquad \text{(III-29)}$$

The solution is in the form of a series

$$a(x,y;\omega) = \sum_n a_n(y)\sin(n\pi x/L) \quad . \qquad \text{(III-30)}$$

Taking the Fourier transform of Eq. III-29 with respect to y yields

$$[(k_y^4+2k_n^2k_y^2+k_n^4)-k_f^4]\bar{a}_n = f_n \qquad \text{(III-31)}$$

with

$$f_n = -\omega^2[12(1-\nu^2)/Eh^3](2/L)\int_0^L f(x)\sin(k_n x)\,dx \qquad \text{(III-32)}$$

and where $k_n = n\pi/L$ and k_y is the wavenumber corresponding to the y-transform variable. Inverting Eq. III-31 and assuming a uniform chordwise pressure of unit amplitude, that is $f(x) = 1$,

$$\mu a(x,y;\omega) = (-ik_f/2) \sum_{n=1,3,5} (2/n\pi)\sin(k_n x)G_n(\bar{y}) \qquad \text{(III-33a)}$$

with

$$G_n(\bar{y}) = (1-\kappa_n^2)^{-\frac{1}{2}}\exp[i(1-\kappa_n^2)^{\frac{1}{2}}\bar{y}]+i(1+\kappa_n^2)^{-\frac{1}{2}}\exp[-(1+\kappa_n^2)^{\frac{1}{2}}\bar{y}] \qquad \text{(III-33b)}$$

where $\kappa_n = k_n/k_f$ and as before, $\bar{y} = k_f y$.

Eq. III-33 may now be used as an influence function governing the wing response to the distributed lift defined previously but now in the presence of discrete stringers,

$$\mu a(x,\bar{y};\omega)/P_o(\omega) = (-i/2) \sum_{n=1,3,5...} (2/n\pi)\sin(k_n x)\int_{-\infty}^{\infty} f(\bar{y}_s/\beta)G_n(\bar{y}_s)\,d\bar{y}_s \ . \qquad \text{(III-34)}$$

Although detailed calculations using Eq. 34 could be performed it is sufficient, for present purposes, to examine the nature of the solution. Of principal interest is that Eq. III-33 implies a cutoff frequency below which $\kappa_n^2 > 1$ and therefore the acceleration decays exponentially with spanwise distance from the source.[15] The lowest cutoff frequency, corresponding to n=1, is given by $\kappa_1 = 1$ or $k_f L = \pi$.

For example, at one-half of this frequency $k_f L = \pi/\sqrt{2}$, and the minimum exponential decay (n=1) given by Eq. III-33 is $\exp[-(\pi/\sqrt{2})y/L]$. Thus, the decay at a spanwise distance from the source equal to only one stringer spacing (y=L) yields ~20 dB of attenuation.

Unfortunately this rather impressive effectiveness can be short-circuited by the flanking path created by the rigid body motion of the stringers. This places a restriction on the minimum size of the stringers, but fortunately only on a spanwise length comparable to the stringer spacing. For example, a 20 dB reduction in this rigid body motion requires a stringer to plating mass ratio of the order of ten.

Typical values of L may be estimated as follows. The cutoff criterion $k_f L = \pi$ yields $f(\text{Hz}) = \pi^2 10^4 h(\text{in})/L^2(\text{in}^2)$ $(= 2.5\text{x}10^3 h(\text{m})/L^2(\text{m}^2))$ for an aluminum skin. Thus, taking $h = 1.7\text{x}10^{-3}$ m (.07 in.) as before, a 0.10 m (4 in.) stringer spacing yields a cutoff frequency of 430 Hz, well beyond the assumed fundamental blade rate frequency of 283 Hz.

7. Wing Sweep and Spar Dynamics

In previous sections, with the exception of the discrete stringer analysis, wing dynamics were modelled one dimensionally, that dimension being the spanwise coordinate. This can be justified on the basis of the source model which predicts an average lift invariant to the chordwise dimension and the implied assumption of a wide wing with zero wing sweep. As a consequence, the structureborne noise propagation characteristics of the wing are dominated by those of the skins. In this section we consider the potential structureborne noise path along the spars, this path being parallel with and coupled to that along the skins.

The spars themselves not being directly exposed to the unsteady lift are excited via the ribbed skin structure. Since the overall surface area of the skin greatly exceeds that which is in direct contact with the spars, it is assumed here that spar motion is the result of propagating waves in the skin being coupled into the spars. This may be justified as follows.

Taking the chordwise variation in the unsteady lift to be of the form[16] $\chi(x) = \pi^{-1}[(b-x)/(b+x)]^{\frac{1}{2}}$ with the front spar located at $x = -b$, and where $b = W/2$, the wing semichord as defined in Chapter II, the integrated pressure acting on the skin over the chordwise distance $x_c > x > -W/2$ becomes

$$\bar{p}_c(x_c) = \int_{-W/2}^{x_c} \chi(x)\,dx = (W/\pi)[\pi/2+\sin^{-1}(2x_c/W)+(1-(2x_c/W)^2)^{\frac{1}{2}}] \quad .$$

If the effective force on the spar (per unit spanwise distance) is approximated as that acting on the adjacent skin extending out a chordwise distance of $\lambda_f/4$ then the ratio of this force to the overall force acting on the wing (per unit spanwise distance) is

$$\bar{p}_c(-W/2+\lambda_f/4)/\bar{p}_c(W/2) = (2/\pi)(\lambda_f/W)^{1/2} << 1 \qquad \lambda_f/W << 1 \quad .$$

To examine the skin-spar phenomenon we analyze the situation shown in Fig. III-7. A straight crested flexural wave propagating in a semi-infinite plate (skin) is incident on a beam (spar) of infinite extent at an angle given by ϕ. This angle may represent the sweep angle of the wing or another source of skew. The beam serves as the termination of the plating and is capable of sustaining both flexural and torsional waves. However we will simplify our analysis by ignoring coupling between torsional motion in the spar and in-plane or membrane motion in the skin. The analysis of this problem is straightforward and follows closely that given in Ref. 17. (In Ref. 17 an infinite rather than semi-infinite plate is analyzed.) A unit amplitude harmonically varying flexural wave is defined by

$$w_i(x,y) = \exp(ik_f y\sin\phi)\exp(ik_f x\cos\phi) \tag{III-35}$$

where ϕ is the incident angle on the beam measured from the x coordinate axis. Grazing incidence on the beam (spar) is given by $\phi = \pi/2$ and normal incidence by $\phi = 0$. The reflected wave takes the form

$$w_r(x,y) = \exp(ik_f y\sin\phi)+R\exp(-ik_f x\cos\phi)+R_N\exp(-k_f x(1+\sin^2\phi)^{1/2}) \tag{III-36}$$

The resulting translational motion of the spar (x=0) is given by

$$|w_s(y)| = |w(0,y)| = |w_i(0,y)+w_r(0,y)| = 1+R+R_N \tag{III-37}$$

and the (torsional) rotation of the spar is

$$|\partial w_s(y)/\partial x| = k_x|1-R+iR_N| \quad . \tag{III-38}$$

After expressing the interaction shears and moments in terms of the boundary motion the reflection coefficients R and R_N may be determined from continuity of displacement and slope. The result is the following set of simultaneous equations.

$$[A]\bar{R} = \bar{B} \tag{III-39}$$

with

$$\bar{R} = \begin{bmatrix} \bar{R} \\ \\ R_N \end{bmatrix}, \qquad \bar{B} = \begin{bmatrix} -S+1+\sin^2\phi-\nu\sin^2\phi \\ \\ iJ\cos\phi-(\cos^2\phi+\nu\sin^2\phi) \end{bmatrix}$$

,

and

$$[A] = \begin{bmatrix} S+i\cos\phi(1+\sin^2\phi-\nu\sin^2\phi) & S-\nu(1+\sin^2\phi)^{\frac{1}{2}}\sin^2\phi \\ iU\cos\phi+(\cos^2\phi+\nu\sin^2\phi) & U(1+\sin^2\phi)^{\frac{1}{2}}-(1+\sin^2\phi-\nu\sin^2\phi) \end{bmatrix}$$

with

$$S = (A_b k_f/h)[(c_b/c_p)^4\sin^4\phi-1] \qquad \text{(III-40)}$$

$$U = (Jk_f^3/h)[1-(c_t/c_p)^2\sin^2\phi] \qquad \text{(III-41)}$$

and where $c_t = c_s^2(K/J)^{\frac{1}{2}}$ and $c_b = (c(r_g)_b\omega)^{\frac{1}{2}}$ are the velocity of torsional and flexural waves in the beam and $c_p = (c(r_g)_p\omega)^{\frac{1}{2}}$ is the velocity of flexural waves in the plating. In the above equations $(r_g)_b$ and $(r_g)_p$ are the radii of gyration of the beam and plating respectively, and it has been assumed that the sound speed in both the beam and plating is c. The term c_s represents the shear velocity in the beam and K and J its cross sectional torsional constant and polar moment of inertia respectively. Also $h = \sqrt{12}(r_g)_p$ is the plating thickness and A_b the cross sectional area of the beam. It is noted from Eqs. III-39 that with the exception of Poisson's ratio ν, the dependence of the reflection coefficients on the physical parameters of the system is solely through the flexural parameter S and the torsional measure U. Once again our interest will be limited to an analysis of the nature of the solution dictated by the mathematical model.

First we observe that for grazing incidence ($\phi = \pi/2$), Eqs. III-39 reduce to

$$\begin{bmatrix} S & S-\sqrt{2}\nu \\ \nu & \sqrt{2}U-(2-\nu) \end{bmatrix} \begin{bmatrix} R \\ R_N \end{bmatrix} = - \begin{bmatrix} S \\ \nu \end{bmatrix} \qquad \text{(III-42)}$$

yielding $R = -1$ and $R_N = 0$. Thus for this (zero wing sweep) case we confirm that there is no coupling into the beam (spar). Although it is not particularly relevant to the problem posed, it is of general interest to explore the other extreme, namely normal incidence for which $\phi = 0$. Here Eqs. 39 reduce to

$$\begin{bmatrix} S+i & S \\ iU+1 & U-1 \end{bmatrix} \begin{bmatrix} R \\ R_N \end{bmatrix} = - \begin{bmatrix} S-i \\ 1-iU \end{bmatrix} \tag{III-43}$$

And it can be shown that under this circumstance

$$\mathop{\mathbf{L}}\limits_{S,U} |W_s(y)| \Rightarrow \begin{array}{ll} 0 & S \gg 1 \\ 4 & S,U \ll 1 \\ 2 & S \ll 1 \;,\quad U \gg 1 \end{array}$$

Physically, large values of S and U imply large translational and rotational beam impedances respectively, relative to the inertial impedance of the plating.

More relevant to the issue at hand, we now consider the solution to Eqs. III-39 for arbitrary values of ϕ but a variety of limiting cases for S and U. For $S \gg 1$, Eqs. III-39 yield the following solution for the reflection coefficients

$$\begin{bmatrix} R \\ R_N \end{bmatrix} = D^{-1} \begin{bmatrix} U(1+\sin^2\phi)^{\frac{1}{2}} - [1+(1-\nu)\sin^2\phi] & -1 \\ -[iU\cos\phi+\cos^2\phi+\nu\sin^2\phi] & 1 \end{bmatrix} \begin{bmatrix} -1 \\ iU\cos\phi-(\cos^2\phi+\nu\sin^2\phi) \end{bmatrix} \tag{III-44}$$

with

$$D = U[(1+\sin^2\phi)^{\frac{1}{2}} - i\cos\phi]-2 \;.$$

If in addition we assume $U \gg 1$ then Eqs. III-44 give $R+R_N \sim -1$ and therefore from Eq. III-37,

$$\mathop{\mathbf{L}}\limits_{S,U\Rightarrow\infty} W_s(y) = 0 \tag{III-45}$$

On the other hand if we assume $U \ll 1$ then Eqs. III-44 yield

$$\mathop{\mathbf{L}}\limits_{S\Rightarrow\infty,\, U=0} W_s(y) = \nu\sin^2\phi \;. \tag{III-46}$$

Similarly it can be shown from Eqs. III-39 that

$$\mathop{\mathbf{L}}\limits_{U\Rightarrow\infty,\, S=0} W_s(y) = (2+\sin^2\phi)/(1+\sin^2\phi) \;. \tag{III-47}$$

Thus, in the asymptotic limit of large translational and rotational spar impedances, there is no translational coupling into the beam. However, if either the translational or rotational coupling factors is negligibly small then the coupling is of the order unity.

The quantity S is small if either $A_b k_f/h << 1$ or $\sin\phi \sim (c_p/c_b)$. However, since for typical wing structures $A_b k_f/h >> 1$ only the latter condition is of interest. Taking the spar and skin to be of the same material $(c_p/c_b) = [(r_g)_p/(r_g)_b]^{\frac{1}{2}}$, and therefore there is strong coupling into the spar for incident angles

$$\phi_f \approx \sin^{-1}[(r_g)_p/(r_g)_b]^{\frac{1}{2}} \quad . \tag{III-48}$$

Similarly, since typically $Jk_f^3/h >> 1$ there is strong coupling into the beam for incident angles that satisfy $\sin\phi \sim (c_p/c_t)^{\frac{1}{2}}$ or

$$\phi_t \approx \sin^{-1}[(\pi/\sqrt{3})(c/c_s)\kappa^{-1}h_p/\lambda_c] \tag{III-49}$$

where the geometrical factor $\kappa = K/J$ and $\lambda_c = 2\pi c/\omega$ is the wavelength of compressional waves in the plating. Eqs. III-48 and III-49 are expressions for the angles at which there is wavenumber matching between flexural and torsional waves in the beam and flexural waves in the plating.

In order to evaluate the degree of coupling between wing skins and spars based on the above model, one first estimates the quantities S and U. To do so we hypothesize an aluminum spar, rectangular in shape, of thickness $t_s = 2h_p$ and height $H_s = 100\ h_p$ where the skin thickness $h_p = 1.7\text{x}10^{-3}$ m (.07 in.). Further we use $c/c_s = 1.7$ for aluminum $\kappa = 4(t/H)^2$ for a rectangular cross section,[18] and consider a frequency of 283 Hz. This yields $\phi_f \sim 6°$ and $\phi_t \sim 11°$ and thus strong coupling due to wavenumber matching occurs only near normal incidence. Also $A_b k_f/h = 8.8$ and $Jk_f^3/h = 14.2$. Therefore, if we somewhat arbitrarily assume a wing sweep of 30° and take this as our angle of incidence then for the above parameters $S,U > 10$. From these large values little coupling is expected between the (bare) skin motions and the front and rear spars.

Although beyond the present scope, it should be noted that the above conclusion may not hold in the event that the effective skin thickness is significantly larger than assumed or if there are large rib motions coupling well into the spars. Also, in this discussion the translational motion of the spar was taken as a measure of coupling while in practice spar rotations are also relevant.

8. Summary of Results

The more salient results from Sections III.A.1 through III.A.7 are summarized below.

a. For a rib to enhance significantly the propagation loss along a wing it must constrain both the translational and rotational motion of the skin. The criteria for achieving this objective appear to be realizable with minimum weight penalty. In practice rib effectiveness will be limited by rib elasticity which reduces its scattering strength and allows more efficient propagation across and coupling into it, both effects leading to an increase in cabin noise, the latter via the rib-spar-fuselage path.

b. Sound radiation (airborne) associated with structureborne noise scattering from structural discontinuities along the wing is negligible compared with the direct acoustic path.

c. Stringers that are small and in effect structurally integral with the skin have minimal impact on propagation along the wing. However, cut-off phenomena associated with a parallel array of discrete stringers could be created and exploited to enhance propagation loss. For an illustrative example the criterion for effectiveness is given as $k_f L < \pi$, where k_f is the (frequency dependent) wavenumber of flexural waves in the skin and L the interstringer spacing. Also, the (spanwise) length of the stringer array need only measure a flexural wavelength in the skin and therefore entails minimum weight penalty.

d. Spar vibration levels directly excited by the unsteady lift are less than those in the skin near the midchord. Also, in the absence of stiffeners, either ribs or stringers, or extreme wing sweep, coupling of structureborne noise from the skin into the spars is minor. The extent of coupling from the skin to spars in the presence of ribs has not been determined, and in view of the previous conclusions this skin-rib-spar-fuselage path may be the dominant one for typical wing configurations.

B. Wing-Fuselage Interaction

1. Introduction

In this section a simplified analytical model of a fuselage that is structurally connected to a wing is presented. In an aircraft the frame of the wing, namely the front and rear spars, is structurally connected to that of the fuselage via a geometrically complex structure, shielded somewhat from the passenger compartment of the cabin. Thus structureborne noise levels in the spars will be attenuated to some extent as they propagate through the fuselage and eventually radiate as cabin noise. For an aircraft the detailed modelling of the wing-fuselage structure is beyond the scope of this report. Nevertheless, to examine some of the characteristics of wing-fuselage interactions and to simulate a laboratory experiment recently performed at NASA/Langley a simplifed analyticalmodel is studied. In this model the fuselage is represented by a uniform cylindrical shell while the wing is modelled as a freely supported beam. Coupling between the beam and shell occurs along the width of the beam (i.e., chord of the wing) where the shell and beam intersect. Along these lines of contact the wing imparts both shear and moment reaction loads to the fuselage. If the beam is assumed to pass through the center of the shell, the reactions of the beam on the shell are an in-plane load and a moment. In this fully coupled structural model the effects of stiffeners in the form of circumferential frames or longitudinal stringers as well as the effects of loading on the shell imposed by the internal fluid are neglected. The latter effects are discussed further in Chapter IV. These effects are considered separately using a model of a frame stiffened shell that is described at the end of this section.

2. Unstiffened Fuselage

Figure III.8a, b, and c shows the geometric idealization for the analysis of the wing-fuselage system. The wing, modelled as a beam of length L_w, passes through the diameter of simply supported cylindrical shell of length L_f (w and f subscripts respectively denote wing and fuselage). Stiffening frames and stringers are not included in the analytical model that follows; however, the effects of frames are examined in Section III.C. As indicated in the wing free body, the structural effect of the shell is modelled as a set of unknown normal-to-beam forces and moment reactions at the two points of contact. For the shell analysis these same forces and moments are assumed smeared over, or distributed along, the width of the beam (root chord in an actual aircraft).

Displacements and rotations at the two contact locations may be independently expressed for beam and shell in terms of respective structural admittance matrices and the unknown load vector (for the beam the known exciting force F_o also takes part). Finally equating displacements and rotations for the two systems at their two points of intersection one obtains a set of 4 simultaneous equations (2 degrees of freedom x 2 points of contact) from which the unknown forces may be calculated. For the shell we have chosen the center chord point z_o in the displacement calculation for continuity with the beam motion. Thus the symmetric coupled system becomes,

$$\begin{bmatrix} c_{11}-Kc^*_{11} & c_{12}-Kc^*_{12} & c_{12}-Kc^*_{13} & c_{14}-Kc^*_{14} \\ & c_{22}-Kc^*_{22} & c_{23}+Kc^*_{14} & c_{24}+Kc^*_{13} \\ & & c_{33}-Kc^*_{33} & c_{34}-Kc^*_{34} \\ & & & c_{24}-Kc^*_{33} \end{bmatrix} \begin{bmatrix} F_1 \\ F_2 \\ M_1/a \\ M_2/a \end{bmatrix} = \begin{bmatrix} c_{01} \\ c_{02} \\ c'_{01} \\ c'_{02} \end{bmatrix} \cdot F_o \qquad \text{(III-50)}$$

where the constants c_{11}, c_{12}, etc., form the admittance matrix of the wing, and c^*_{11}, c^*_{12}, etc., that of the shell. These are all given below. The nondimensional parameter K gives some indication of the relative importance of the beam and of the shell in the combined admittance matrix. It is given by

$$K = \frac{4(1-\nu_f^2)\left(\frac{I_w}{ha^3}\right)\left(\frac{E_w}{E_f}\right)}{\pi L_f}$$

Here L_f, as all wavenumbers and other spatial quantities except a, h, and I_w in what follows, appears normalized by the shell radius a. I_w, E_w stand respectively for the moment of inertia of the beam about its cross-sectional horizontal axis, and E_w for the beam's Young's modulus. E_f, ν_f, h, and a are shell values of Young's modulus, Poisson's ratio, thickness and radius.

The beam constants are expressed in terms of free-free beam eigenfunctions[19]

$$\psi_m(x) = \frac{\sinh k_{fm}x + \sin k_{fm}x + C(\cosh k_{fm}x + \cos k_{fm}x)}{\sqrt{N_m}\ \sqrt{k_{fm}^4 - k_f^4}} \qquad \text{(III-51)}$$

where

$$N_m = \frac{1}{k_{fm}} \left\{ \frac{1}{8} \left[(1+C)^2 e^{2k_{fm}L_w} - (1-C)^2 e^{-2k_{fm}L_w} \right] \right.$$

$$+ \frac{\sin k_{fm}L_w}{2} \left[(1+C)^2 e^{k_{fm}L_w} + (1-C)^2 e^{-k_{fm}L_w} \right]$$

$$+ (C^2-1) \left[\sinh k_{fm}L_w \cos k_{fm}L_w + \frac{\sin 2k_{fm}L_w}{4} \right]$$

$$\left. + C \left[-\frac{1}{2} + \sin^2 k_{fm}L_w + Ck_{fm}L_w \right] \right\}$$

$$C = \frac{\sinh k_{fm}L_w - \sin k_{fm}L_w}{\cos k_{fm}L_w - \cosh k_{fm}L_w}$$

$$k_{fm}L_w = \frac{\pi}{2}\,(3.0112,\ 5,\ 7,\ 9,\ \ldots)$$

$$k_f^2 = \frac{\omega a}{c_p}\ \frac{1}{r_g}$$

where r_g is the beam's radius of gyration (normalized by a) for its cross-sectional horizontal axis.

The beam system's constants are

$$c_{11} = \sum_m \psi_m^2(x_1) - \frac{1}{k_f^4 L_w} \left[1 + \frac{12(x_1-L_w/2)^2}{L_w^2} \right] \qquad \text{(III-52)}$$

$$c_{12} = \sum_m \psi_m(x_1)\psi_m(x_2) - \frac{1}{k_f^4 L_w^3} \left[1 - \frac{12(x_1-L_w/2)^2}{L_w^2} \right]$$

$$c_{13} = \sum_m \psi_m'(x_1)\psi_m(x_1) - \frac{12}{k_f^4 L_w^3}\,(x_1-L_w/2)$$

$$c_{14} = \sum_m \psi_m(x_2)\psi_m(x_1) - \frac{12}{k_f^4 L_w^3}\,(x_1-L_w/2)$$

$$c_{22} = \sum_m \psi_m^2(x_2) - \frac{1}{k_f^4 L_w}\left[1 + \frac{12(x_1 - L_w/2)^2}{L_w^2}\right]$$

$$c_{23} = \sum_m \psi_m'(x_1)\psi_m(x_2) + \frac{12}{k_f^4 L_w^3}(x_1 - L_w/2)$$

$$c_{24} = \sum_m \psi_m'(x_2)\psi_m(x_2) + \frac{12}{k_f^4 L_w^3}(x_1 - L_w/2)$$

$$c_{33} = \sum_m \psi_m'^2(x_1) - \frac{12}{k_f^4 L_w^3}$$

$$c_{34} = \sum_m \psi_m'(x_1)\psi_m'(x_2) - \frac{12}{k_f^4 L_w^3}$$

$$c_{44} = \sum_m \psi_m'^2(x_2) - \frac{12}{k_f^4 L_w^3}$$

$$c_{01} = \sum_m \psi_m(x_o)\psi_m(x_1) - \frac{1}{k_f^4 L_w}\left[1 + \frac{12}{L_w^2}(x_o - L_w/2)(x_1 - L_w/2)\right]$$

$$c_{02} = \sum_m \psi_m(x_o)\psi_m(x_2) - \frac{1}{k_f^4 L_w}\left[1 - \frac{12}{L_w^2}(x_o - L_w/2)(x_1 - L_w/2)\right]$$

$$c_{01}' = \sum_m \psi_m(x_o)\psi_m'(x_1) - \frac{12}{k_f^4 L_w^3}(x_o - L_w/2)$$

$$c_{02}' = \sum_m \psi_m(x_o)\psi_m'(x_2) - \frac{12}{k_f^4 L_w^3}(x_o - L_w/2)$$

The shell constants may be obtained from analysis for thin cylindrical shells in Ref. 13, p. 237. The shell system's constants are

$$c_{11}^* = \sum_m \frac{\sin\frac{m\pi z_o}{L_f}\,\sin\frac{m\pi}{2}\frac{\Delta L_f}{L_f}}{m\pi\,\frac{\Delta L_f}{L_f}}\;\sum_n \frac{a_{11}a_{33} - a_{13}^2}{\det}\;\frac{1}{\varepsilon_n} \tag{III-53}$$

$$c_{12}^* = -\sum_m \frac{\sin\frac{m\pi z_o}{L_f}\,\sin\frac{m\pi}{2}\,\frac{\Delta L_f}{L_f}}{m\pi\,\frac{\Delta L_f}{L_f}}\ \sum_n (-1)^n \left(\frac{a_{11}a_{33}-a_{13}^2}{\det}\right)\frac{1}{\varepsilon_n}$$

$$c_{13}^* = -\sum_m \frac{\sin\frac{m\pi z_o}{L_f}\,\sin\frac{m\pi}{2}\,\frac{\Delta L_f}{L_f}}{m\pi\,\frac{\Delta L_f}{L_f}}\ \sum_n n\left(\frac{a_{13}a_{12}-a_{11}a_{23}}{\det}\right)$$

$$c_{14}^* = -\sum_m \frac{\sin\frac{m\pi z_o}{L_f}\,\sin\frac{m\pi}{2}\,\frac{\Delta L_f}{L_f}}{m\pi\,\frac{\Delta L_f}{L_f}}\ \sum_n (-1)^n \left(\frac{a_{13}a_{12}-a_{11}a_{23}}{\det}\right)$$

$$c_{33}^* = \sum_m \frac{\sin\frac{m\pi z_o}{L_f}\,\sin\frac{m\pi}{2}\,\frac{\Delta L_f}{L_f}}{m\pi\,\frac{\Delta L_f}{L_f}}\ \sum_n n^2\left(\frac{a_{11}a_{22}-a_{12}^2}{\det}\right)$$

$$c_{34}^* = \sum_m \frac{\sin\frac{m\pi z_o}{L_f}\,\sin\frac{m\pi}{2}\,\frac{\Delta L_f}{L_f}}{m\pi\,\frac{\Delta L_f}{L_f}}\ \sum_n (-1)^n \left(\frac{a_{11}a_{22}-a_{12}^2}{\det}\right)$$

where

$$\varepsilon_n = \begin{cases} 2 \text{ for } m = 0 \\ 1 \text{ for } n \geq 1 \end{cases}$$

$$a_{11} = \Omega^2 - \frac{1-\nu_f}{2}\ n^2 - \left(\frac{m\pi}{L_f}\right)^2$$

$$a_{12} = -\left(\frac{1+\nu_f}{2}\right) n \left(\frac{m\pi}{L_f}\right)$$

$$a_{13} = \nu_f \frac{m\pi}{L_f}$$

$$a_{22} = \Omega^2 - \left(\frac{1-\nu_f}{2}\right)(1+\beta^2)\left(\frac{m\pi}{L_f}\right)^2 - n^2(1+\beta^2)$$

$$a_{23} = -n\left[1 + \beta^2\left\{\left(\frac{m\pi}{L_f}\right)^2 + n^2\right\}\right]$$

$$a_{33} = \Omega^2 - 1 - \beta^2\left[\left(\frac{m\pi}{L_f}\right)^2 + n^2\right]^2$$

$$\det \equiv \begin{vmatrix} a_{11} & a_{12} & a_{13} \\ & a_{22} & a_{23} \\ & & a_{33} \end{vmatrix}$$

$$\Omega = \frac{\omega a}{c_p} / \sqrt{1-i\eta_f}$$

$$\beta = \frac{h/a}{\sqrt{12}}$$

and where η_f stands for the shell loss factor.

C. Model of Frame-Stiffened Cylinder

The external fuselage is a shell that is stiffened by both circumferential frames and axial stringers. In the laboratory test cylinder discussed in Section V the shell is coupled to a beam through either of these stiffeners by bolt attachments. The analytical model of the coupled beam and shell discussed in the previous section does not include internal stiffeners. In order to examine the effects of these structural elements, the structural response field of a frame stiffened cylindrical shell with internal fluid in response to localized circumferential force and moment excitations is examined. These excitations can be viewed as providing influence functions (i.e., pressure per shell load) for the coupled problem of a shell and wing.

The analytical model of the framed stiffened cylinder assumes the shell to be simply supported. The model allows the interior fluid loading to be included in calculating the shell response. The frames are modeled as rings, having three translational degrees of freedom as well as rotation aligned with the circumferential direction. The impedance matrix for the frame dynamics is given in Ref. 20. Coupling between the shell and frames is assumed to occur through line reaction loads at each frame location. Excitation loads are applied at the centroid of the cross section of the driven frame. Under these assumptions each circumferential mode of the shell couples to the frames and the reaction loads for a given circumferential mode are obtained by solving a system of equations equal to 4 (frame degrees of freedom) times the number of frames. The terms in each equation involve a sum over the axial modes of the shell. Once the frame reactions are known, they are applied one-by-one to the shell to calculate the response. The contribution of any particular frame to the response can therefore be examined by omitting it and noting the change in the response. As discussed in Chapter V, this procedure is useful for examining the importance of specific structural elements to the response and interior sound field.

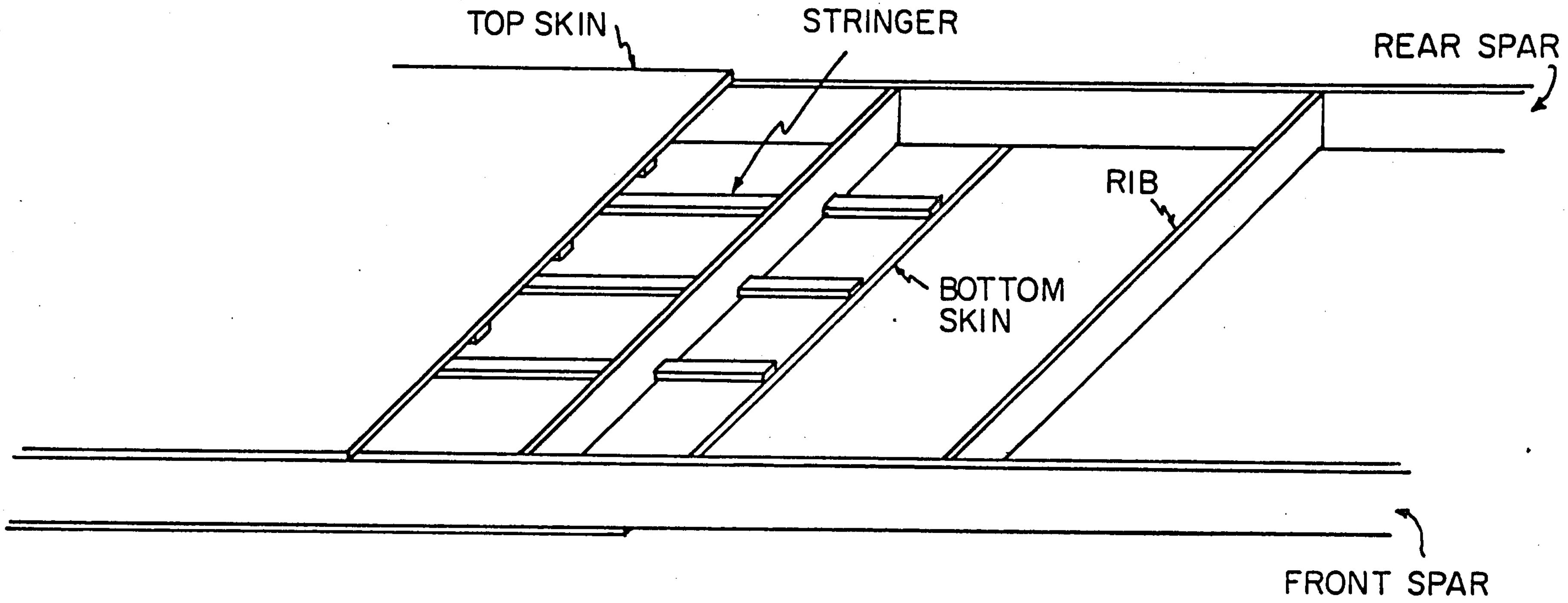

Fig. III.1 - Schematic of Wing Structural Components

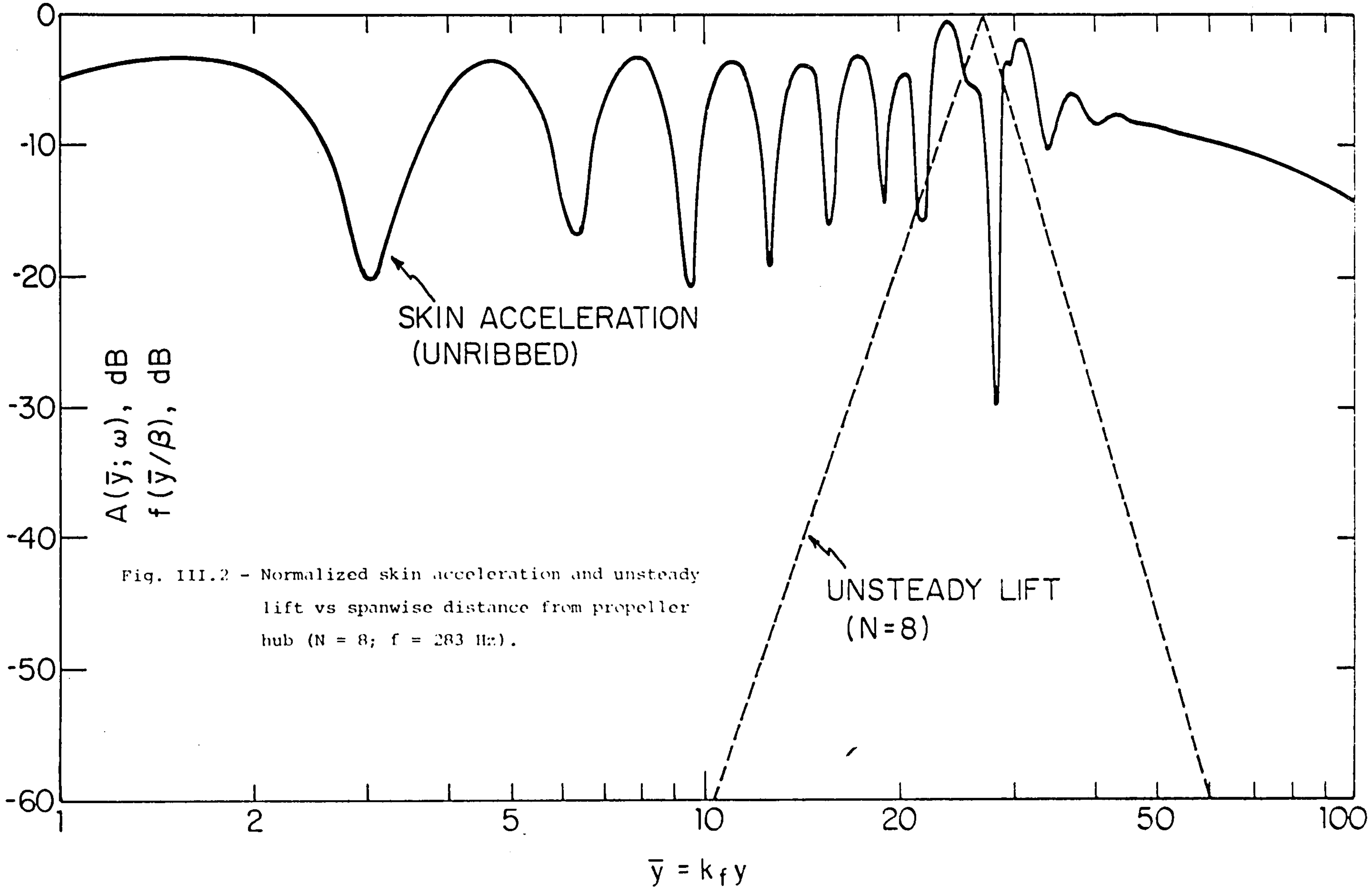

Fig. III.2 - Normalized skin acceleration and unsteady lift vs spanwise distance from propeller hub ($N = 8$; $f = 283$ Hz).

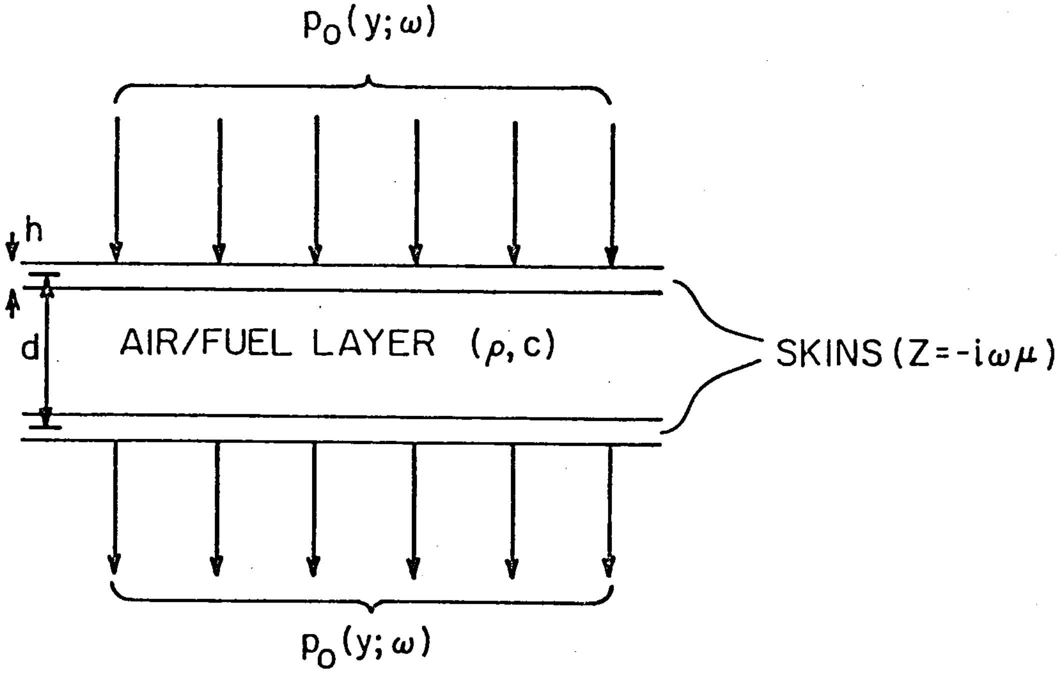

Fig. III.3a - Mathematical model of skin-air/fuel layer interaction.

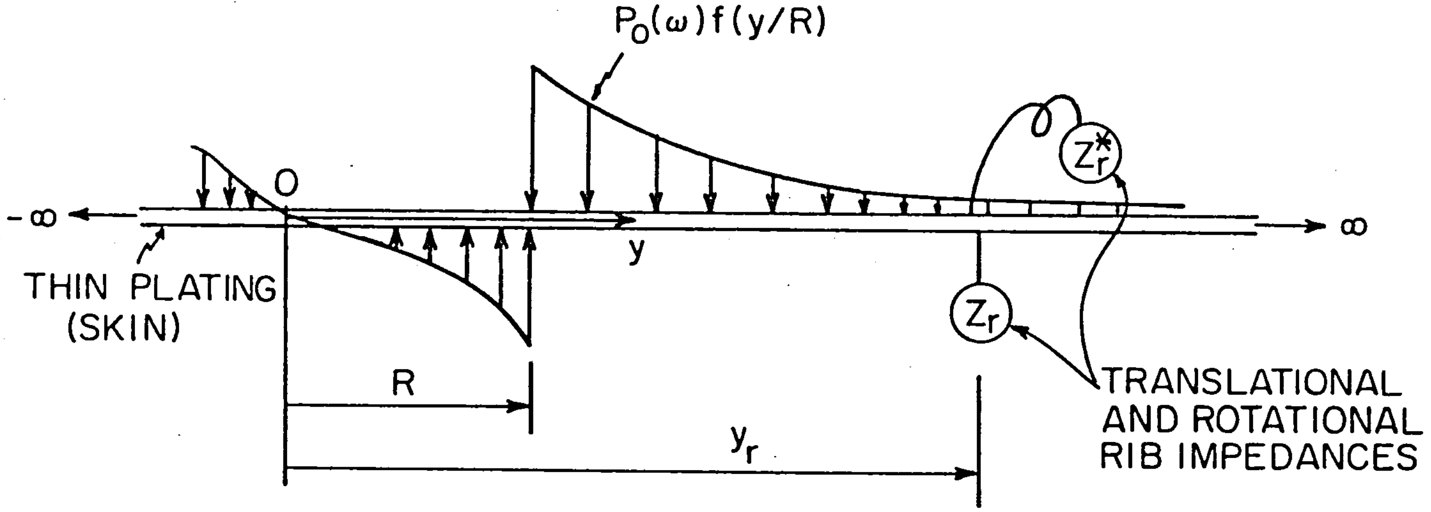

Fig. III.3b - Mathematical model for skin-rib interaction.

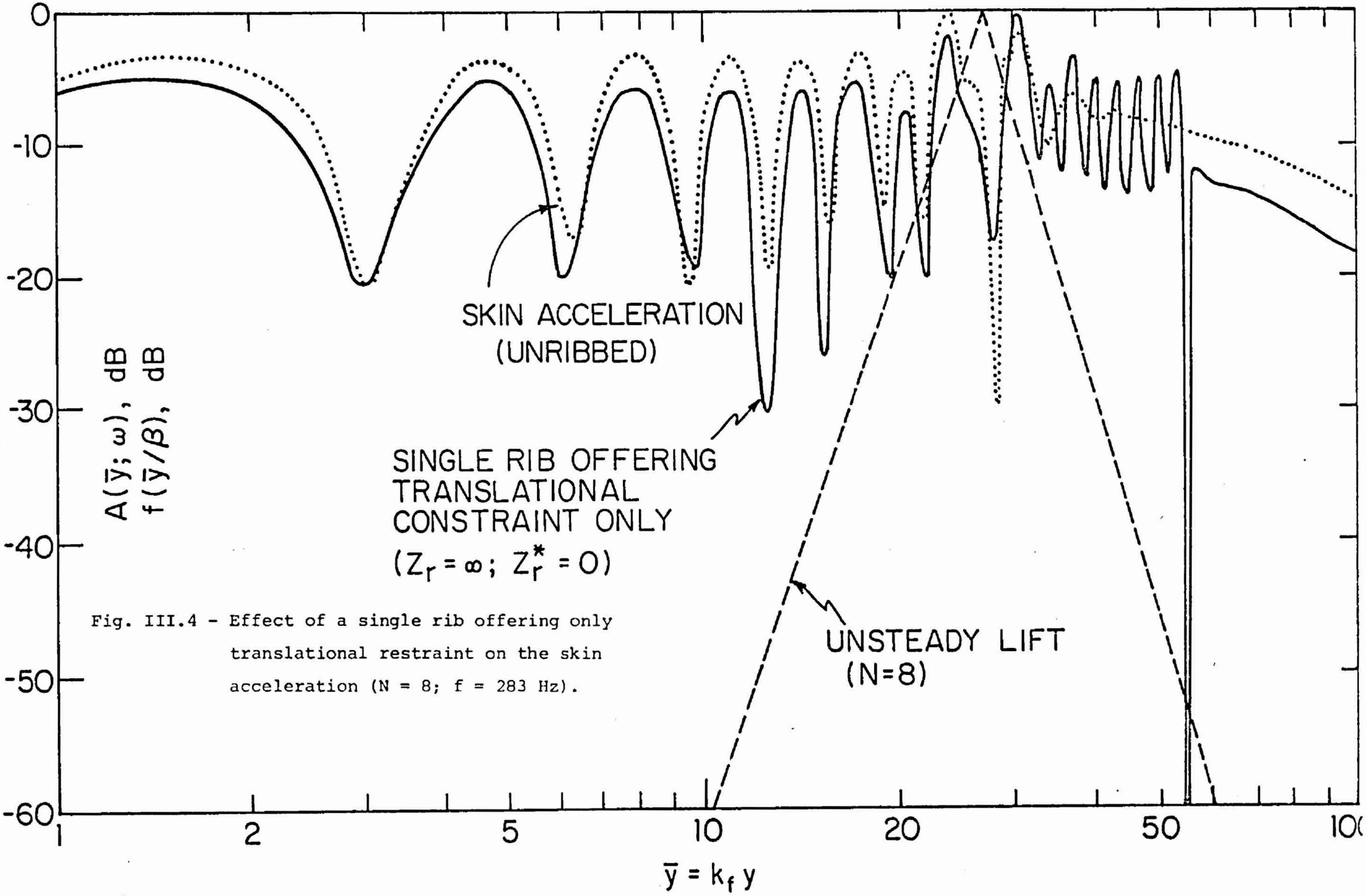

Fig. III.4 - Effect of a single rib offering only translational restraint on the skin acceleration ($N = 8$; $f = 283$ Hz).

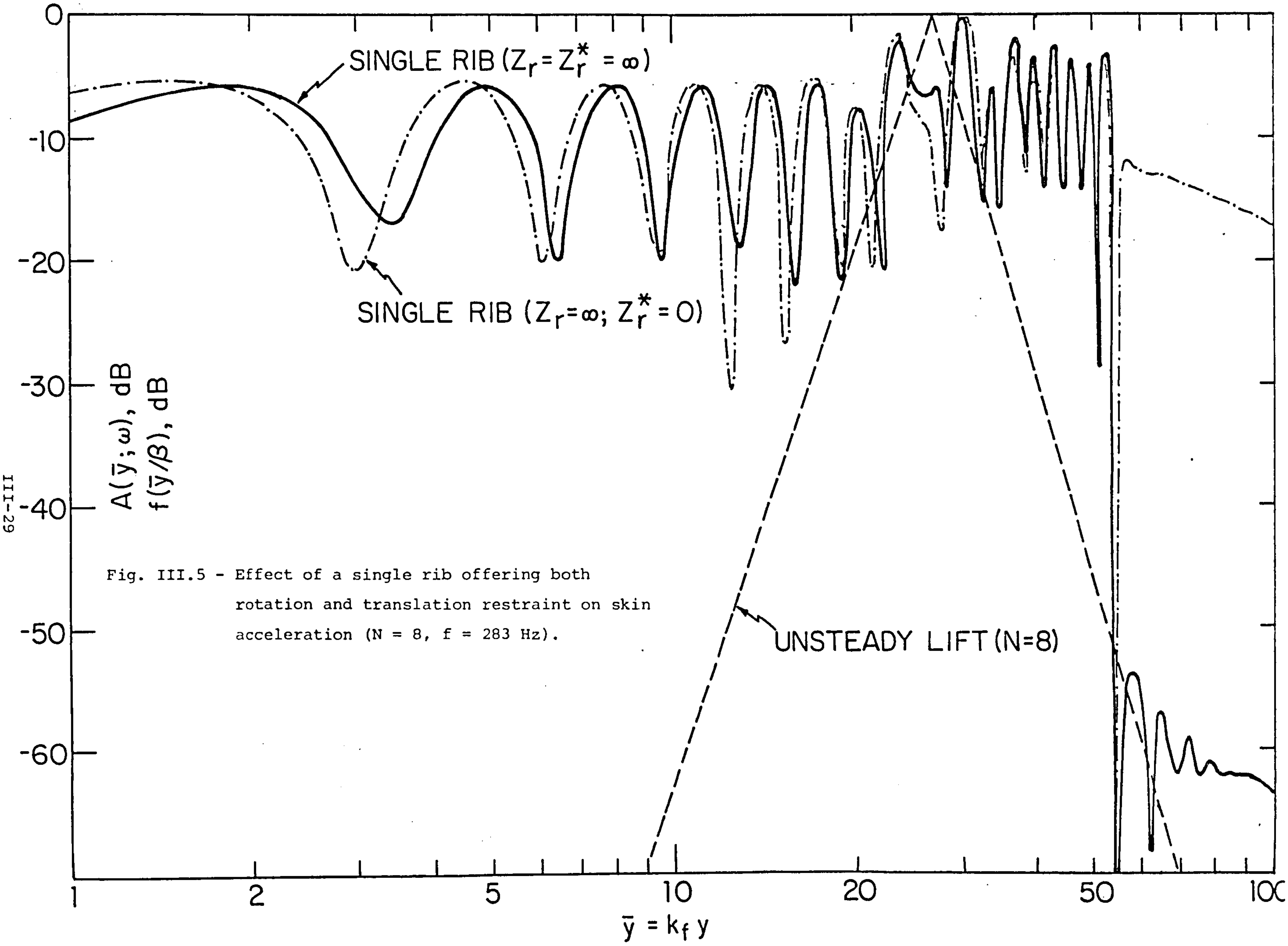

Fig. III.5 - Effect of a single rib offering both rotation and translation restraint on skin acceleration (N = 8, f = 283 Hz).

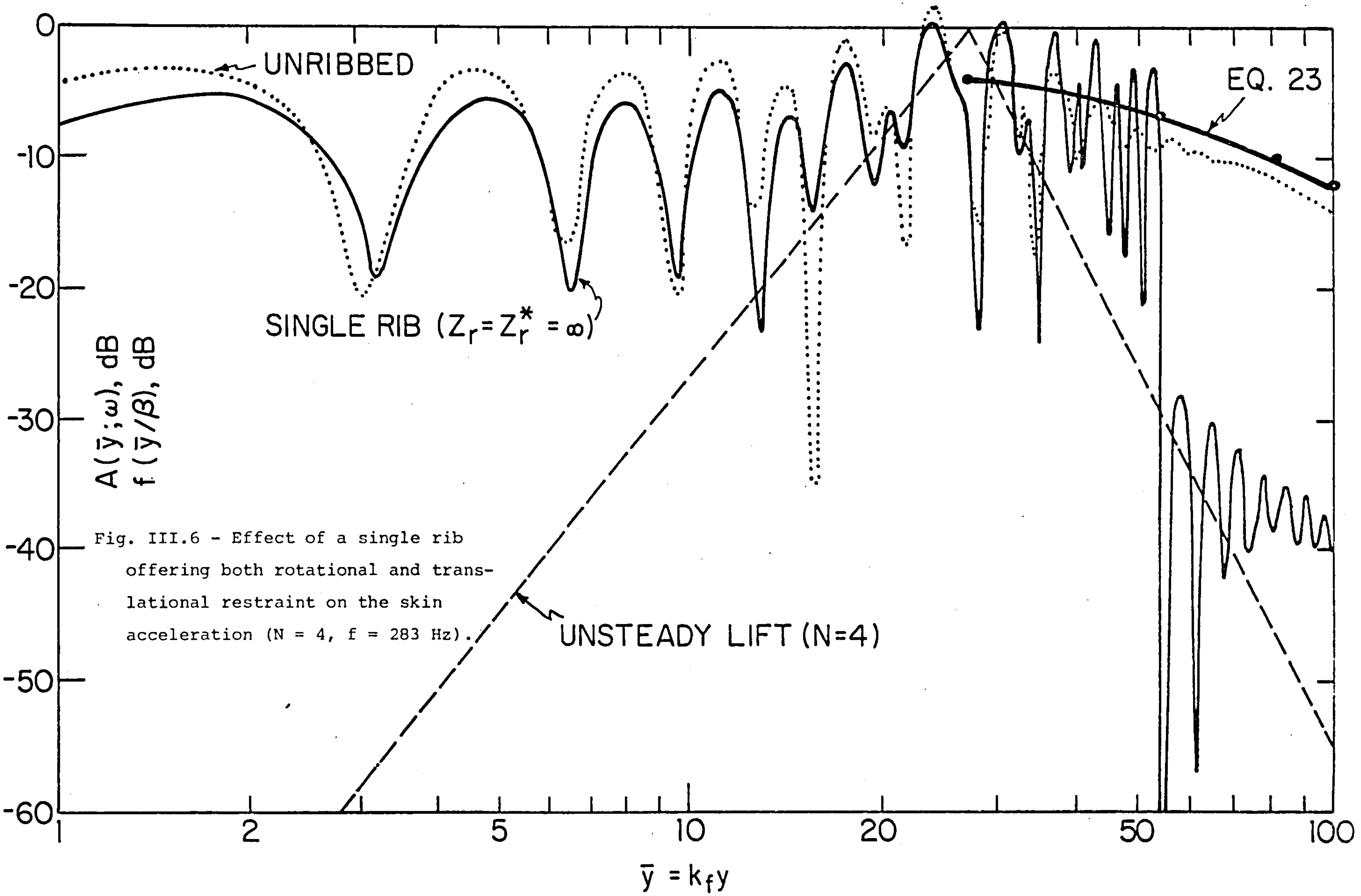

Fig. III.6 - Effect of a single rib offering both rotational and translational restraint on the skin acceleration (N = 4, f = 283 Hz).

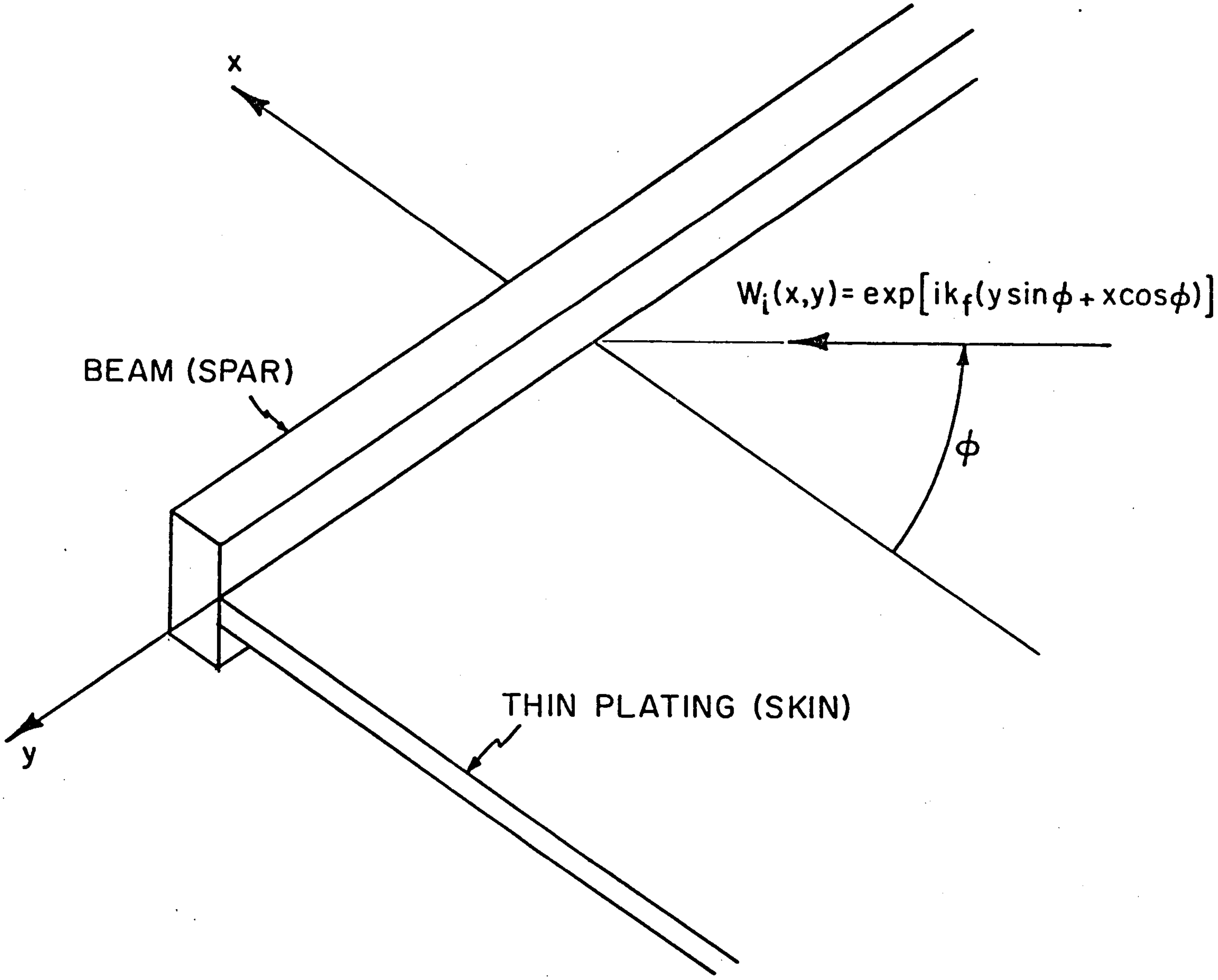

Fig. III.7 - Mathematical model of skin-spar interaction.

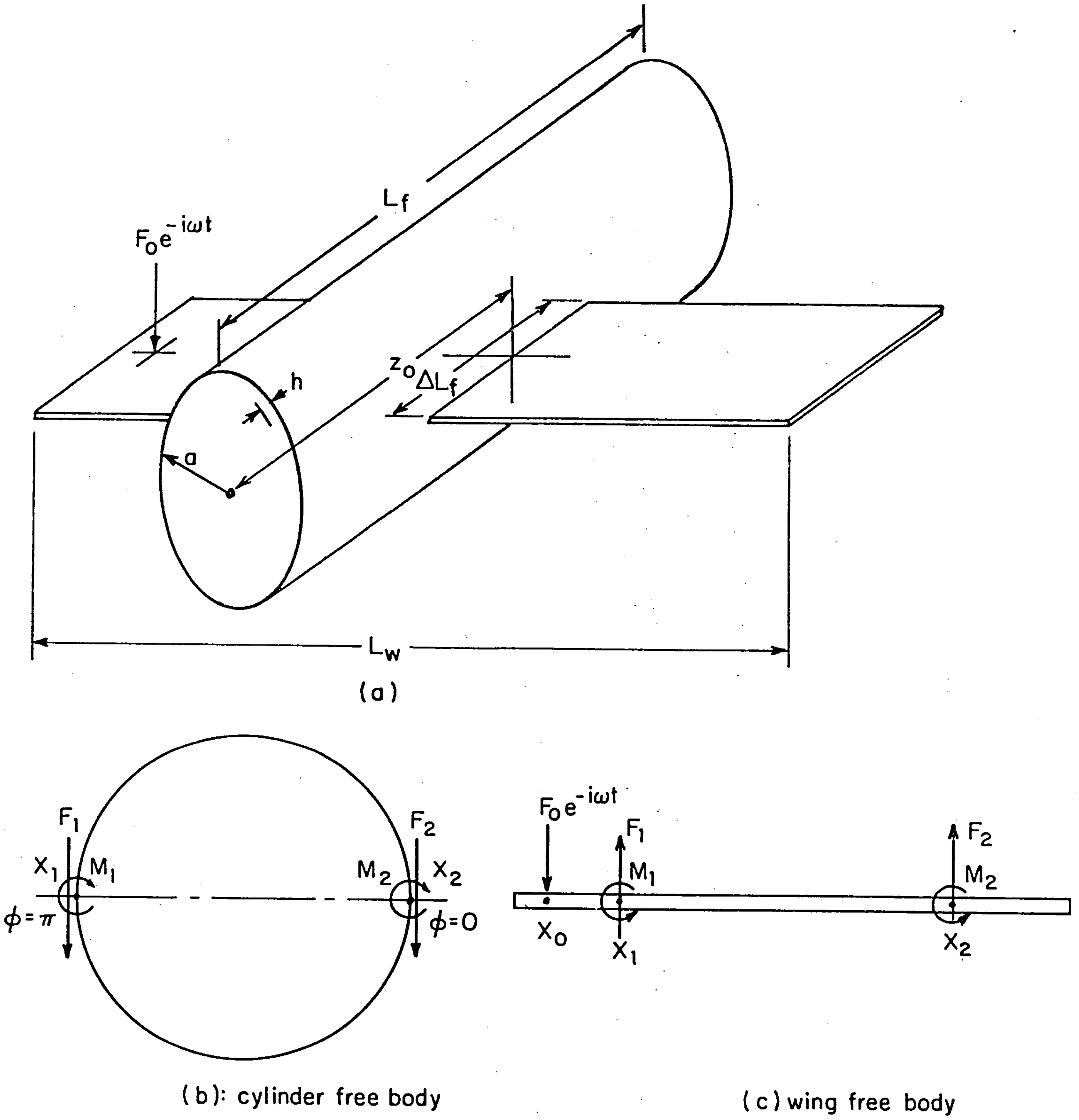

(a)

(b): cylinder free body

(c) wing free body

Fig. III.8a,b,c - Wing-fuselage structural interaction model.

IV. ACOUSTIC MODELS FOR CABIN INTERIOR

A. The Sound Field in a Fuselage Modelled as a Cylindrical Shell Terminated by Bulkheads

1. Introduction

The sound field in an aircraft fuselage, modelled as a cylindrical shell vibrating in response to structureborne noise incident along its wings, is formulated for two types of acoustical treatment. In both cases the cylindrical shell is assumed to be simply supported and terminated by bulkheads, the wings being located in the horizontal plane of symmetry. Both analyses assume that the internal source impedance of the shell modes is so large compared to the impedance of the corresponding room modes, that they (the shell modes) act effectively as constant-velocity sound sources. Under these circumstances, pressure peaks are associated with antiresonance of the air volume, as well of course as with shell resonances.

First, in Section B the sound field inside a cylindrical shell with zero surface absorption is calculated as the sum of two pressure components, one describing the contribution of the cylindrical part of the boundary, and the other that due to the presence of the two end bulkheads. In Section C.1 this solution is generalized in approximate form to account for small surface absorption. In the theory each of the pressure components contains parameters through which bulkhead and radial absorption may be independently controlled. The result derived here, however, takes into account only the latter effect. Inclusion of the former axial effect would require a parallel though somewhat simpler analysis which would complicate final expressions needlessly. In Section C.2 absorption parameters used in B.1 are related to fuselage reverberation time. Finally, Section D is a discussion of the theoretical modal density for both shell structural response and internal acoustic field.

B. The Sound Field in a Vibrating Cylindrical Shell with no Sound Absorption

1. Formulation of the Problem

The radial shell response is in the form of a double Fourier series,

$$w(\phi,z) = \exp(-i\omega t) \sum_{m,n} W_{mn} \sin n\phi \sin \frac{m\pi z}{L} \qquad \text{(IV-1)}$$

Here z is measured from the one shell extremity and the circumferential angle ϕ is from the plane containing the wings. In the more general case where the wings are not restricted to lie in a plane of symmetry, Eq. IV-1 would have to be supplemented with a $\cos n\phi$ series.

The sound pressure satisfies the steady-state wave equation in cylindrical coordinates

$$(\nabla^2+k^2)p = 0 \qquad \text{(IV-2)}$$

and the boundary conditions

$$\begin{aligned} \frac{\partial p}{\partial r} &= -\rho\ddot{w}(\phi,z), \qquad r = a \\ \frac{\partial p}{\partial z} &= 0 \qquad , \qquad z = 0,L \end{aligned} \qquad \text{(IV-3)}$$

A solution satisfying the former boundary condition is readily constructed, by inspection, but being matched to Eq. IV-1, it necessarily displays nodal planes coinciding with the bulkheads. This solution taken by itself is incompatible with the latter boundary condition in Eq. IV-3. We shall therefore construct the pressure field by combining two pressure components.

$$p = p_1+p_2 \qquad \text{(IV-4)}$$

satisfying respectively the boundary conditions

$$\left.\begin{aligned} \frac{\partial p_1}{\partial r} &= -\rho\ddot{w}(\phi,z) \\ \frac{\partial p_2}{\partial r} &= 0 \end{aligned}\right\} \quad r = a \qquad \text{(IV-5)}$$

and

$$\frac{\partial p_2}{\partial z} = -\frac{\partial p_1}{\partial z} \quad , \quad z = 0,L \qquad \text{(IV-6)}$$

This procedure can, if desired, be modified to account for a non-zero specified bulkhead motion, viz., $\Sigma\, u_n(r)\sin n\phi$.

2. Pressure Field Radiated by the Vibrating Shell

Eq. III-1 admits solutions in the form of Bessel functions of the first and second kind. However, the latter display a singularity on the axis r=0. Consequently, in the absence of significant absorption, only functions of the first kind are required. Taking w positive outward, it can be verified that the solution which satisfies Eq. IV-5 is of the form

$$p_1(r,\phi,z) = -\rho \sum_{m,n} \ddot{w}_{mn} \frac{J_n(k_m r)}{k_m J_n'(k_m a)} \sin n\phi \sin \frac{m\pi z}{L} \qquad \text{(IV-7)}$$

where the radial wavenumber is

$$k_m = [k^2 - (m\pi/L)^2]^{\frac{1}{2}} \qquad \text{(IV-8)}$$

This pressure component describes the sound field in an infinitely periodic shell. If the shell is provided with a sound absorptive core, the Bessel functions in Eq. IV-7 are replaced by Hankel functions. Both solutions predict vanishing pressures in the planes z=0 and L. Some analyses even though intended for finite shells, erroneously omit the pressure component p_2 required to account for the bulkheads, whether the space is anechoic or not.[21]

The axial pressure gradient in the plane of the bulkheads is

$$\begin{aligned} \frac{\partial p_1}{\partial z} &= -\rho \sum_m \frac{m\pi}{L} \sum_n W_{mn} \frac{J_n(k_m r)}{k_m J_n'(k_m a)} \sin n\phi \quad , \quad z=0 \\ &= -\rho \sum_m \frac{m\pi}{L} (-1)^m \sum_n \ddot{W}_{mn} \frac{J_n(k_m r)}{k_m J_n'(k_m a)} \sin n\phi \quad , \quad z=L \end{aligned} \qquad \text{(IV-9)}$$

The pressure component in Eq. IV-7 displays resonances at frequencies where the product $k_m a$ equals a root of the Bessel functions. As explained in the introduction, the pressure peaks generated by a high-internal impedance source are associated with antiresonances at the zeros $\gamma_{ns} a$ of the Bessel function derivatives[22]

$$f^a_{mns} = \frac{c}{2\pi} \left(\gamma_{ns}^2 + \frac{m^2 \pi^2}{L^2} \right)^{\frac{1}{2}} \quad , \quad J_n'(\gamma_{ns} a) = 0 \qquad \text{(IV-10)}$$

There is therefore a triple infinity of room resonances and antiresonances. For $k_m = 0$,

$$f^a_{om} = \frac{cm}{2L} \tag{IV-11}$$

is an antiresonance for n=0. This wave harmonic is excited only if the wing plane does not contain the cylindrical axis.

It is convenient to distinguish between odd and even axial modes by selecting a new origin of coordinates in the midplane, at z = L/2. The new axial coordinate is

$$z' = z - \tfrac{1}{2}L$$

The pressure in Eq. IV-7 now becomes

$$p_1(r,\phi, z') = -\rho \sum_{m,n} \frac{\ddot{W}_{mn} J_n(k_m r)}{k_m J'_n(k_m a)} \sin n\phi \begin{cases} (-1)^{(m-1)/2} \cos(m\pi z'/L), & m = 1,3,\ldots \\ (-1)^{m/2} \sin(m\pi z'/L), & m = 2,4,\ldots \end{cases} \tag{IV-12}$$

3. Pressure Field Generated by the Bulkheads

We now construct the pressure component which satisfies Eq. IV-6, where $\partial p_1/\partial z$ is given by Eq. IV-9. Noting that odd values of m in Eq. IV-7 correspond to the even modes, i.e., modes symmetrical about the midplane, while even values of m correspond to modes which are antisymmetric about this midplane, the pressure component we are seeking is of the form

$$p_2(r,\phi,z') = \sum_{n,s} J_n(\gamma_{ns} r) \sin n\phi \left[\sum_{m=1,3} P_{mns} \cos k_{ns} z' + \sum_{m=2,4} P_{mns} \sin k_{ns} z'\right] \tag{IV-13}$$

where

$$k_{ns} = (k^2 - \gamma^2_{ns})^{\frac{1}{2}} \tag{IV-14}$$

and where, as in Eq. IV-11, $\gamma_{ns} a$ is a root of J'_n.

Consequently, the introduction of p_2 does not alter the boundary condition satisfied at r=a by p_1. Differentiating Eq. IV-9 with respect to z', one can satisfy the boundary condition in Eq. IV-6 by expressing each m,n term in Eq. IV-9 to a Fourier-Bessel series:

$$\frac{\rho \ddot{W}_{mn} m\pi}{k_m L} \; \frac{J_n(k_m r)}{J_n'(k_m a)} = \sum_s k_{ns} P_{mns} J_n(\gamma_{ns} r) \begin{cases} \sin \dfrac{k_{ns} L}{2} \; , & m = 1,3,\ldots \\ \cos \dfrac{k_{ns} L}{2} \; , & m = 2,4,\ldots \end{cases} \tag{IV-15}$$

Multiplying both sides of this equation by $J_n(\gamma_{ns} r)$ and integrating allows one to solve for the coefficients of the Fourier-Bessel series:[23,24]

$$P_{mns} = \frac{2\rho m \pi \gamma_{ns}^2 \ddot{W}_{mn}}{k_{ns} k_m L(\gamma_{ns}^2 a^2 - n^2)} \; \frac{I_{mns}}{J_n'(k_m a) J_n^2(\gamma_{ns} a)} \begin{cases} [\sin(k_{ns} L/2)]^{-1}, & m=1,3,\ldots \\ [\cos(k_{ns} L/w)]^{-1}, & m=2,4,\ldots \end{cases} \tag{IV-16}$$

where the integral I_{mns} is[25,26,27]

$$\begin{aligned} I_{mns} &\equiv \int_0^a J_n(k_m r) J_n(\gamma_{ns} r)\, r\,dr \\ &= \frac{k_m a}{\gamma_{ns}^2 - k_m^2} \; J_n(\gamma_{ns} a) J_n'(k_m a) \end{aligned} \tag{IV-17}$$

Combining Eqs. IV-13, 16, and 17, this yields an explicit expression for the bulkhead-reflected pressure:

$$p_2(r,\phi,z') = \frac{2\rho\pi a}{L} \sum_{m,n,s} \frac{\ddot{W}_{mn} m \gamma_{ns}^2 \sin n\phi \; J_n(\gamma_{ns} r)}{k_{ns}(\gamma_{ns}^2 - k_m^2)(\gamma_{ns}^2 a^2 - n^2) J_n(\gamma_{ns} a)} \begin{cases} \dfrac{\cos k_{ns} z'}{\sin(k_{ns} L/2)} \; , & m = 1,3,\ldots \\ \dfrac{\sin k_{ns} z'}{\cos(k_{ns} L/2)} \; , & m = 2,4,\ldots \end{cases} \tag{IV-18}$$

This does not introduce any additional resonances or antiresonances.

The resultant pressure is finally obtained by adding Eqs. IV-12 and 18 as indicated in Eq. IV-4.

C. Sound Field in a Vibrating Cylindrical Shell with Small Sound Absorption

1. Generalization of Section B Theory

We define the cylinder internal pressure p^* and associated Green's function G^* as the absorptive counterparts of those in Section B (there defined without asterisk though G is not used explicitly). With non-zero surface admittance K (Ref. 1, Eq. 24) their boundary-value problems are, respectively,

$$\nabla^2 p^* + (ka)^2 p^* = 0 \qquad \text{(IV-19a)}$$

$$\frac{\partial p^*}{\partial n_o} + iKp^* = -\rho \ddot{w} a \qquad \text{on } n_o = r_o = 1 \qquad \text{(IV-19b)}$$

$$\frac{\partial p^*}{\partial n_o} = 0 \qquad \text{on } n_o = z_o = \pm L/a \qquad \text{(IV-19c)}$$

$$\nabla^2 G^* + (ka)^2 G^* = \delta(\bar{x} - \bar{x}_o) \qquad \text{(IV-20a)}$$

$$\frac{\partial G^*}{\partial n_o} + iKG^* = 0 \qquad \text{on } n_o = r_o = 1 \qquad \text{(IV-20b)}$$

so that

$$p^* = \frac{1}{4\pi} \int_S dSG^* \quad \frac{\partial p^*}{\partial r_o} + iKp^* \quad = -\frac{\rho}{4\pi} \int_S dSG^* \ddot{w} \qquad \text{(IV-21)}$$

In terms of room modes appropriate to the cylindrical geometry the solution for G^* may be constructed for small values of K:

$$G^* = 2a \sum_{nms} \frac{\gamma_{ns}^{*2} J(\gamma_{ns}^* r) J_n(\gamma_{ns}^* r_o) \sin n\phi \sin n\phi_o \sin(m\pi z/L) \sin(m\pi z_o/L)}{J_n^2(\gamma_{ns}^*) [\gamma_{ns}^{*2} - n^2] \left[(ka)^2 - \left(\frac{m\pi a}{L} \right)^2 - \gamma_{ns}^{*2} \right]} \qquad \text{(IV-22)}$$

where r, r_o are normalized by the radius a and γ_{ns}^* are the eigenvalues of the radially absorptive boundary condition, a modal form of which (Eq. IV-25 below) is given shortly, For small K γ_{ns}^* may be assumed equal to the real zero γ_{ns} plus a small complex part; viz.,

$$\gamma_{ns}^{*} \simeq \gamma_{ns}+i\varepsilon \qquad \text{(IV-23)}$$

For $\varepsilon=0$ G^{*} as given by Eq. IV-22 collapses to the room mode form of G, the Green's function for the nonabsorptive case which contains an infinite antiresonance whenever the denominator vanishes, i.e., whenever $(ka)^2-(m\pi a/L)^2-\gamma_{ns}^2 = 0$, or at frequencies given by,

$$f = \frac{2\pi c/a}{\sqrt{\left(\frac{m\pi a}{L}\right)^2+\gamma_{ns}^2}}$$

With absorption, however, the corresponding value of this quantity is always finite, since then

$$(ka)^2 - \left(\frac{m\pi a}{L}\right)^2 -\gamma_{ns}^{*2} \simeq -2i\varepsilon\gamma_{ns} \qquad \text{(IV-24)}$$

We now calculate ε in terms of K. The $r_o = 1$ homogeneous boundary condition on G^{*} (Eq. IV-20b) implies that

$$\lim_{r_o\to 1} \gamma_{ns}^{*}J_n'(\gamma_{ns}^{*}r_o)+iKJ_n(\gamma_{ns}^{*}r_o) = 0 \qquad \text{(IV-25)}$$

Since $J_n'(\gamma_{ns}^{*}) \simeq i\varepsilon J_n''(\gamma_{ns})$, and $J_n(\gamma_{ns}^{*}) = J_n(\gamma_{ns})+0(\varepsilon^2)$ it follows that

$$\varepsilon = \frac{-KJ_n(\gamma_{ns})}{\gamma_{ns}J_n''(\gamma_{ns})}$$

so that the right side of Eq. IV-24 becomes

$$\frac{2iKJ_n(\gamma_{ns})}{J_n''(\gamma_{ns})}$$

The p_1^{*} component of pressure with nonzero absorption may now be obtained in terms of a triple sum of room modes by substitution of G^{*} with the above result for ε:

$$p_1^{*} = 2\rho a \sum_{mns} \frac{J_n(\gamma_{ns}^{*}r)\gamma_{ns}^{*2} \sin n\phi \sin m\pi z/L\, \ddot{W}_{mn}}{J_n(\gamma_{ns}^{*})(\gamma_{ns}^{*2}-n^2)\left[(ka)^2-\left(\frac{m\pi}{L/a}\right)^2 - \gamma_{ns}^{*2}\right]} \qquad \text{(IV-27)}$$

or

$$p_1^* = -\rho a \sum_{mn} \sin m\pi z/L \; \sin n\phi \; \tilde{\psi}_{mn}(r)\ddot{W}_{mn} \tag{IV-28a}$$

$$\tilde{\psi}_{mn}(r) = 2 \sum_s \frac{J_{ns}(\gamma_{ns}^* r)\gamma_{ns}^{*2}}{J_n(\gamma_{ns}^*)(\gamma_{ns}^{*2}-n^2)\left[\gamma_{ns}^{*2} + \left(\frac{m\pi a}{L}\right)^2 - (ka)^2\right]} \tag{IV-28b}$$

In Section B, p_1 appears in a different form, however. There the more economical double sum solution in Eq. III-7 was the end result of an implicit construction of the Green's function to satisfy the radial boundary condition with no absorption. Letting $\varepsilon=0$ in Eq. IV-27, it follows therefore that the following identity must hold for any m, n, ka combination

$$2 \sum_s \frac{J_n(\gamma_{ns} r)\gamma_{ns}^2}{J_n(\gamma_{ns})(\gamma_{ns}^2-n^2)\left[\gamma_{ns}^2 + \left(\frac{m\pi a}{L}\right)^2 - (ka)^2\right]}$$

$$= \frac{J_n\left(\sqrt{(ka)^2-(m\pi a/L)^2}\;\; r\right)}{\sqrt{(ka)^2-(m\pi a/L)^2}\; J_n'\left(\sqrt{(ka)^2-(m\pi a/L)^2}\right)} \quad . \tag{IV-29}$$

One may now approximate the right side of Eq. IV-28b for $\varepsilon << 1$. The result is the term on the left side of Eq. IV-29 plus the following correction term

$$+2i\varepsilon r(1-r) \sum_s \frac{\gamma_{ns}}{\gamma_{ns}^2+(m\pi a/L)^2-(ka)^2} \tag{IV-30}$$

Away from the antiresonances then, where no single term in the s sum dominates, the eigenfunction for the double-sum solution from Section B may still be used as the right side of Eq. IV-29 after neglecting its $0(\varepsilon)$ correction given in Eq. IV-30.

At the antiresonances, where the $s=\tilde{s}$ term for which Eq. IV-24 is satisfied dominates the sum, we find that the latter may then be approximated to yield that

$$\tilde{\psi}_{mn}(r) \cong \frac{-i}{\varepsilon} \; \frac{J_n(\gamma_{ns} r)\gamma_{ns}}{J_n(\gamma_{ns})(\gamma_{ns}^2-n^2)} \tag{IV-31}$$

which upon substitution of ε in terms of K (Eq. IV-26), and use of Bessel's equation $(J_n''/(n^2-\gamma_{ns}^2) = J_n/\gamma_{ns}^2)$, gives that

$$\tilde{\psi}_{mn}(r) = \frac{-i}{K} \frac{J_n(\gamma_{ns}r)}{J_n(\gamma_{ns})} \tag{IV-32}$$

In summary then, the absorptive double-sum model for p_1^* could be kept as given in Section B away from the antiresonances; and near them, where the term on the right side of Eq. IV-29 becomes infinite, the latter can be replaced by the expression on the right side of Eq. IV-32, i.e., a finite quantity. A practical payoff of the approximations is that the absorptive case continues then to have Bessel functions of real arguments, thus allowing use of well-known efficient numerical techniques for their evaluation.

So far we have dealt only with the p_1^* component for pressure, which appeared in Section B in terms of a constructed Green's function and which we could not therefore immediately generalize to account for small radial absorption. The analysis first had to invoke the room-mode formulation, for which the generalization to include absorption is in principle always simple. The p_2 solution given in Eq. IV-18, however, appears already cast in room-mode form. The corresponding p_2^* solution is thus simply given by that same expression with γ_{ns} replaced by γ_{ns}^*. Furthermore, for convenience of computation and consistency with the above analysis for p_1^*, the imaginary part of γ_{ns}^* may be dropped from all Bessel function arguments and kept only in the algebraic denominator terms for modes containing an antiresonance.

It is interesting to note that the p_2 solution in Eq. IV-18 exhibits a larger number of antiresonances than does p_1. It contains all the antiresonances apparent in p_1, as indicated by the $\gamma_{ns}^2-k_m^2$ term in the denominator in Eq. IV-18 (where wavenumbers do not appear normalized by a as they do here), but also it contains others corresponding to zeros of k_{ns} in Eq. IV-14. However, these new antiresonances may be interpreted as given by the same criterion which defines those of p_1, so long as the latter may be allowed to include the m=0 possibility. The reason for omission of m=0 in earlier discussions is, of course, that m=0 represents a degenerate mode for p_1, which is constructed in terms of sin $m\pi z/L$ eigenfunctions.

2. Estimate of Reverberation Time

It may be useful to relate the notation used above to the symbols found in standard texts such as Morse[28] and Pierce,[29] and to express the attenuation term in terms of the reverberation time. While Eq. IV-23 is associated only with the radial wavenumber, being effectively a large-L or small-m approximation, room acoustics theory embodies the resultant wavenumber. For ease of relating variables to those of Morse and Pierce, we revert to the dimensional forms of γ_{ns}, etc., as used in Section IV.B.

In cylindrical coordinates, the complex wavenumber is

$$\gamma_N^{*2} = \left(\gamma_{ns}^2 + \frac{m^2\pi^2}{L^2}\right)(1+i\eta_N). \qquad \text{(IV-33)}$$

This related to the imaginary term in Eq. IV-23 as

$$\eta_N \cong -2\frac{\varepsilon}{\gamma_N} \quad , \quad \eta_N << 1 \qquad \text{(IV-34)}$$

In Morse's notation,[28]

$$\gamma_N = \omega_N/\varepsilon \quad , \quad \eta_N = 2\frac{k_N}{\omega_N}$$

In Pierce's notation,[29]

$$\gamma_N = k(n)$$

$$\eta_N = \frac{kB_{nn}}{k^2(n)}$$

The imaginary component of Eq. IV-33 is related to the characteristic decay time τ_n of mode N as

$$\text{Im } \gamma_N^{*2} = \frac{k}{c\tau_N}$$

Since τ_N equals the reverberation time T_N divided by 6 ℓn 10 = 13.8, this can be written as

$$\text{Im } \gamma^{*2} = \frac{7.3\text{x}10^{-4}f}{T_n} \ m^{-2}$$

where f is in Hz and T_n in sec.

The attenuation constant in Eq. IV-3 can be computed from the attenuation A_z over the bulkheads and the attenuation A_r over the cylindrical boundary (Ref. 28, p. 409):

$$\varepsilon = -\frac{1}{16V}\left[2A_z + \frac{A_r}{1-(n/\gamma_{ns}a)^2}\right] \qquad \text{(IV-35)}$$

where V is the volume of the cylinder.

D. Modal Density and Resonance Bandwidth of the Structural Response and Sound Field

Peak pressures are observed at the natural frequencies of the shell and at the eigenfrequencies of the room, Eq. IV-10. It is of interest to determine the respective contributions of these two families of resonances for the parameters of the laboratory test model.

1. Structural Resonance Spacing of Cylindrical Shell

The shell acts effectively as a membrane below its breathing mode natural frequency $f_o = 2\pi a/c_p$, where c_p is the plate velocity in aluminum. For membrane modes, stiffeners are not anticipated to raise the natural frequencies significantly, i.e., to decrease the modal density. In the frequency range above the breathing mode resonance, where the shell responds predominantly in flexure, stiffeners are anticipated not only to raise the natural frequencies, but to cause the modal density to decrease with increasing frequency, in contrast to the modal density of the unstiffened shell which is frequency independent at high frequencies. In the low frequency range, below the ring resonance $f_r = f_o(1-\nu^2)$ (= 3.2 kHz for the 0.50 m (20 in.) shell), we shall therefore approximate the modal densities of the stiffened shell by those of the unstiffened shell.

$$\frac{dN}{df} \cong \frac{2.5}{\pi}\,\frac{f^{1/2}}{f_r^{3/4}}\,\frac{L}{h} \quad , \quad \text{Hz}^{-1} \quad , \quad f \le 0.48\, f_r \qquad \text{(IV-36)}$$

$$\cong \frac{3.6}{\pi}\,\frac{L}{h}\,\frac{f}{f_r^2} \quad , \quad 0.48 < \frac{f}{f_r} \le 0.83$$

For the 0.5 m (20 in.) shell, this becomes

$$\frac{dN}{df} = 1.3 \times 10^{-2} f^{1/2} \quad , \quad f \le 1.5\ \text{kHz}$$

$$= 3.4 \times 10^{-4} f \qquad , \qquad 1.5 \text{ kHz} < f < 1.7 \text{ kHz}$$

The spacing $(dN/df)^{-1}$ of the resonance peaks is shown in the first column of Table IV-1.

2. Room Mode Antiresonance Spacing

The modal density of the characteristic frequencies of the modes of a cylindrical room are given by (Ref. 28, p. 400)

$$\frac{dN}{df} = \frac{1}{c}\left[\left(\frac{2\pi af}{c}\right)^2 L + \frac{\pi^2 af}{c}(a+L) + \frac{\pi a+L}{2}\right] \quad , \quad \text{Hz}^{-1} \qquad \text{(IV-37)}$$

For the dimensions of the 0.50 m (20 in.) shell, this yields

$$\frac{dN}{df} \cong 7.6 \times 10^{-8} f^2 + 3.1 \times 10^{-5} f + 0(10^{-3}) \quad , \quad \text{Hz}^{-1} \qquad \text{(IV-38)}$$

The corresponding frequency spacing is tabulated in the second column of Table IV-1.

3. Bandwidth of Pressure Peaks for Structural Response and for Acoustic Field

The bandwidth between the -3 dB points of a peak is ηf. Even selecting a conservatively small structural loss factor of $\eta = 0.01$, the bandwidth is seen to exceed the average resonance spacing of the shell modes (third column of Table IV-1).

The loss factor associated with a room mode is computed from Eq. IV-35 with $\gamma_N = k$. We shall conservatively assume that $(n/\gamma_{ns}a)^2 << 1$. Assuming that all interior boundaries are covered with a blanket whose absorption coefficient is as indicated in the fourth column of Table IV-1, one computes room bandwidths which, once again, are wider than the average resonance, or antiresonance, spacing. Since room modes tend to cluster, there may of course exist noticeable pressure peaks in frequency ranges sparsely populated by characteristic frequencies, but we do not expect marked peaks at the frequency spacings calculated above. It should, of course, be recalled that these results are semi-quantitative in that we apply an asymptotic small-boundary admittance theory.

Finally, since boundary absorption limits pressure buildup at these antiresonance frequencies, the modelling of the shell as a large-internal impedance sound source seems justified. For this same reason it is anticipated that as long as the model shell boundaries are provided with an acoustic blanket, while the shell is devoid of a damping coating, marked pressure peaks will be associated with structural resonances rather than with the characteristic frequencies of the room modes.

TABLE IV-1

Resonance Characteristics of 0.50 m (20 in) Model Shell

(All Units in Hz)

f	Average Resonance Spacing		-3 dB Resonance Bandwidth	
	Shell Modes	Room Modes	Shell ($\eta=10^{-2}$)	Room
500	3.4	29	5	26 (α=0.4)
1000	2.4	9.1	10	46 (α=0.7)
2000	1.5	2.7	20	46 (α=0.7)

V. CALCULATED RESULTS FOR INTERIOR NOISE

A. Introduction

In this chapter we present results for the interior acoustic field calculated using the analytical models of the source, structure, and sound field developed in the preceding sections. The calculations have been performed for parameters representative of two physical structures. The first is a full scale aircraft excited by the propeller wake acting on the skin of the wing. The second structure is a laboratory model consisting of a shell coupled to a uniform beam. Excitation of this model is a shaker applied near the outer end of the beam.

Because our goal in this study has been to examine a variety of parameters relevant to the structureborne noise problem, various models (i.e., assumptions) have been used to obtain the results presented in this section.

B. Full Scale Aircraft

The dimensions used for the estimate of the interior noise field of a small aircraft in response to a propeller wake excitation of the wing are given in Table V-1. As indicated the chord of the wing is taken to be 1/4 the length of the shell, the wing being centered along the shell. The principal assumptions invoked to obtain the interior noise estimate are given as follows:

1. The propeller wake-induced pressures propagate to the fuselage along the skin of the wing.
2. The structural impedance presented to the wing skin by the fuselage is large.
3. The effects of coupling between the wing and fuselage on the side away from the excitation are negligible.
4. The fuselage can be modelled as a uniform shell.
5. The interior pressure field is consistent with pressure-release terminations (i.e., the p_1 component discussed in Chapter IV).

The first assumption defines the structureborne path being considered, and relates to the fact that the skins of the wing and fuselage are contiguous. The implication of the second assumption is that the wing reaction loads can be calculated assuming rigid constraints at the fuselage interface. The reaction loads thus calculated can then be applied directly to the shell. The third assumption follows from the second in that the fuselage blocks propagation along the wing and any back reaction of the shell on the low impedance skin is negligible. The last two assumptions are invoked for convenience in computation. The presence of internal fluid is included in this model in evaluating the shell response.

The pressure at the propeller blade passing frequency (283 Hz) and normalized to the maximum pressure on the wing in the propeller wake is shown as a function of axial distance from the midspan on Fig. V.1. Circumferential variations of the pressure have been averaged over angles of 30°, 60°, and 90° from the location of the excitation. The parameter of the curves presented is the radial distance from the center of the shell. It is noted that the predicted level of the interior pressure is comparable to the maximum pressure applied to the wing by the propeller wake (i.e., 0 dB). This result differs from the relatively low radiation from discontinuities along the wing predicted earlier (Section III.A.5) primarily because of the high radiation efficiency of the membrane-like modes in the (cylindrical) shell. Fortunately as discussed in Section III.A, this structural path can be easily interrupted by ribs or other structural discontinuities. Another feature of the results in Fig. V.1 is the smooth variation of the average pressure with both radial and axial locations near the excitation.

C. Laboratory Model

1. Introduction

The schematic in Fig. V.2 shows the test model at NASA Langley Research Center, the dimensions being given in Table V-I. The physical model consists of a thin cylindrical shell reinforced by five stiffeners in each direction (i.e., frames and stringers). The box-beam representing the wing passes through the shell just above the horizontal and is driven by a shaker near one end. The beam and shell materials are, respectively, magnesium and aluminum, both assumed in the theory to have a loss factor of .01. The apparatus is suspended by a pair of shock chords, each attached to the shell at the uppermost point of the flat end cap.

As described in Section III the analytical model of the coupled beam and shell is a somewhat simplified representation of the physical model. In particular neither the effects of the stiffeners nor the loading of the internal fluid are included in this model. Both these effects are examined using another model and discussed further along in this section.

2. Detailed Results for the Coupled Beam and Shell Model

As previously implied, the calculation of the acoustic field by the theories of Chapter III.B and IV.A is really a two-step process. First the forces and moments at the two wing-fuselage intersection locations are solved for from the combined admittance system (Eq. III-50). Then, the numerical values for the reactions so computed (in terms of the drive amplitude F_o) become drives for the acoustic model of IV.A. As discussed in Chapter IV, in the acoustic model these four reactions appear distributed over the root chord.

In addition to the final acoustic predictions for the laboratory shell-beam model, in fact, in order to best interpret them, some intermediate structural results are also presented here. Regarding these, we should point out that for the unframed shell model rotational admittances remained consistently high over the frequency range investigated (600-2000 Hz), with the result that the two moment reactions are always found to be insignificant relative to the two shear forces (typically 20-30 dB down). Furthermore, since their influence coefficients in the sound field are found to be of magnitude comparable to those of the shear loads, their acoustic contribution is also negligible. We therefore omit from discussion the two moment reactions and their part in the coupled system of Eq. III-50 (bottom two rows and rightmost two columns).

Figure V.3 shows, vs. frequency, the self admittances c_{11}, Kc^*_{11} for the beam and shell, respectively. Relative maxima occur for c_{11} at 800, 1200, and 1700 Hz, corresponding to natural frequencies of the free-free beam. The fundamental resonance frequency of the beam is 89 Hz. The greater modal density of the shell within this frequency range is evident from both the less patterned nature of Kc^*_{11} and the milder oscillations for the same loss factor. Of particular interest is the fact that the beam and shell admittances are on average of comparable magnitude making for efficient coupling of structureborne noise between the two structures.

Figure V.4 similarly shows the two shear reactions F_1, F_2 (normalized by F_o) as a function of frequency. Here the efficient coupling mentioned earlier is manifested in the force ratios hovering about unity or 0 dB. Also, the fact that F_1 and F_2 are of comparable magnitude results from both this close coupling and the assumed low loss factor.

The "structural-acoustical influence function" of the shell, that is the interior acoustic pressure level per unit tangential force on the shell is plotted in Fib. V.5 for two field locations. The predicted oscillations with frequency are great, in excess of 40 dB over the band shown, and since the modal density of the acoustical space and the shell exceeds the spacing between computed points, they are not connected. Pressure peaks occur at frequencies corresponding to resonances of the structure, and, with fluid loading on the shell neglected in calculating the shell response, at antiresonance frequencies of the interior acoustic space. This latter source of peakiness requires further discussion.

The interior acoustic space being closed exhibits an infinite set of resonance frequencies associated with its "room" modes. Between these frequencies exist antiresonance frequencies and ignoring acoustic absorption a room mode driven at antiresonance yields an infinite impedance. Under this circumstance the modal impedance of the acoustic space exceeds that of the shell. If the interaction problem is solved rigorously, that is if the acoustic impedance is included in the calculation of the shell response then the antiresonant mode is not excited owing to its infinite impedance. However if neglected, the contribution of such a mode to the shell response is finite and the infinite acoustic impedance yields the artifact of an infinite acoustic pressure level at precisely these antiresonance frequencies. Nevertheless, interestingly enough, these predicted peaks do reflect at least qualitatively a real phenomenon, one that results from the rigorously solved interaction problem in the absence of appreciable absorption and structural damping.

As the excitation frequency sweeps through each of these modal acoustic antiresonance frequencies the acoustic impedance rises in above and then drops below the corresponding modal shell impedance and in so doing changes from inertial to stiffness-like or vice versa. Thus not precisely at, but in the vicinity of, the antiresonance frequency, the reactive components of the acoustic and shell impedances will cancel and a peak pressure will result due to what may accurately be called a coupled or system resonance. And in the absence of energy dissipation these peaks will be infinite.

Therefore the only way to reduce this second set of peaks to realistic values is to incorporate realistic absorption or damping into the model. Although, in this report (Chapter IV) and elsewhere, asymptotic approaches have been developed for this purpose, namely small absorption or black body radiation[31] models, more rigorous and computationally efficient solutions are required, at a minimum for confirmation of these models.

An example of the effect of fluid loading on the internal pressure field in the absence of absorption is given in Fig. V.6. These results are calculated for the unframed laboratory shell excited by a point circumferential load at midspan, the pressure being evaluated at the same axial location as the load and 2 inches (.05 m) in from the surface. In the frequency range indicated there are 21 antiresonance frequencies of the internal fluid. However, with a structural loss factor of $\eta = 0.01$ the results for the fully coupled problem (i.e., including fluid loading) are found to vary smoothly near the antiresonance frequencies. The results of the calculation performed without including fluid loading are however strongly influenced by the proximity of the frequency of interest to an antiresonance frequency. Consequently these results are shown as points. Differences of as much as 20 dB are found between the results of the two calculations shown on Fig. V.6.

With the above background comments Fig. V.7 is presented comparing the calculated acoustic pressure normalized to the input force on the beam with measurements. Specifically Fig. V.7 is a plot of acoustic pressure p_{oe} normalized by F_o/ft^2 as predicted by the nonabsorptive model of Section IV.A. The measurement curves corresponds to the nominally "beam-horizontal" position (as shown in Fig. IV.1c; beam vertical refers to the latter rotated by 90°). One curve is for the beam attached to the shell ring frames, and the other for the beam attached to longitudinal stringers. The axial position z is the halfway point between the cylinder ends, and the radial position is r = 8 in. or 2 in. in from the shell inner surface. For this r,z combination two circumferential angular positions are shown in the predicted results: 45° from the horizontal plane measured from the drive-side of the beam, and 90°. Measurements are for these same values of r,z, and for $\phi = 90°$. As expected the omission of acoustic absorption in these calculations produces levels that are high at specific frequencies as well as on-average. Thus in spite of the complexity of the mathematical model which for example includes finite length shell and acoustic space effects, and the beam-shell interactions, the salient features of the measured data are not predicted well. (The effects of the omission of stiffening frames is discussed in Section V.C.5.) The lessons to be learned from this exercise have been summarized in Section 6.

Although broad band analyses are of limited value given the tonal nature of the problem at hand they are generally insightful and in this context a simple power flow view of the measurements is presented in the following section section.

3. Asymptotic model and results

Detailed (deterministic) mathematical models are necessitated by the fact that the major problem associated with prop-fan induced cabin noise is tonal in nature. Nevertheless, even for tonal problems broadband or statistical analyses are often useful in providing additional guidance and insight. For example let us consider the implications of balance of power for the set of shell experiments being investigated.

Power is introduced into the system via the shaker at the termination of the beam (wing). The amount of power is given by

$$\pi_{in} = F^2 \mathrm{Re}(Y) \qquad \text{(V-1)}$$

where F is the rms force level and Re(Y) the real component of the drive point admittance of the beam. If we ignore finite length effects on Y, in other words if we ignore the effects of reflections from the shell-beam interface as well as the far end of the beam, then it can be shown that $\mathrm{Re}(Y) = k_f/\omega\mu$ where k_f is the wavenumber of freely propagating flexural waves in the beam and $\omega\mu$ its locally reacting inertial impedance.

Let us suppose that the dominant dissipation mechanism is the absorption of acoustic energy in the "blanket" that is located along the inner surface of the shell. That is, it is assumed that under steady state conditions the power flow is from mechanical power in the beam to acoustic power within the cylindrical space (without appreciable losses) and that this power is then dissipated along the interior of the shell surface by the blanket. This may be expressed as follows

$$\Pi_{in} = \Pi_{out} = I_a S \qquad \text{(V-2)}$$

where I_a is the space averaged acoustic intensity at the shell surface and $S \sim 2\pi aL$ the surface area of the shell. Eq. V-2 may now be used to obtain an upper bound (in view of the above assumptions) estimate of the interior pressure levels. Taking the plane wave admittance for the acoustic space, $I_a = p^2/\rho c$, where p is the space averaged rms pressure. Therefore,

$$|P/F|^2 = (\rho/\rho_b)(k_f/k)(A_bS)^{-1} \qquad \text{(V-3)}$$

or

$$|pa^2/F|^2 = (2\pi^2)^{-1}(\rho/\rho_b)(f_c/f)^{\frac{1}{2}}(a/L)A_s/A_b \qquad \text{(V-4)}$$

where ρ and ρ_b are the mass densities of the acoustic medium (air) and the beam (magnesium) respectively, $k = \omega/c$ is the wavenumber of acoustic waves, A_b and A_s are the cross-sectional areas of the beam and shell, and f_c is the critical frequency for flexural vibrations in the beam (the frequency at which the wavelength of freely propagating flexural waves in the beam matches the acoustic wavelength). For the shell experiments performed in the laboratory, and with the beam "horizontal", f_c = 238 Hz and we get

$$20 \log|P/R| \text{ (re: } 1 \text{ ft}^{-2}) = -14 - 5 \log [f(\text{Hz})] \qquad \text{(V-5)}$$

(Since f_c is proportional to the radius of gyration of the beam, differences between horizontal and vertical positioning of the tested beam are expected to be less than 3 dB.) Eq. 5 is compared in Fig. V.8 to an envelope of experimental data constructed from the six curves corresponding to measurement at ϕ = 0°, 90°, and 180°, for both ring and stringer shell-beam attachment. Also shown is the three point average (ϕ = 45°, 90°, and 135°) of the acoustic field as predicted using the methods of Chapters III.B and IV.A. The favorable comparison between the power balance calculation and the data is gratifying and it is noted that the parametric dependence of the prediction (Eq. V-4) implies that for this particular model the acoustic field, frequency averaged is relatively insensitive to minor structural changes such as beam-shell attachment details or beam orientation.

4. Effect of Structural Damping of the Shell

As present in the wing model discussed in Chapter III, the effect of adding structural damping to the wing is to increase the propagation loss and thereby to decrease the excitation of the fuselage. The effects on interior noise achieved by structurally damping the fuselage however are somewhat less obvious. Shown in Fig. V.9 is the pressure at a point inside the unframed test shell for both small (η = 0.01) and large (η = 1.0) damping. The excitation is a point circumferential load (shear), applied at a half way point between the shell ends. In the case of large damping, the acoustic source can be viewed as being the structural near field of the excitation, and the shell away from the drive point acts as a locally-reacting high-impedance boundary. For low damping, the shell away from the drive point responds as a wavebearing boundary. The results on Fig. V.9 show that comparable peak levels are obtained for both values of damping, indicating that radiation from the structural nearfield of the excitation is important for the unframed shell. This being the case the interior noise level averaged over frequency is not expected to be sensitive to the structural damping in the fuselage. However as indicated on Fig. V.9 a general statement regarding the effect of damping at a specific frequency and location can not be made.

5. Effect of Shell Ring-Frame Stiffeners

Results have been calculated for the test cylinder stiffened by five frames located along the shell at intervals of eight inches (see Fig. V.10). A structural loss factor of 0.01 is assumed. The dimensions of the frames are indicated in Fig. V.10c. Results are calculated every 50 Hz in the middle frequency range from 800 to 1200 Hz. For the purpose of examining the effect of frames on the interior acoustic field, the shell is assumed to be excited by a single localized load on the frame located midway between the simple supports. The resulting symmetry permits the response to be calculated using only the odd numbered axial modes (i.e., $\sin m\pi x/L$, $m = 1,3,5,\ldots$). Additionally, the symmetry implies that the reactions are identical for the frames symmetrically located about the center frame. Loading on the shell by the interior fluid is included in these calculations.

As a basis for comparison, the pressure at a radial distance of 0.05 m (2 in) in from the skin is shown on Fig. V.11 for the unframed shell excited by a circumferential in-plane load applied at the center. Figure V.11a shows the pressure 90 degrees away from the drive at axial locations from one end of 0.2, 0.4, and 0.6 m (8, 16, and 24 in). Substantial variations (e.g., 20 dB) are found within 0.2 m (8 in) axially within this frequency range. The peak pressure in this frequency range is approximately -20 dB (re: $0.09\ \mathrm{m}^{-2}$ ($1\ \mathrm{ft}^{-2}$)). The circumferential variation between points located 0.2 m (8 in) axially from the drive is shown in Fig. V.11b. Here large differences (e.g., 20 dB) are found at frequencies in the range between points located 45 degrees apart.

Results for the pressure in the framed shell excited by a circumferential load are shown on Fig. V.12. Although substantial differences at specific frequencies are found between these results and those of the unframed shell shown on the previous figure, the general frequency dependence of both results has an approximate correspondence. Furthermore the peak pressure level calculated with frames (i.e., -20 dB) is within 5 dB of that evaluated in the absence of frames. Finally, it is observed that the pressure field in the stiffened shell varies somewhat more smoothly with circumferential distance than the field in the unframed shell. The most likely explanation for the smoothness is that the response of the framed shell is dominated by the lower order circumferential modes with their corresponding longer structural wavelength.

Figure V.13 shows the pressure field in response to a moment excitation of 1.4 N-m (1 ft-lb). Although the respective levels are shifted the results are similar to those obtained with the in-plane loading shown in Fig. V.12.

As previously described the shell is excited in the analytical model by applying the reaction loads of the passive frames as well as of the driven frame. In a highly damped structure the interior pressure field would be expected to be dominated by the loads applied by the driven frame. In an undamped structure however the driven frame reactions would not be expected to dominate the response. The importance of the driven frame for the lightly damped test cylinder is indicated in Fig. V.14. Here the pressure at 0.4 m 16 in) in response to an in-plane load is shown both with and without the reactions of the driven frame included. There is no clear trend evident in these results. At some frequencies (e.g., 1000 Hz), the pressure is much different without the driven frame. The conclusion at these frequencies is that the result is dominated by the pressure induced by the drive frame loads. At other frequencies however, the two results are not much different suggesting that the contributions of the driven and passive frames are comparable.

6. Conclusions

Based on the results presented in this Chapter the following conclusions are drawn:

a. In the absence of significant scattering from wing ribs or other major structural discontinuities, the propagation loss of structureborne noise along the wing at the propeller BPF is negligible and cabin noise levels are comparable to the source pressure levels for a cylindrical fuselage.

b. Consistent modelling of the interior fluid requires either the inclusion of fluid loading in evaluating the shell response or the inclusion of boundary absorption in the interior space.

c. The interior acoustic levels on average are not appreciably altered by the presence of structural damping in the shell.

d. Compared with the pressure field in a uniform shell, the effect of frame stiffeners alter the details of the response in frequency and space. The average response and peak levels however are minimally changed.

e. The asymptotic model discussed in Section V.B.3 gives a conservative prediction (i.e., somewhat high) for the average pressure level measured in the laboratory model.

TABLE V-1

Dimensions and Properties of Aircraft and Laboratory Model

	Small Aircraft[2]	Laboratory Model
Fuselage (Shell)		
Dimensions		
Radius (a)	1.11 m (43.8 in.)	0.25 m (10 in.)
Length (L_f)	17.3 m (692 in.)	1.2 m (48 in.)
Skin Thickness (h)	1.7×10^{-3} m (.07 in.)	4.0×10^{-4} m (.016 in.)
Material		
Mass Density (ρ_f)	2.7×10^{3} kg/m^3 (2.5×10^{-4} lb-s^2/in^4)	2.7×10^{3} kg/m^3 (2.5×10^{-4} lb-s^2/in^4)
Modulus of Elasticity (E_f)	6.9×10^{10} Pa (10^7 psi)	6.9×10^{10} Pa (10^7 psi)
Poisson's Ratio (ν_f)	.33	.33
Loss Factor	0.01	0.01
Wing (Beam)		
Dimensions		
Effective Cross-Sectional Radius of Gyration (r_g)		
Skin	5×10^{-4} m (.02 in.)	2.9×10^{-2} m (1.13 in.)
Spar	5×10^{-2} m (2 in.)	
Length (L_w) (Span)	2.2 m (86.4 in.)*	1.7 m (69 in.)
Width (ΔL_f) (Chord)	4.3 m (173 in.)	7.6×10^{-3} m (3.1 in.)
Material		
Mass Density (ρ_w)	2.7×10^{3} kg/m^3 (2.5×10^{-4} lb-s/in^4)	1.7×10^{3} kg/m^3 (1.6×10^{-4} lb-s/in^4)
Modulus of Elasticity (E_w)	6.9×10^{10} Pa (10^7 psi)	4.5×10^{10} Pa (6.5×10^6 psi)
Loss Factor	0.05	0.01

---

*Assumed length from propeller hub to wing-fuselage interface.

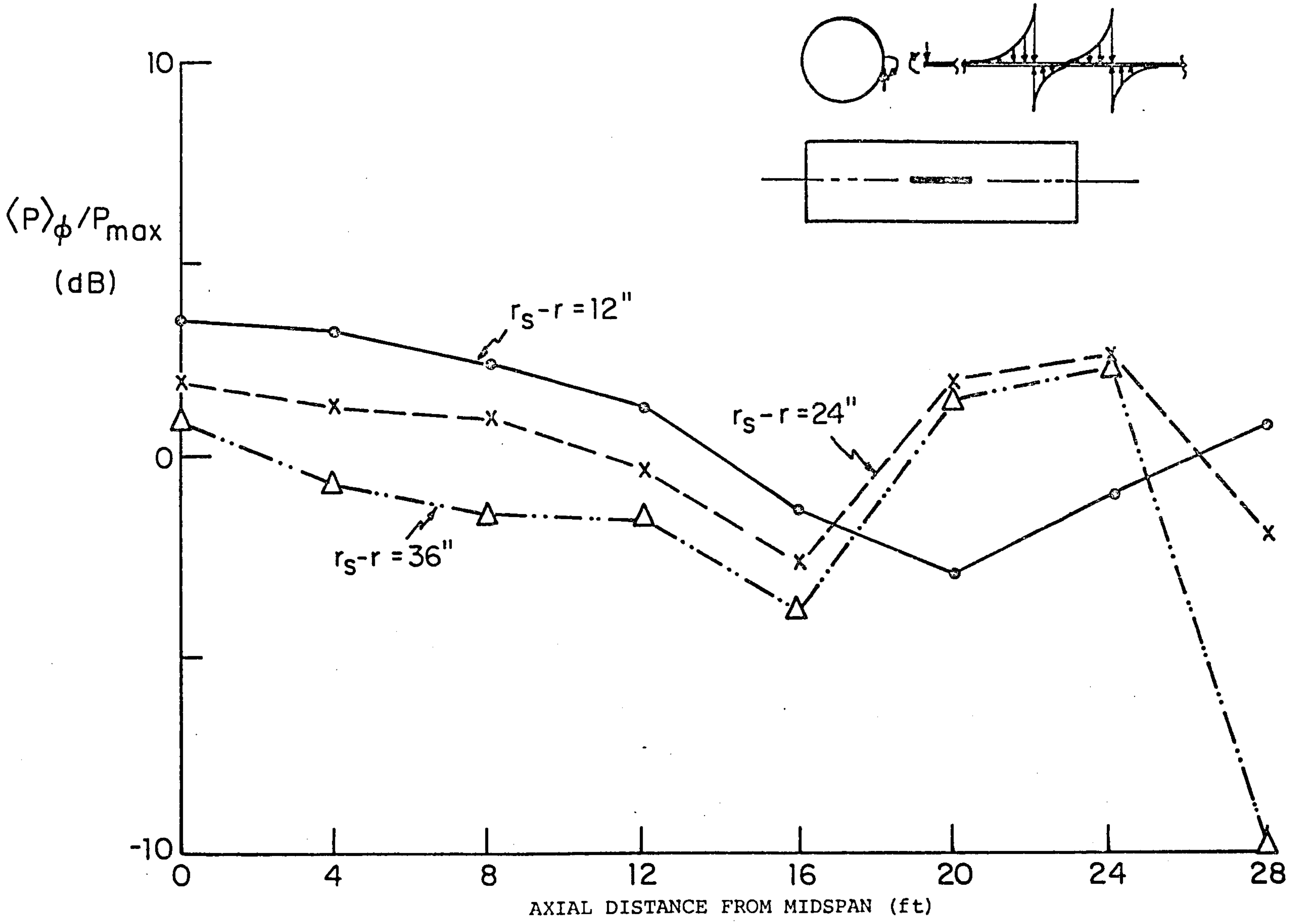

Fig. V.1 - Average fuselage interior pressure in response to wing excitation loads as a function of axial distance from midspan at 3 radial locations (1 ft = 12 in = .305 m).

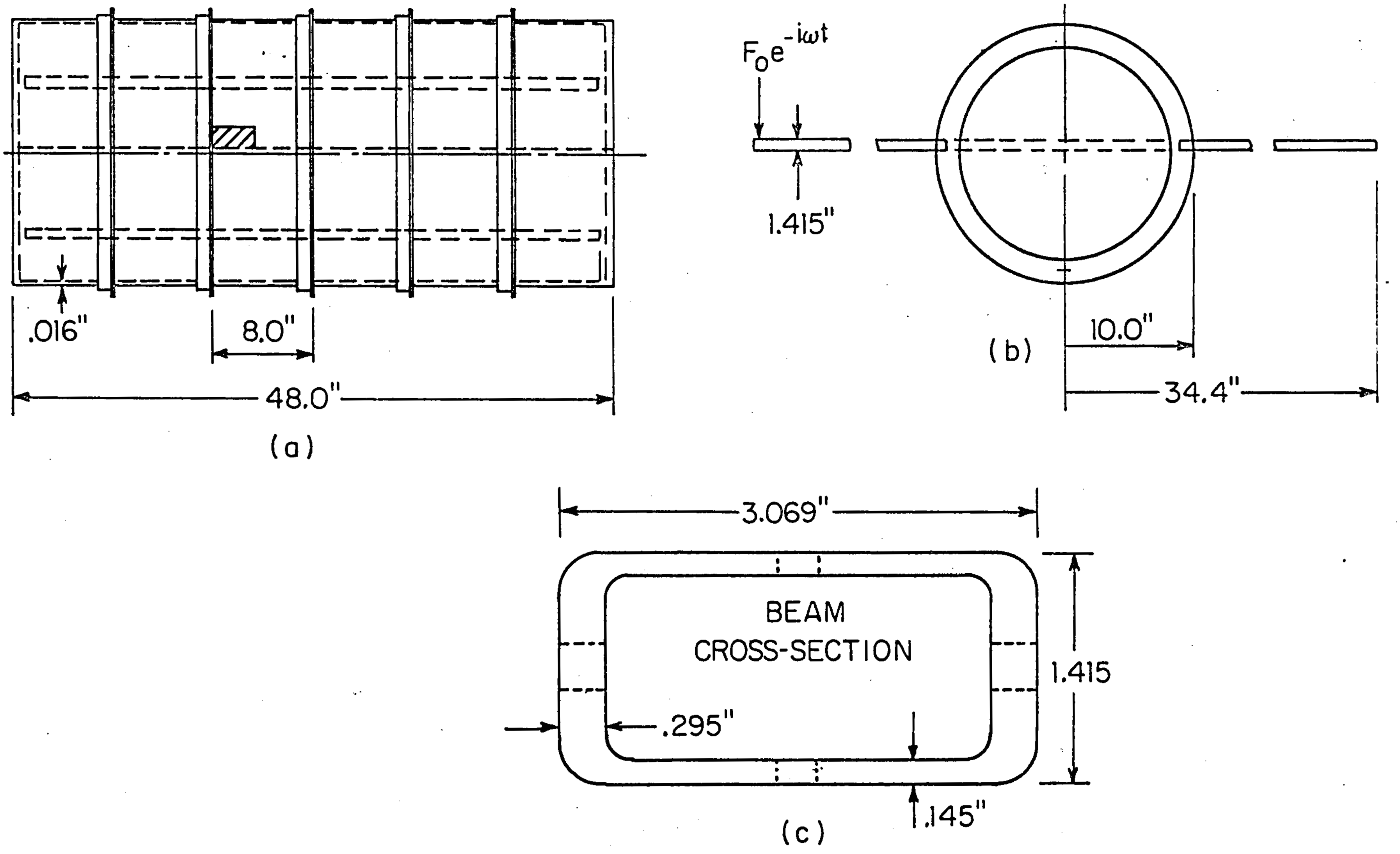

Fig. V.2 - Geometry and dimensions of laboratory model (1 in = .025 m).

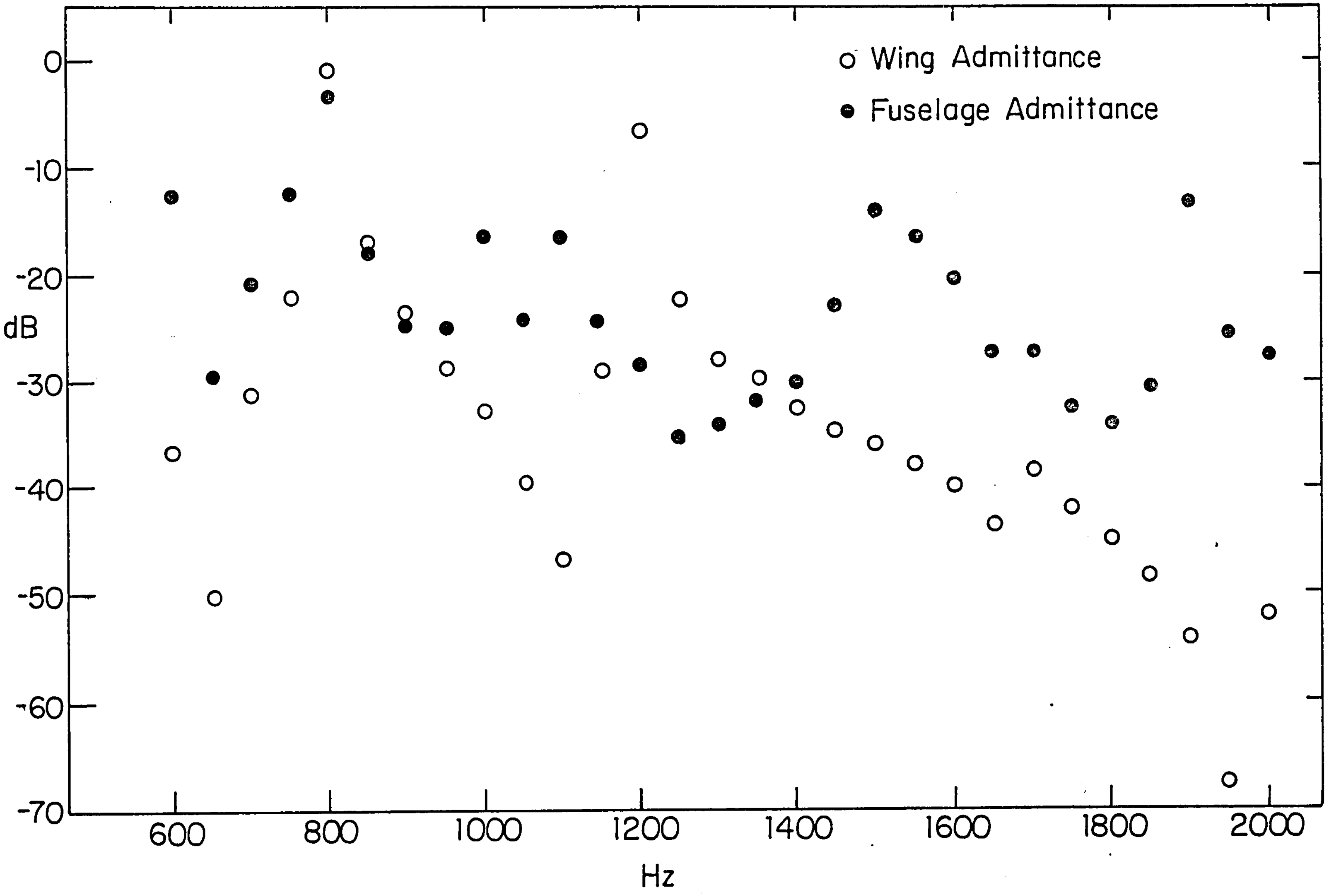

Fig. V.3 - Laboratory model point structural admittances of the beam (wing) and shell (fuselage) vs. frequency for shell location ϕ = 180°, $z = L/2$.

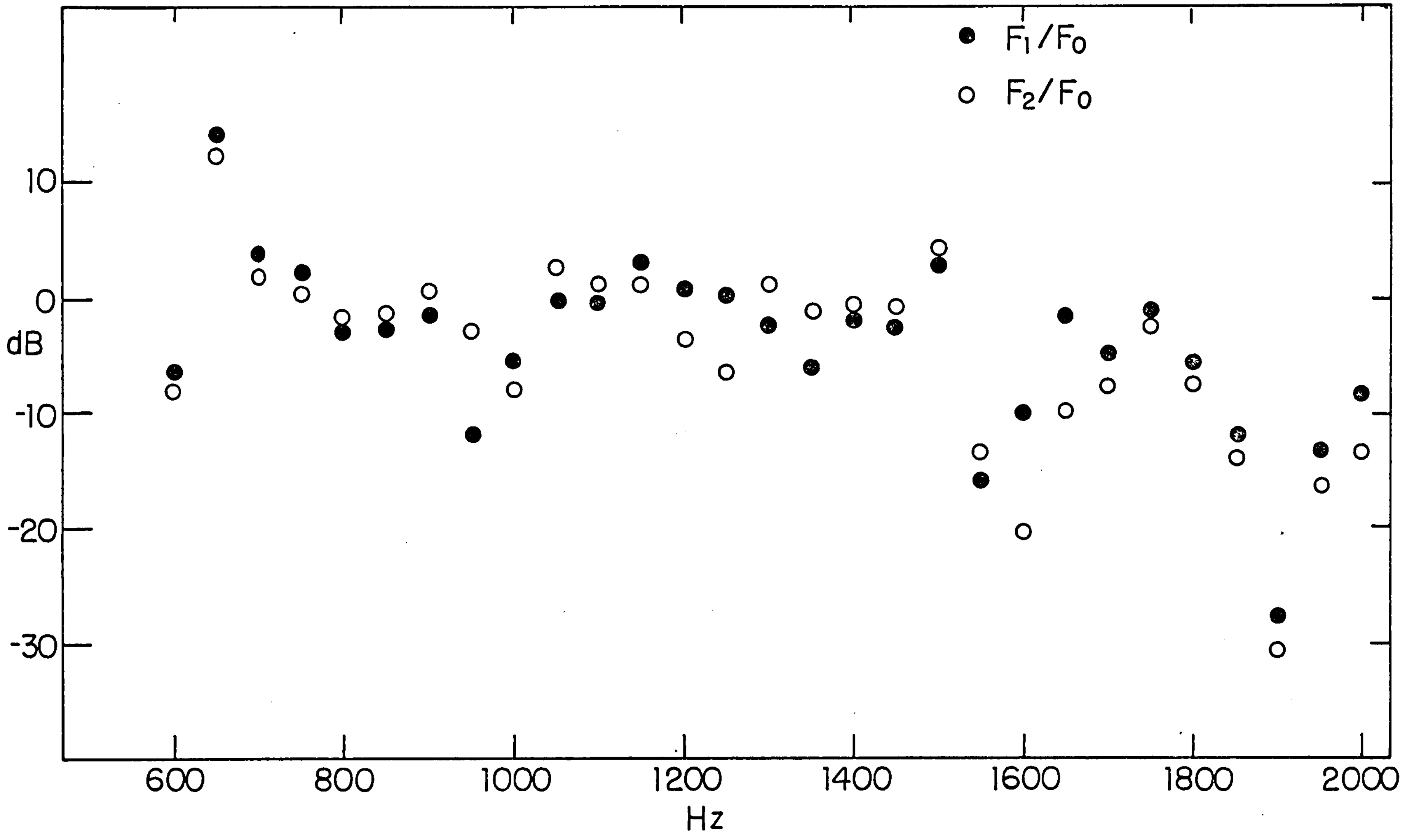

Fig. V.4 - Beam-shell reaction forces vs. frequency for the laboratory model.

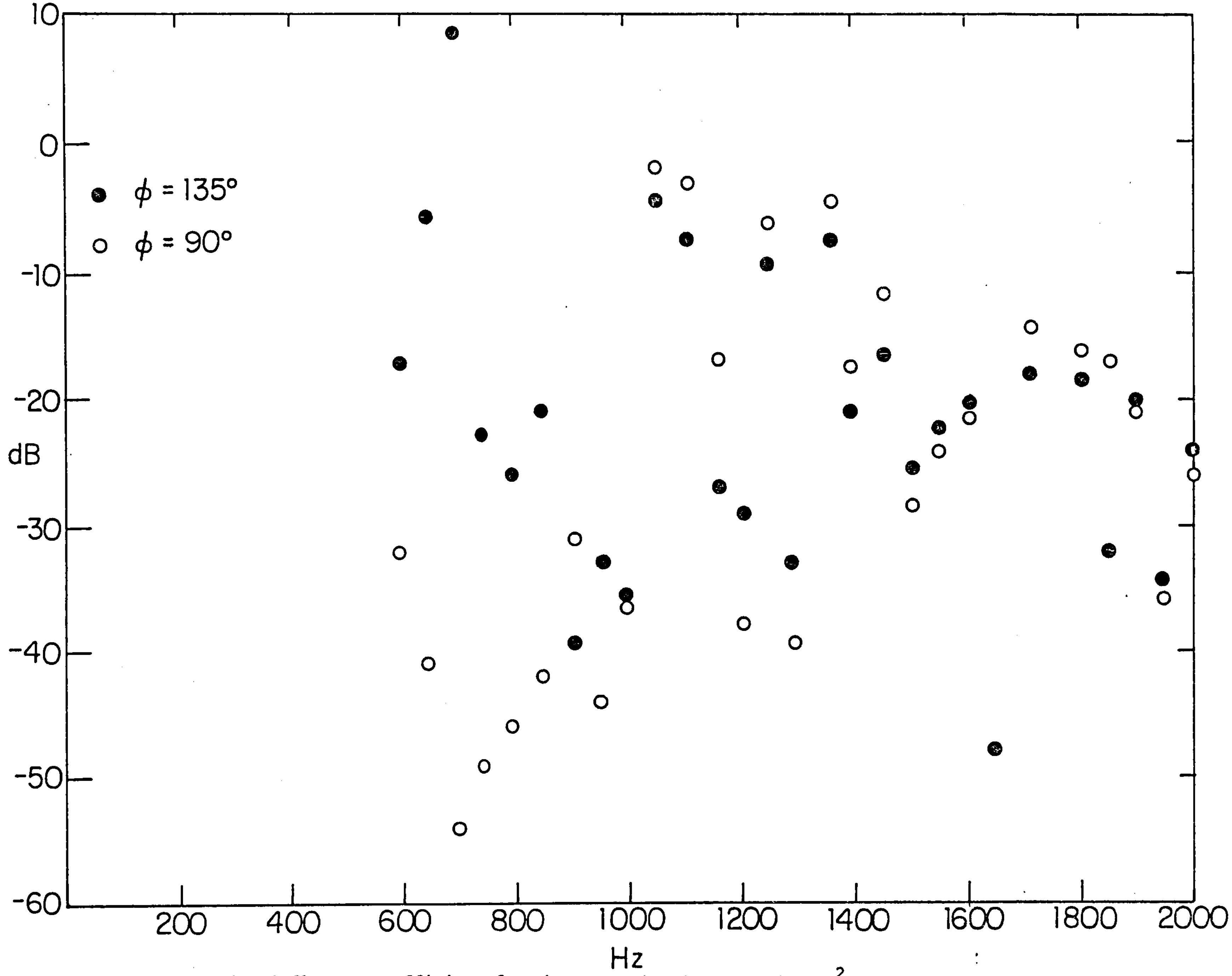

Fig. V.5 - F_1 reaction influence coefficient for the acoustic field ($p_{ac}/F_1/ft^2$) in the laboratory model vs. frequency at ϕ = 135°, 90° (with z = 42, r = .8a).

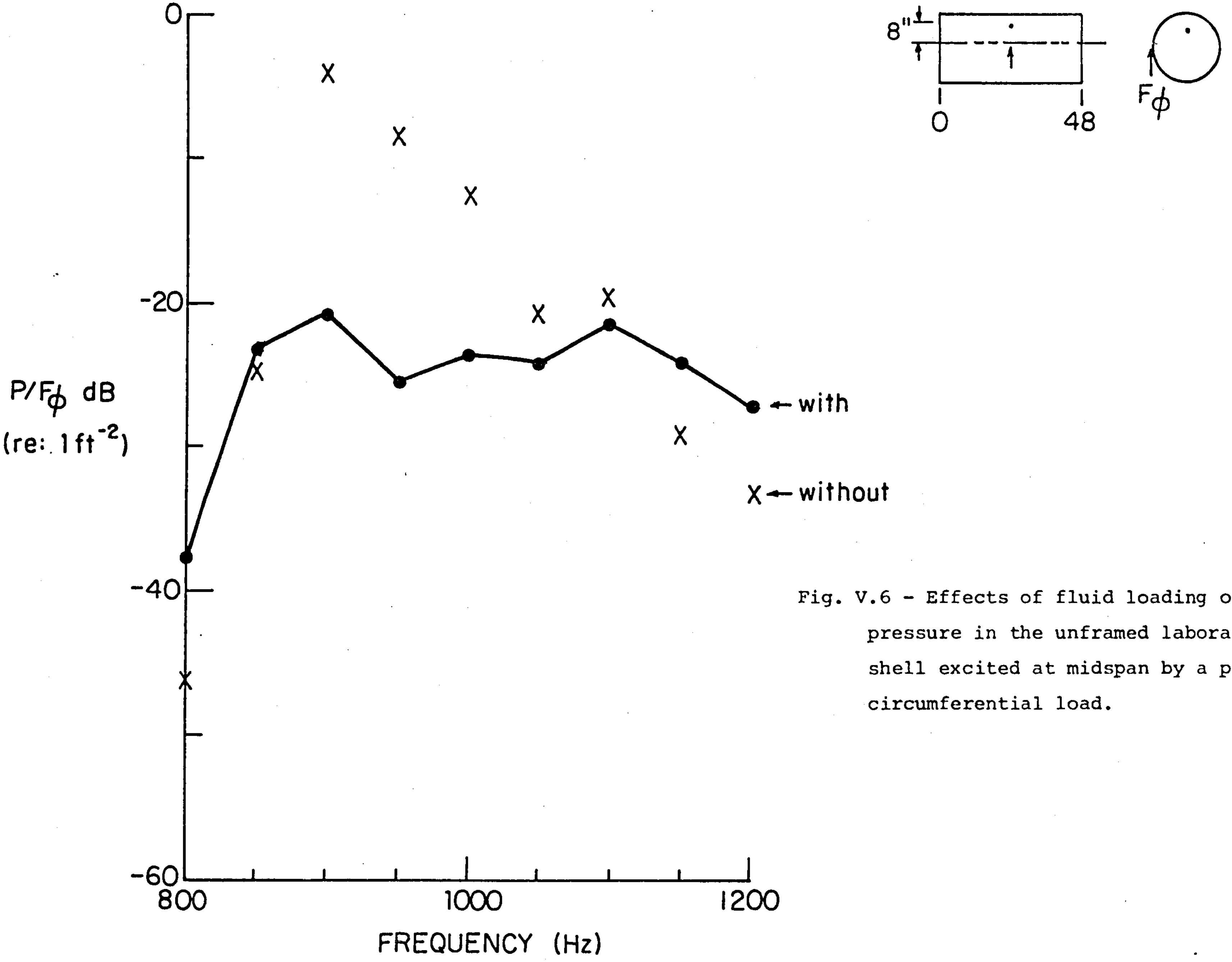

Fig. V.6 - Effects of fluid loading on the pressure in the unframed laboratory shell excited at midspan by a point circumferential load.

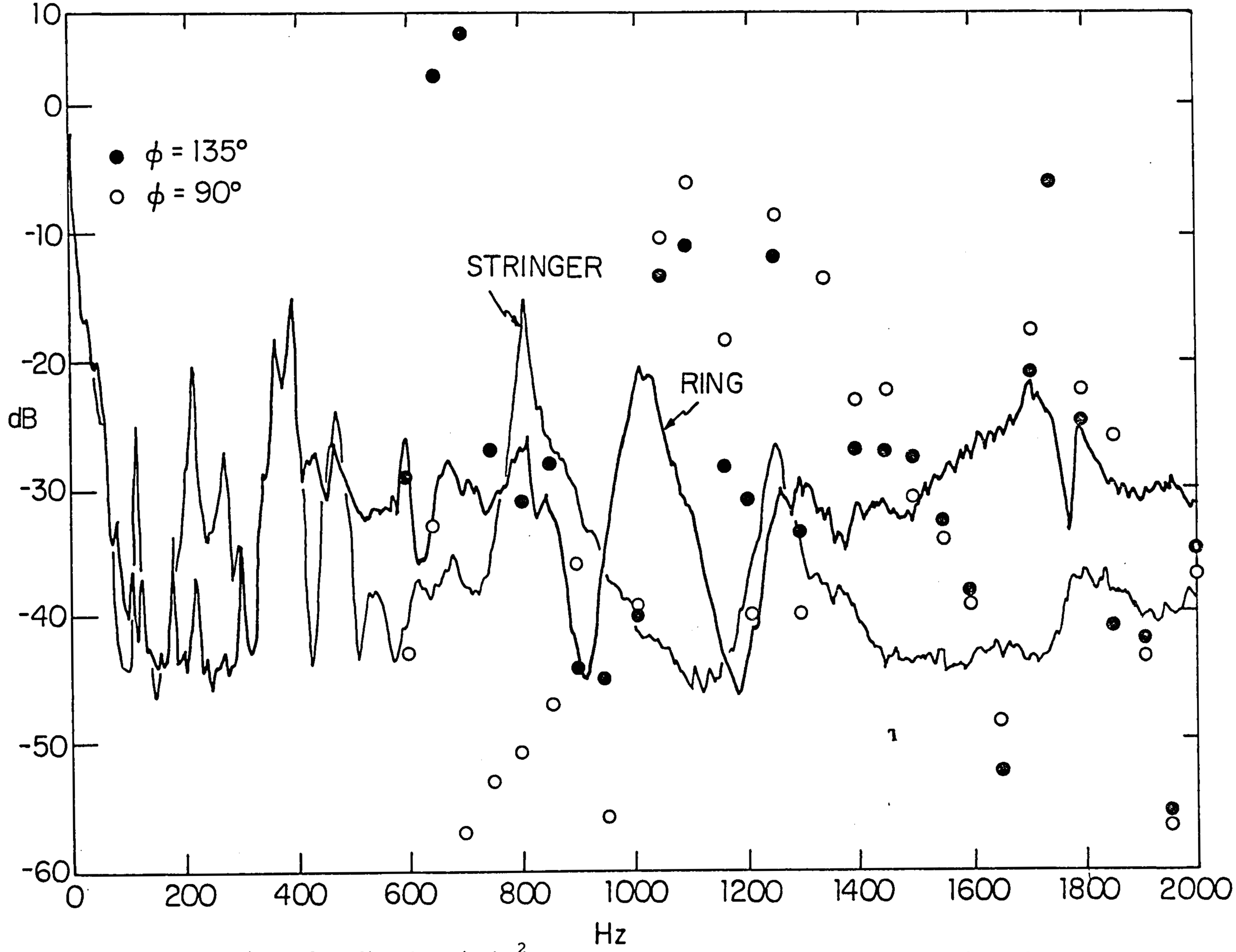

Fig. V.7 - Comparison of predicted $p_{ac}/F_o/ft^2$ spectrum for the laboratory model to experimental data for $\phi = 90°$ at $r = .8a$, $z = L/2$.

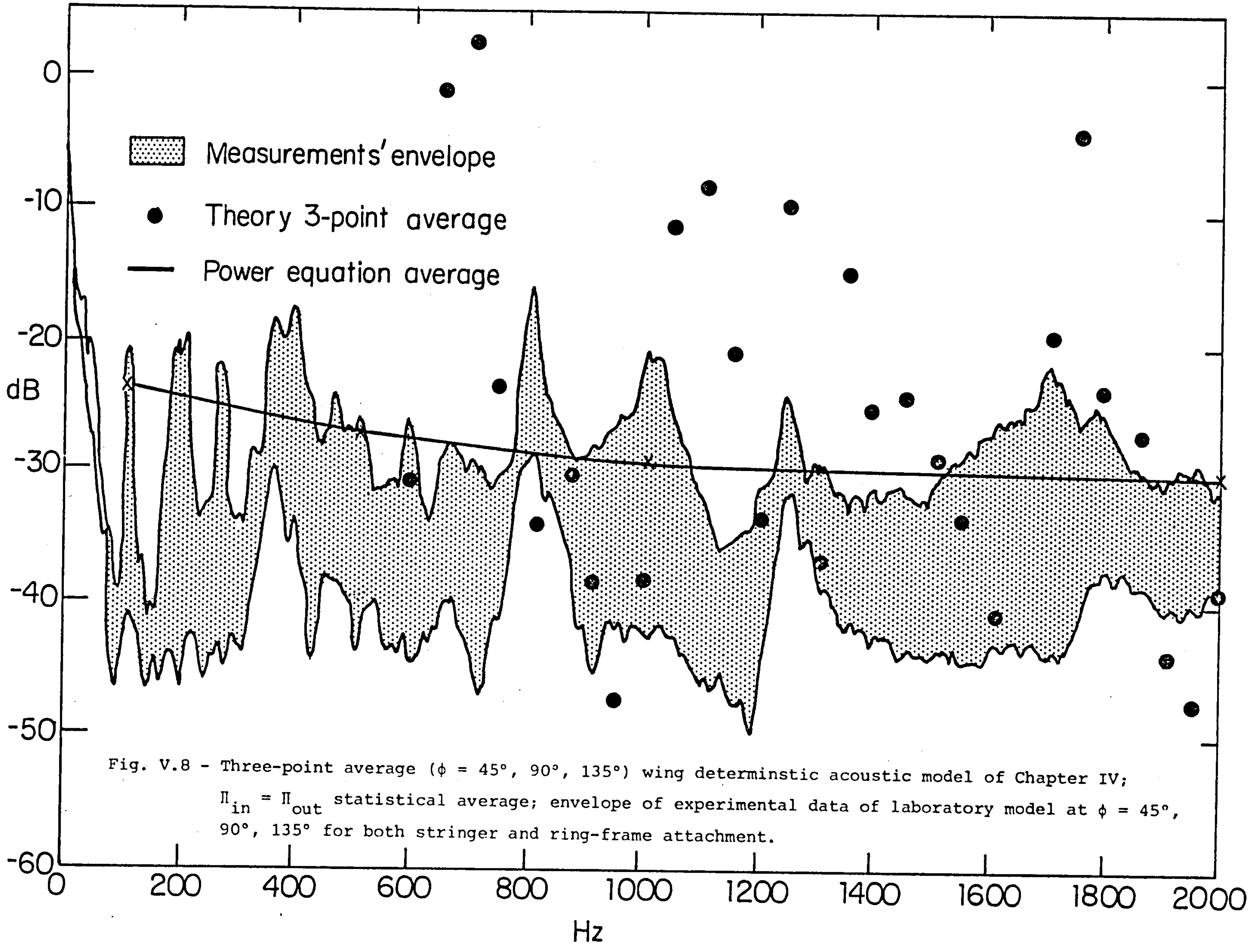

Fig. V.8 - Three-point average (ϕ = 45°, 90°, 135°) wing determinstic acoustic model of Chapter IV; $\Pi_{in} = \Pi_{out}$ statistical average; envelope of experimental data of laboratory model at ϕ = 45°, 90°, 135° for both stringer and ring-frame attachment.

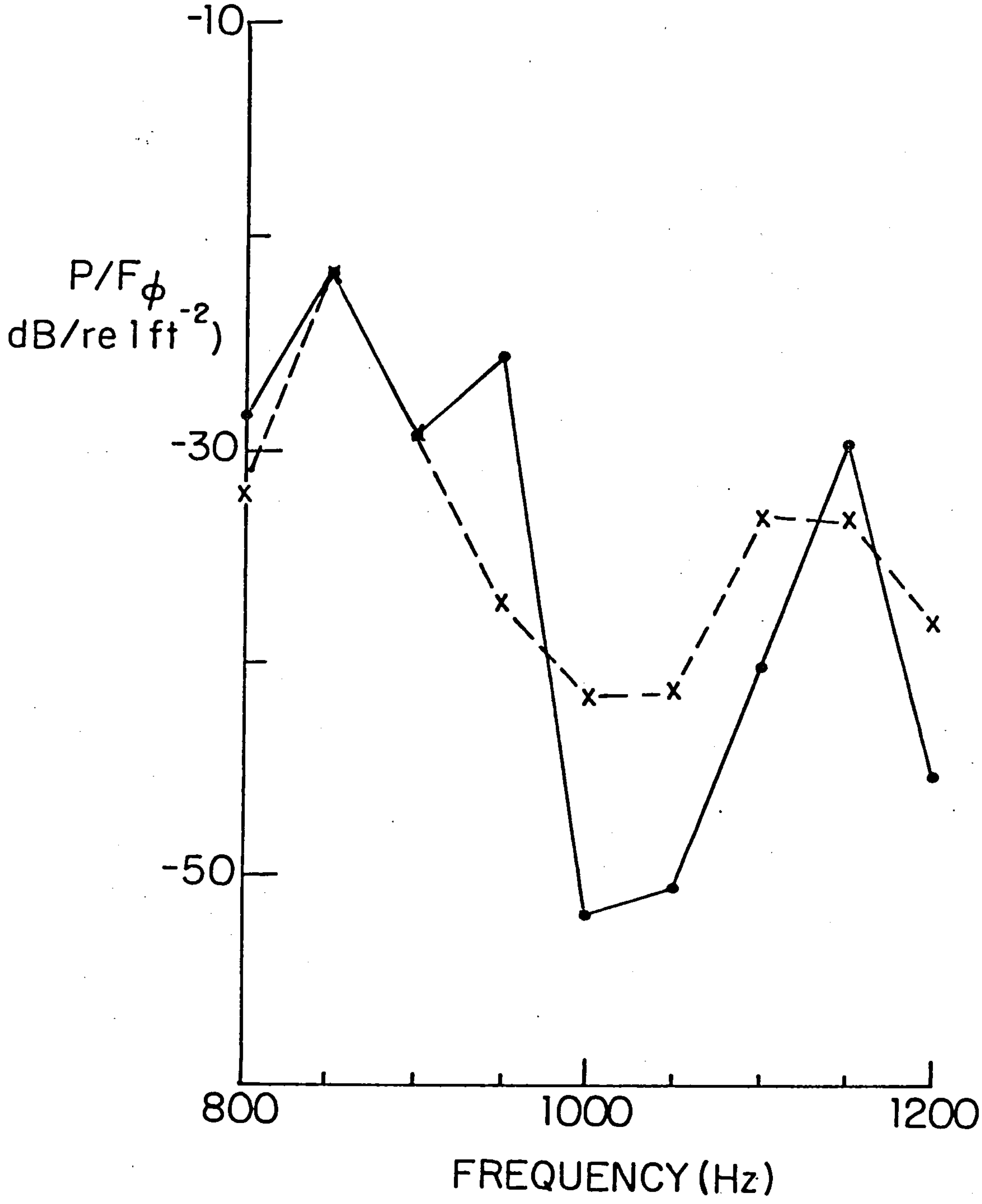

Fig. V.9 - Pressure level in response to a point circumferential load on the unframed laboratory shell for loss factors of 0.01 (•——•) and 1.0 (x---x). Pressure location is x = 16 in, r = 8 in, and ϕ = 90° (from drive) (1 in = .025 m).

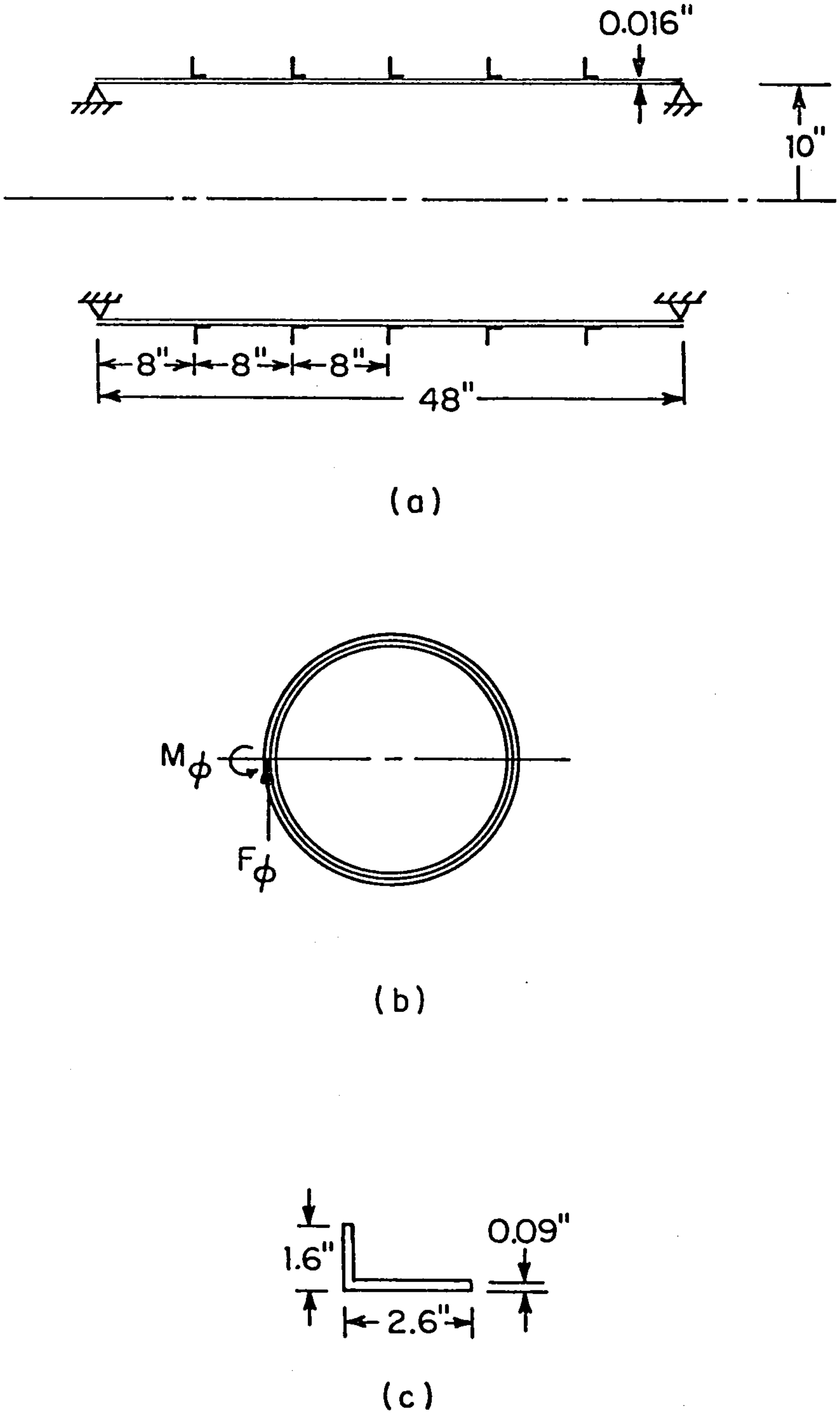

Fig. V.10 - Model of the frame stiffened laboratory cylinder showing (a) dimensions, (b) loading, and (c) frame details (1 in = .025 m).

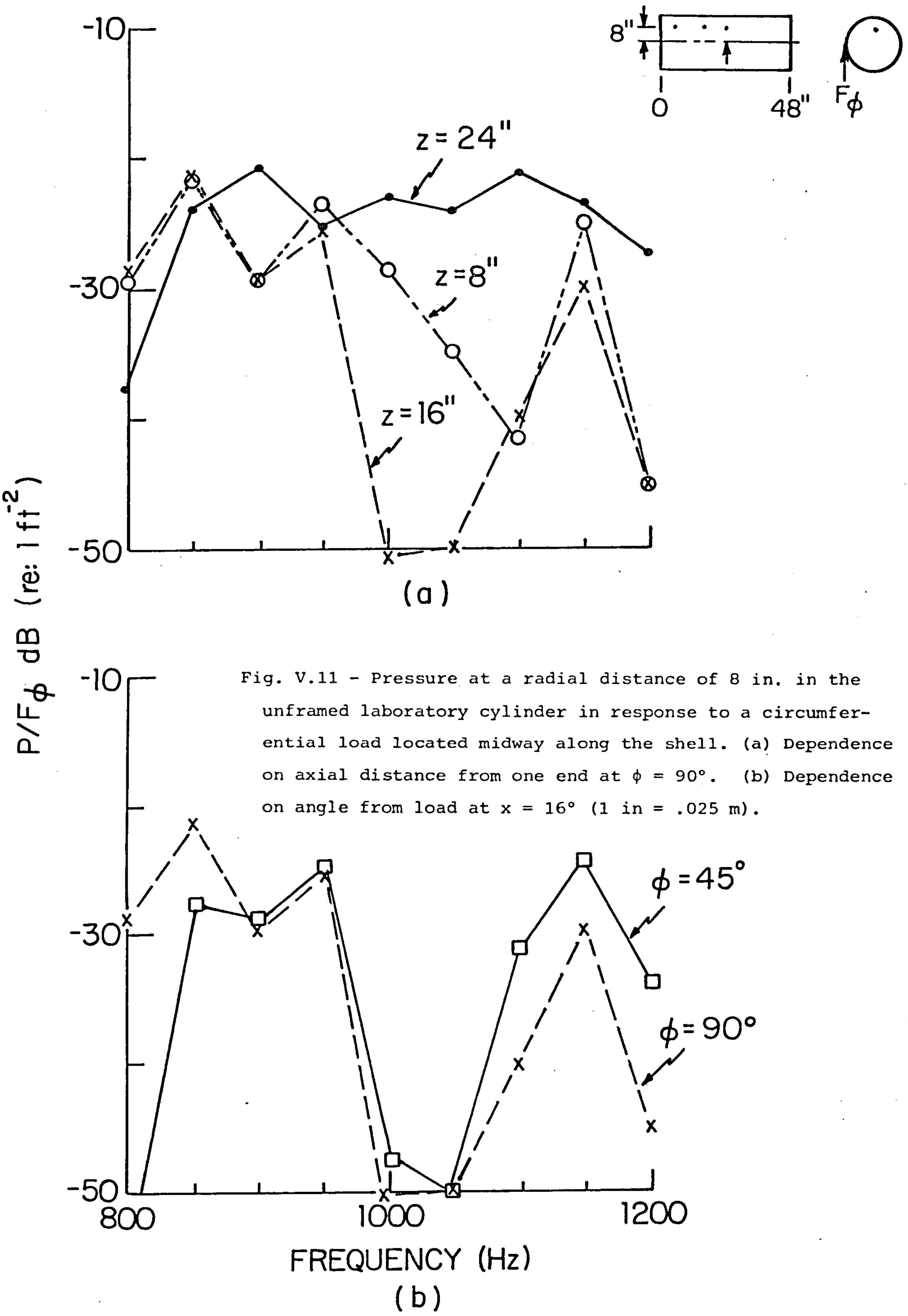

Fig. V.11 - Pressure at a radial distance of 8 in. in the unframed laboratory cylinder in response to a circumferential load located midway along the shell. (a) Dependence on axial distance from one end at ϕ = 90°. (b) Dependence on angle from load at x = 16° (1 in = .025 m).

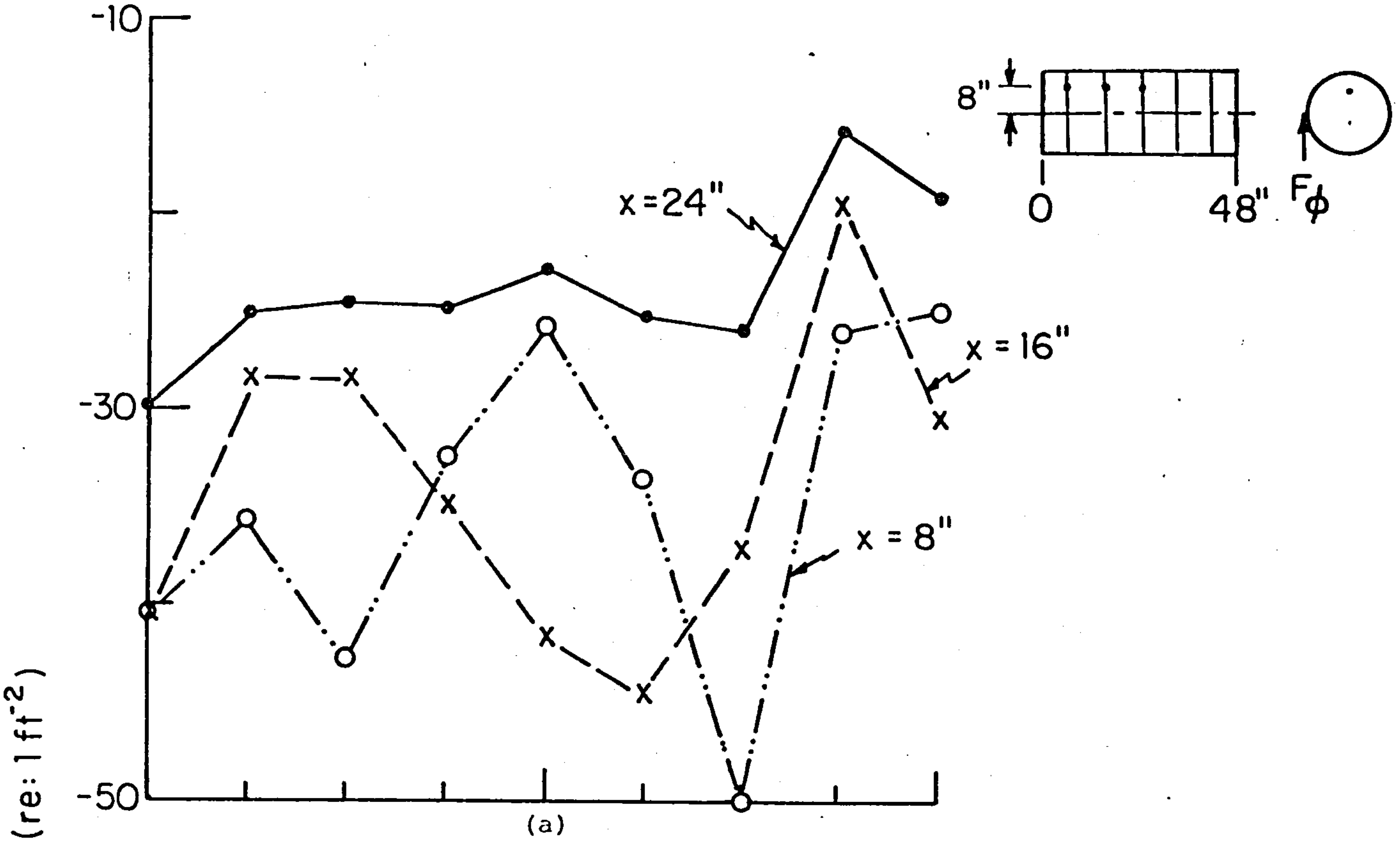

Fig. V.12 - Pressure at a radial distance of 8 in. in the framed laboratory cylinder in response to a circumferential load located midway along the shell. (a) Dependence on axial distance from one end at φ = 90°. (b) Dependence on angle from load at x = 16 in (1 in = .025 m).

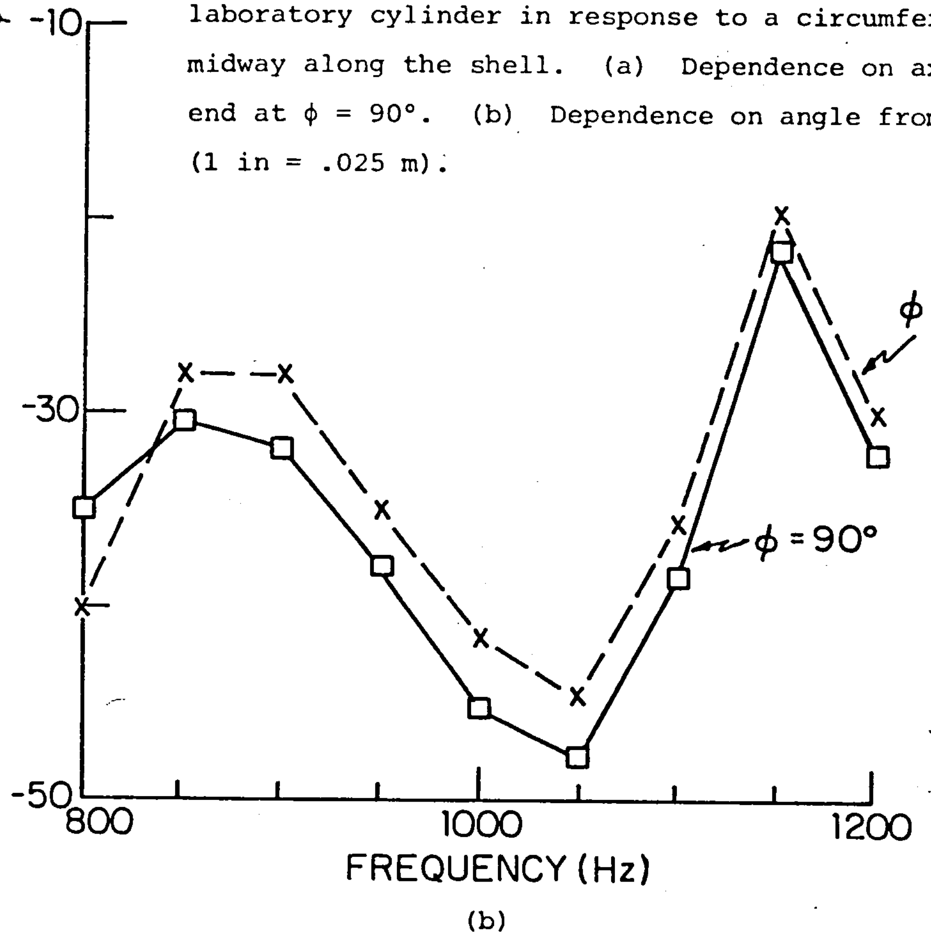

Fig. V.13 - Pressure at a radial distance of 8 in. in the framed laboratory cylinder in response to a moment excitation located midway along the shell (1 in = .025 m).

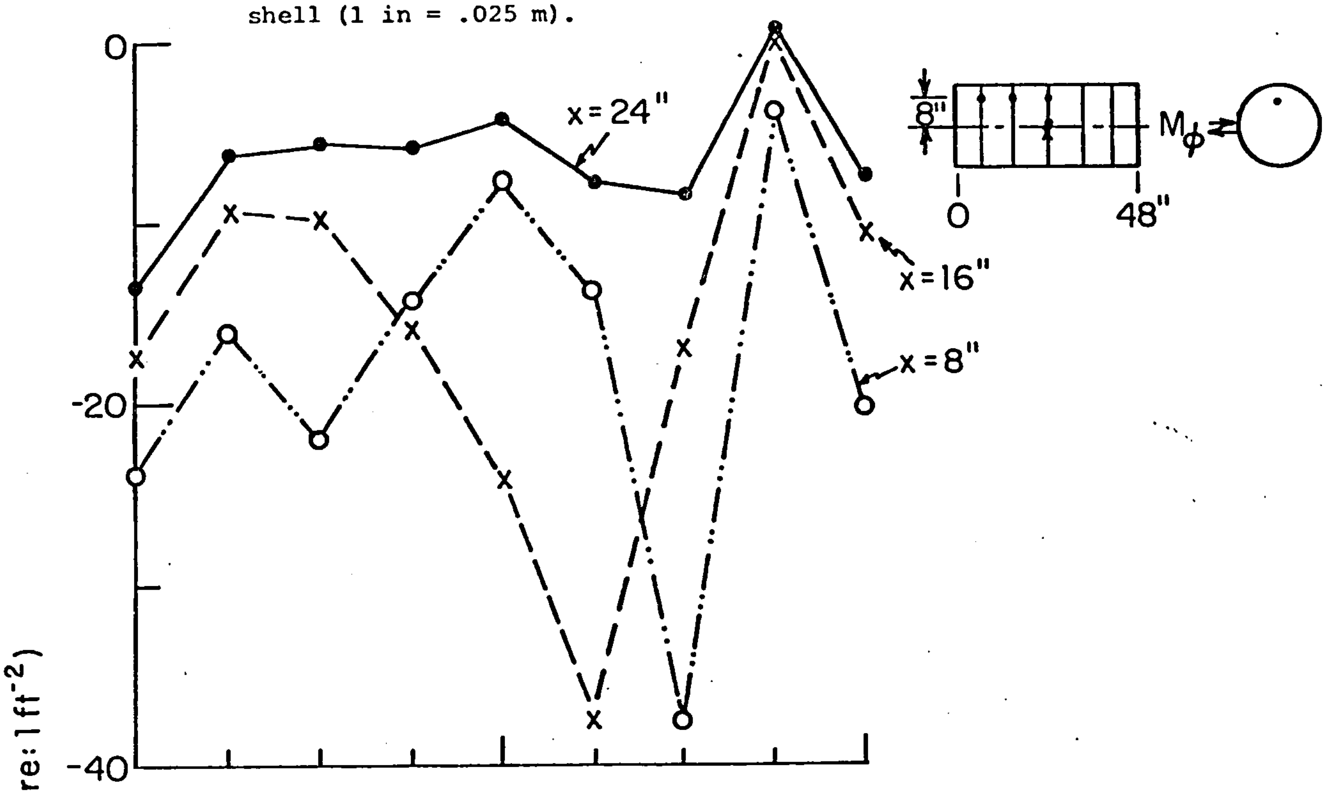

(a) Dependence on axial distance from one end at φ = 90°.

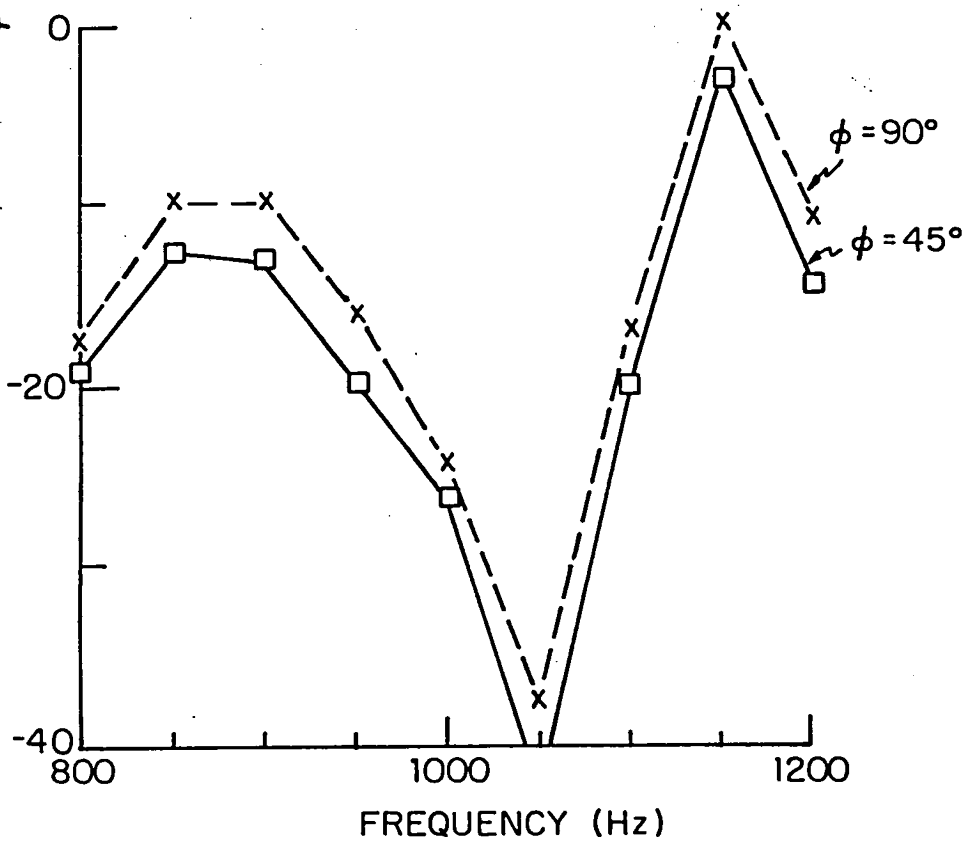

(b) Dependence on angle from excitation at x = 16 in.

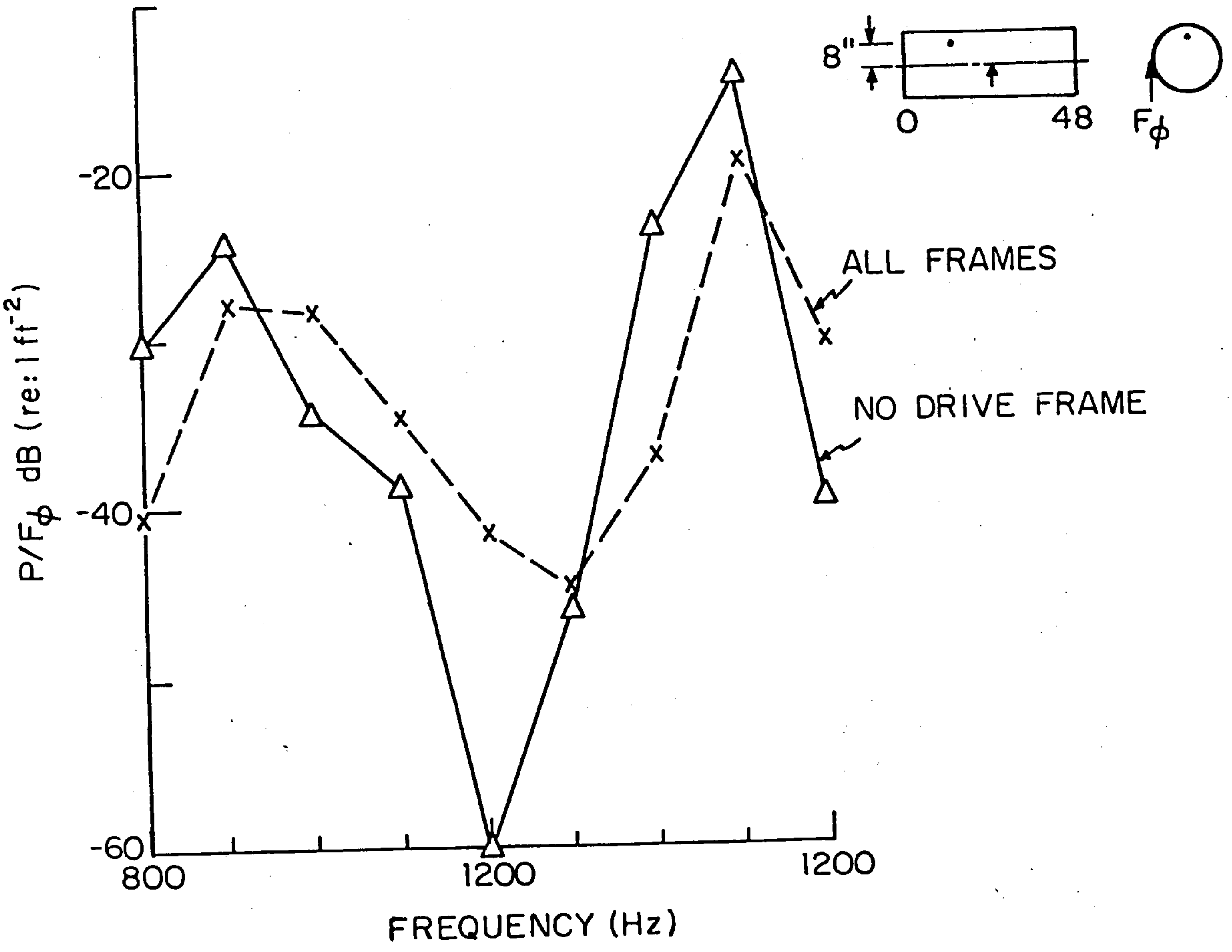

Fig. V.14 - Pressure at r = 8 in, x = -6 in, and ϕ = 90° for the framed laboratory cylinder excited by a circumferential load calculated with all frame reactions included and by omitting the reactions of the driven frame (1 in = .025 m).

REFERENCES

1 J. F. Wilby, "The Prediction of Interior Noise of Propeller-Driven Aircraft: A Review", SAE Paper 830737 (April 1983).

2 F. B. Metzger, "Strategies for Aircraft Interior Noise Reduction in Existing and Future Propeller Aircraft", SAE Paper 810560 (1981).

3 B. E. Miller, et al., The Propeller Tip Vortex - A Possible Contributor to Aircraft Cabin Noise, NASA TM 81768 (April 1981).

4 J. F. Johnston and R. E. Donham, "Attenuation of Propeller-Related Vibration and Noise", AIAA J. Aircraft, 19, 858-867 (Oct. 1982).

5 V. L. Metcalf and W. H. Mayes, "Structureborne Contribution to Interior Noise of Propeller Aircraft", SAE Paper 830735 (April 1983).

6 J. F. Unruh, et al., Engine Induced Structureborne Noise in a General Aviation Aircraft, NASA CR-159099 (Aug. 1979).

7 R. E. Hayden, et al., A Study of Interior Noise Levels, Noise Sources, and Transmission Paths in Light Aircraft, NASA CR-172152 (July 1983).

8 L. M. Milne Thompson, Theoretical Aerodynamics, (Dover, New York, 1973), p. 234-235.

9 R. K. Amiet, "High-Frequency Thin-Airfoil Theory for Subsonic Flow", AIAA J. 14, (Aug. 1976) pp. 1076-1082.

10 G. F. Carrier, M. Krook, and C. E. Pearson, Functions of a Complex Variable, (McGraw-Hill, New York, 1966), p. 47.

11 P. M. Morse and H. Feshback, Methods of Mathematical Physics, (McGraw Hill, New York, 1953), p. 217.

12 J. D. Revell and F. J. Balena, "Analytical Study of Interior Noise Control by Fuselage Design Techniques on High-Speed Propeller-Driven Aircraft", AIAA Paper 80-1001, AIAA 6th Aeroacoustics Conference, Hartford, CT (June 1980).

13 M. C. Junger and D. Feit, Sound, Structures and Their Interaction, (MIT Press, Cambridge, 1971).

14 D. J. Mead, "Free Wave Propagation in Periodically Supported, Infinite Beams", J. Sound Vib. 11(2), 1970) pp. 181-197. Also, G. SenGupta, Dynamics of Periodically Stiffened Structures Using a Wave Approach, Inst. of Sound and Vib. Res. Tech. Rept. AFML-TR-71-99 (May 1971).

15 M. C. Junger, "Impedance of Acoustic and Structural Waveguides at Their Cutoff Frequencies", J. Acoust. Soc. Am. 63(4) (April 1978), 1206-1210. Also, the application of this concept to marine vehicles was previously proposed to the Navy under contract N00014-83-C-0210.

16 R. L. Bisplinghoff, H. Ashley, and R. L. Halfman, Aeroelasticity, (Addison-Wesley, Reading, MA, 1955), p. 218.

17 E. E. Ungar, "Transmission of Plate Flexural Waves Through Reinforcing Beams; Dynamic Stress Concentrations", J. Acoust. Soc. Am. 33(5), 633-639 (1961). Also, R. H. Lyon, "Sound Radiation from a Beam Attached to a Plate", J. Acoust. Soc. Am. 34(9), 1265-1268 (1962).

18 F. R. Hanley, Strength of Materials, (McGraw Hill, New York, 1957) p. 509.

19 E. Skudrzyk, Simple and Complex Vibratory Systems, (Pennsylvania State University Press, University Park, PA, 1968), p. 207.

20 A. Harari, "Wave Propagation in Cylindrical Shell with Finite Regions of Structural Discontinuity", J. Acoust. Soc. Am. 62, 1196-1205 (1977).

21 L. R. Koval, "On Sound Transmission Into a Stiffened Cylindrical Shell with Rings and Stringers Treated as Discrete Elements", J. Sound Vib. 71, pp. 511-521 (1980); and L. R. Koval, "Sound Transmission Into a Laminated Composite Cylindrical Shell", J. Sound Vib. 71, pp. 523-530 (1980).

22 M. Abramowitz and I. A. Stegun, Handbook of Mathematical Functions, (NBS, Washington, D.C., 1964), p. 411.

23 G. N. Watson, A Treatise on the Theory of Bessel Functions, 2nd ed. (Cambridge University Press, 1952), p. 580.

24 I. N. Sneddon, Special Functions of Mathematical Physics and Chemistry, (Oliver and Boyd, New York, 1956), p. 121.

25 Ibid, p. 120.

26 Watson, op. cit., p. 134.

27 N. W. McLachlan, Bessel Functions for Engineers, 2nd ed. (Clarendon Press, Oxford, 1955), p. 200, Formula 149.

28 P. M. Morse, Vibration and Sound, 2nd ed. (McGraw Hill Book Co., New York, 1948), p. 416, Eq. 34.4.

29 A. D. Pierce, Acoustics (McGraw Hill, New York, 1981), p. 288, Eq. 6-5.16.

30 E. Szechenyi, "Modal Densities and Radiation Efficiencies of Unstiffened Cylinders Using Statistical Methods," J. Sound Vib. 19, pp. 65-81 (1971).

31 J. D. Revell and F. J. Balena, "An Analytical Model for Study of Interior Noise Control of High-Speed Propeller-Driven Aircraft," AIAA Paper 80-1000, (June 1980).

1. Report No. NASA CR-172381	2. Government Accession No.	3. Recipient's Catalog No.

4. Title and Subtitle
Analytical Model of the Structureborne Interior Noise Induced by a Propeller Wake

5. Report Date
May 1984

6. Performing Organization Code

7. Author(s)
M. C. Junger, J. M. Garrelick, R. Martinez, and J. E. Cole, III

8. Performing Organization Report No.

9. Performing Organization Name and Address
Cambridge Acoustical Associates, Inc.
54 Rindge Ave. Ext.
Cambridge, MA 02140

10. Work Unit No.

11. Contract or Grant No.
NAS1-17570

12. Sponsoring Agency Name and Address
National Aeronautics and Space Administration
Washington, DC 20546

13. Type of Report and Period Covered
Contractor Report

14. Sponsoring Agency Code
324-01-00

15. Supplementary Notes

Langley Technical Monitor: William H. Mayes
Final Report

16. Abstract

Advanced prop-fan propulsion systems which are being considered for passenger aircraft have noise characteristics quite different from turbo-jet systems they may replace. Rather than being primarily broadband much of the acoustic energy of propellers is concentrated in tonals at the harmonics of the blade-passage frequency (BPF). Since the fundamental BPF is in the range of several hundred hertz, the tonal spectrum of the propeller induced noise is of concern from the viewpoint of passenger acceptance and comfort.

The objective of this study is to examine analytically the structureborne contribution to the interior noise that is induced by the propeller wake acting on the wing. Analytical models have been developed to describe each aspect of this path including the excitation loads, the wing and fuselage structures, and the interior acoustic space. Because this is a feasibility study, the emphasis has been placed on examining a variety of parameters, and as a result different models have been developed to examine specific parameters. The excitation loading on the wing by the propeller wake is modeled by a distribution of rotating potential vortices whose strength is related to the thrust per blade. The response of the wing to this loading is examined using beam models. A model of a beam structurally connected to a cylindrical shell with an internal acoustic fluid has been developed to examine the coupling of energy from the wing to the interior space. The model of the acoustic space allows for arbitrary end conditions (e.g., rigid or vibrating end caps). Calculations are presented using these models to compare with a laboratory test configuration as well as for parameters of a prop-fan aircraft.

17. Key Words (Suggested by Author(s))
Interior Noise
Structureborne Noise
Propeller Wake
Prop-Fan Noise

18. Distribution Statement
Unclassified - Unlimited
Subject Category 71

19. Security Classif. (of this report) Unclassified	20. Security Classif. (of this page) Unclassified	21. No. of Pages 97	22. Price A05

N-305